Spin waves in periodic media and magnetic textures

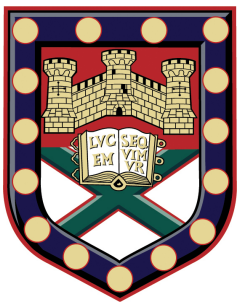

Angus Laurenson

Department of Physics

University of Exeter

This dissertation is submitted for the degree of

Doctor of Philosophy

November 2020

Dedicated to my parents and my brother

Declaration

Submitted by Angus Laurenson to the University of Exeter as a thesis for the degree of Doctor of Philosophy in Physics, September 2019. This thesis is available for Library use on the understanding that it is copyright material and that no quotation from the thesis may be published without proper acknowledgement.

I certify that all material in this thesis which is not my own work has been identified and that no material has previously been submitted and approved for the award of a degree by this or any other University.

Angus Laurenson

November 2020

Acknowledgements

First of all, I would like to acknowledge first my supervisors Dr. Volodymyr Kruglyak and Dr. Jacopo Bertolotti for their contributions to the research presented in this thesis, and my personal development these last four years. Thank you for bearing with me and pointing me back in the right direction when I got distracted and side tracked.

Thanks also to Dr. Feodor Ogrin, the unoffical third supervisor, and our motley team which undertook the X-ray scattering experiments; Dr. Nicolas Jaouen and Dr. Horia Popsecu from SOLEIL synchrotron, Max Birch and Luke Turnbull of Durham University, Erick Burgos and Nick Bukin of Exeter University and our wider collaborators, James Louden of Cambridge university and many more too numerous to list, who prepared samples and performed complimentary experiments.

Thanks go to my friends and colleagues who put up with me and kept me sane. Special shout out to Natalie Whitehead for good sense and bad taste, Tom McDermott for good taste and bad sense, Callum Vincent for being the god of the computer and Charlie Mann for being himself.

Finally I am grateful to the centre for doctoral training in metamaterials χM^2 for providing funding, training and a framework of support.

Table of contents

Chapter 1

Introduction

Magnets have long been established as a key component data storage technologies, [1–4]. Information is stored in the internal magnetisation configuration of the magnet. Today, collective waves of magnetisation precession, known as spin waves, are considered a promising information carrier in future spin wave devices [5, 6]. They offer several advantage over electron for this purpose, lower energy consumption and heat generation whilst their coherence lengths are greater, enabling wave computing phenomena [7]. This comes at the expense of shorter lifetimes and a more complicated relationship between the propagation characteristics and the geometry of the device [8, 9]. To control their propagation, periodic media known as magnonic crystal have been developed which break the spin wave spectrum into a series of minibands [10]. Recent interest into a new class of mobile bubble domains known as magnetic skyrmions has reopened questions regarding the size, stability, mobility and dynamic modes of bubble domains [11, 12]. Although the theory of domains and spin waves are well established [13], there remains a long way to go before the two can be combined into a feasible technology [14]. As new magnetic materials are synthesised and fabrication techniques improve, new phenomena are still being discovered [15]. The research in this thesis was aimed at both spin wave propagation in periodic media and the formation

of new magnetic textures which could in the future find application in new magnonic crystals or other devices.

Chapter 2 introduces the central topics addressed in this thesis. First, the history of magnetism research is condensed into a few short paragraphs. Followed by a more detailed discussion of micromagnetic physics and the origins of ferromagnetism, which forms the theoretical basis upon which the rest of the work is built. Ferromagnetic resonance of magnetic media is then introduced which naturally leads to the topic of spin waves, which are discussed in the context of ferromagnetic films. Magnonic crystals, periodic magnetic media which open band gaps in the spin wave spectrum, and Magnetic bubble domains, cylindrical magnetic domains, are both introduced here, as they both appear in multiple chapters. The chapter closes with a short description of micromagnetic simulations which are a key tool in micromagnetism research.

Chapter 3 is concerned with the Bloch oscillation of spin waves in a periodic magnetic medium. An approximate theory is first derived that describes the Bloch oscillations and then it is applied to backward volume spin waves in a periodically modulated Yttrium Iron Garnet film. Periodic field modulation and periodic modulation of the magnetisation saturation are both used to open band gaps in the spin wave spectrum. When gradient in the bias magnetic field is introduced, spin waves are induced to perform Bloch oscillations. Micromagnetic simulations are used to validate the theory and both Bloch oscillations and Bloch-Zener oscillations are observed and characterised. Finally an experimental method is proposed to observe Bloch Oscillations of spin waves for the first time.

Chapter 4 follows the story of X-ray scattering experiments aimed at imaging a recently discovered and exotic domain structure known as a biskyrmion. Publications reporting Lorentz transmission electron microscopy image of biskyrmion domains in MnNiGa films have the disadvantage of only being sensitive to in-plane magnetic flux density. Using off axis X-ray holography we show that the reported biskyrmion domains are more likely to be

traditional, type 2 bubble domains. This analysis was reinforced by our collaborators who performed micromagnetic simulations showing that type 2 bubble domains and biskyrmions give rise to nearly identical images when measured using Lorentz transmission electron microscopy images.

Chapter 5 reports a micromagnetic simulation of a complex magnonic crystal composed of a honeycomb array of magnetic bubble domains, confined within a hexagonal lattice of antidots. The low frequency modes corresponding to the oscillation of the bubble domain walls are shown to interact with one another to form a band structure. The breathing mode dominates the response of the system to exeternal magnetic field pulses and forms the widest band with the greatest group velocities. Higher order oscillations of the bubble domain wall form much flatter, weakly propagating bands. The domains interact through their magnetic fields and a simple model of interaction is developed with qualitatively explains the trend towards zero group velocity for higher order modes.

Chapter 6 rounds off this thesis with concluding remarks regarding the research presented within it.

Chapter 2

Micromagnetism

" .. all the twistings and turnings that must go on in all those atomic magnets. (Some people like to amuse themselves with the theory of these things!) "

-Feynman

Magnetism takes its name from the ancient Greek territory of Magnesia, where magnetic magnetite ore was discovered that attracted iron. They used it as a novelty and for superstitious medicine. Today our modern, scientific understanding enables us to use magnetism for real medicine, [16]. In fact magnetism underpins many technologies we rely on, from electrical power generation [17, 18] to microwave signal processing in our telecommunications [19] and magnetic data storage in our computers [1–3], to name just a few.

The first breakthroughs in understanding magnets came with Orsted's experiment that showed a current-carrying wire exerts a force on magnets and other current-carrying wires [20]. This inspired Ampere to study the problem and he suggested that magnets possessed microscopic currents circulating constantly inside them which generated the magnetic field. Mathematical treatment of the relationship between electricity and magnetism was established by Maxwell, unified electricity, magnetism and light, setting the foundation of electromagnetism [21]. None the less, Weiss was to show that classical electromagnetism cannot explain

the strength of permanent magnets [22, 23]. It took the development of Quantum mechanics in the early 20th to explain the origin of permanent magnets as arising from the exchange interaction, an effect with no classical analogue [24, 25]. Understanding of the internal magnetic structure of magnets and their dynamics remained a challenging problem.

Micromagnetism is the study of magnetisation on length scales great enough that a continuous medium approximation can be applied, but small enough that magnetic textures such as domain walls can be resolved. Approximately nanometre to micrometre length scales. Built on the theory of Landau and Lifshitz [26] and refined by Brown [27], it boasts success in predicting the domain patterns formed in ferromagnets [26], magnetisation dynamics such as spin-waves [28, 5], domain wall motion [29] and more. With the advent of micromagnetic simulations, researchers can go beyond the limitations of analytical theory and explore the full range of non-linear phenomena that occur within magnetic materials [30–32]. Today research is aimed at increasingly exotic phenomena to develop materials and devices which have applications in information technologies [12, 33].

The micromagnetic model has three pieces. The first being the free energy of a ferromagnet which is composed of all the energies which affect the magnetisation. The second piece is the effective field, so-called because it takes the form of a magnetic field but not all of its contributions are true magnetic fields. It is the functional derivative of the free energy with respect to the magnetisation and it feeds into the final piece which is the equation of motion of magnetisation. This determines the time evolution of magnetisation and was originally developed by Landau and Lifshitz [13, 26, 34]. The equilibrium magnetisation configuration is determined by minimising the free energy, while the magnetisation dynamics are determined by the free energy combined with the equation of motion.

2.1 Free energy of a ferromagnet

The free energy of a ferromagnet can in principle contain many terms, many of which describe either rare or extremely weak phenomena. There are however some terms which cannot be left out and these essential contributions to the free energy are discussed here.

2.1.1 External field

The simplest contribution to the free energy is the influence of external fields. Since the magnetisation is the density of dipole moments, the energy density is just the energy of a dipole in an external field,

$$\varepsilon_{\text{ext}} = -\mathbf{M} \cdot \mathbf{H}_{\text{ext}}, \tag{2.1}$$

where $\mathbf{H}_{\text{ext}}$ is the external magnetic field and ε_{ext} is the Zeeman energy density, named in honour of Pieter Zeeman who made his name showing the splitting of spectral lines due to external magnetic fields [35]. In addition to controlling the static magnetic state, time-dependent external fields can be used to induce dynamics. For example, short pulses to excite broadband behaviour, or continuous wave excitation to excite specific frequencies [36, 5].

2.1.2 Demagnetising field

The most complicated term in the free energy is the interaction of the magnetisation with itself via its magnetic field. It is known as the demagnetising field because it acts to minimise the total magnetic moment. In principle, every magnetic moment in the system affects every other moment. Therefore the field is found by integrating over the entire volume as,

$$\mathbf{H}_{\text{d}} = -\frac{1}{4\pi} \int_V \nabla \cdot \mathbf{M} \frac{\mathbf{r}}{|r|^3} \, dV, \tag{2.2}$$

where $\mathbf{H}_\mathrm{d}$ is the demagnetising field and $\mathbf{r}$ is the vector between the element of volume dV and the point where the field is evaluated.

This solution for the magnetic field is a solution of Maxwell's equations in the static limit. Relieved of their time dependence, electrostatics and magnetostatics take the same forms. Here Divergent and convergent magnetisation take the role of positive and negative magnetostatic charges. As do magnetisation components normal to a surface. The associated energy density take the form,

$$\varepsilon_\mathrm{d} = -\frac{1}{2}\mathbf{M}\cdot\mathbf{H}_\mathrm{d}, \tag{2.3}$$

where the shape of a system can induce strong anisotropy through the formation of magnetostatic charges at the surfaces. The most important examples are thin films where the demagnetising field makes perpendicular magnetisation energetically unfavourable, creating a hard axis [37, 38]. Weiss showed that the dipolar interaction is not responsible for the spontaneous magnetic ordering observed in ferromagnets and that a molecular field thousands of times stronger must be responsible. [22, 23].

2.1.3 Exchange interaction

The true nature of Weiss' molecular field was explained by Heisenberg, who suggested that the exchange interaction is responsible [24]. In ferromagnets, the exchange interaction promotes the parallel alignment of neighbouring atomic moments. Fundamentally it arises from the difference in electrostatic energy states that arise from the condition that electron wave-functions must change sign when exchanged.

Direct exchange is the simplest manifestation that is concerned with localised valence electrons of neighbouring atoms. Consider the textbook case of molecular hydrogen, composed of two electrons and two protons. It has a hamiltonian,

$$\mathscr{H} = \mathscr{H}_0 + \mathscr{H}_1, \tag{2.4}$$

where, $\mathscr{H}_0$ is the Hamiltonian the isolated hydrogen atoms,

$$\mathscr{H}_0 = -\frac{\hbar^2}{2m}(\Delta_1 + \Delta_2) - \frac{e^2}{r_1} - \frac{e^2}{r_2} \tag{2.5}$$

and $\mathscr{H}_1$ represents their coloumb interaction,

$$\mathscr{H}^1 = \left(\frac{e^2}{R_{ab}} + \frac{e^2}{r_{12}} - \frac{e^2}{r_{a1}} - \frac{e^2}{r_{b2}}\right), \tag{2.6}$$

where R_{ab} is the separation between protons, r_{12} between electrons and r_{a1}, r_{b2} are the separation vectors between the electrons.

The spatial component of the two electron wavefunction can be composed of symmetric or antisymmetric linear combinations of single electron wave functions,

$$\psi^{(\pm)}(r_1, r_2) = \frac{1}{\sqrt{2}}\left[\Phi_a(r_1)\Phi_b(r_2) \pm \Phi_a(r_2)\Phi_b(r_1)\right], \tag{2.7}$$

where $\Phi_a(r_1)$ the wave function of the electron 1 in state a, with $\Phi_a(r_2)$ the same for electron 2 and $(\pm)$ indicates the symmetry of the combination (+) for symmetric and (-) for antisymmetric.

Two eigenvalues of the Hamiltonian are found, for the spatially symmetric and antisymmetric wave functions respectively.

$$E^{(\pm)} = E_0 \pm \frac{C + J_{ex}}{1 + S^2}, \tag{2.8}$$

where C is the expectation value of the coulomb intergral, J_{ex} is the exchange integral and S is the overlap integral. Considering the interaction as a perturbation on the internal energy of the separate hydrogen atoms, the overlap integral $S \to 0$,

$$E_2^{(\pm)} = C \pm J_{ex} \tag{2.9}$$

where,

$$\begin{aligned} C &= \iint \Phi_a(r_1)^2 \mathscr{H}_1 \Phi_b(r_2)^2 d^3 r_1 d^3 r_2, \\ J_{ex} &= \iint \Phi_a^*(r_1) \Phi_b^*(r_2) \mathscr{H}_1 \Phi_b(r_1) \Phi_a(r_2) d^3 r_1 d^3 r_2, \end{aligned} \tag{2.10}$$

The exchange integral J_{ex} is negative for Hydrogen, therefore the symmetrical spatial wavefunction has the lower energy. Thus far, the spin part of the electron wavefunction has not been considered. They are indirectly related to the energy by the rule that the two-electron wavefunction must be antisymmetric. This connects the spin state to the Coulomb energy.

It follows that the spinor component of the two-electron wavefunction must, therefore, be anti-symmetric. Like the spatial component, the two-electron spinor is also a linear combination of the individual spin components, which can be either up or down.

$$\chi_s^{(\pm)} = \frac{1}{\sqrt{2}} \left[\chi_s^{(1)} \chi_s^{(2)} \pm \chi_s^{(2)} \chi_s^{(1)} \right] \tag{2.11}$$

where $\chi_s^{(i)}$ is the spinor of electron i with spin state s. There is one antisymmetric combination that has one spin up and one spin down, for a total S=0.

$$\chi_{m=0}^{(-)} = \frac{1}{\sqrt{2}} \left[\chi_\uparrow^{(1)} \chi_\downarrow^{(2)} - \chi_\uparrow^{(2)} \chi_\downarrow^{(1)} \right] \tag{2.12}$$

There are three states with $S = 1$ known as the triplet states with $m = -1, 0, 1$ respectively.

$$\begin{aligned} \chi_{m=1}^{(+)} &= \frac{1}{\sqrt{2}} \left[\chi_\uparrow^{(1)} \chi_\uparrow^{(2)} \right] \\ \chi_{m=0}^{(+)} &= \frac{1}{\sqrt{2}} \left[\chi_\uparrow^{(1)} \chi_\downarrow^{(2)} + \chi_\uparrow^{(2)} \chi_\downarrow^{(1)} \right] \\ \chi_{m=-1}^{(+)} &= \frac{1}{\sqrt{2}} \left[\chi_\downarrow^{(1)} \chi_\downarrow^{(2)} \right] \end{aligned} \tag{2.13}$$

The total wavefunction is given by the product of spatial and spinor. It must be antisymmetric (-) for electrons.

$$\Psi^{(-)} = \psi^{(\pm)}\chi^{(\mp)} \tag{2.14}$$

In the hydrogenic case, the lower energy state is obtained for antisymmetric spin states. However, in Ferromagnetic materials, the lower energy state is obtained for symmetric spin states and this is the cause of ferromagnetism. Direct exchange is dominant for local moments in non-metals in non-metallic ferromagnets.

Dirac pointed out that the critical feature of the Heisenberg Hamiltonian could be simply expressed as the dot product of the neighbouring spins,

$$\mathscr{H}_{i,j} = -J\sum_{i,k}\left(\mathbf{s}_i \cdot \mathbf{s}_j\right), \tag{2.15}$$

which is known as the Heisenberg Hamiltonian, [25]. Here J is the exchange integral [24, 13] which represents the strength of exchange interaction, while s_i and s_j are neighbouring spins. In ferromagnets J is positive, favouring parallel alignment of neighbouring atomic magnetic moments. Negative values of J results in an anti-parallel alignment of neighbouring atomic magnetic moments, known as antiferromagnetic ordering. But for most materials, the exchange interaction is not strong and there is no magnetic ordering. Despite being negative for the hydrogen molecule, Heisenberg argued that the sign of J might reverse at some critical inter-atomic distance. Calculations of the exchange integral ab-initio are very challenging, [39]. Moreover, direct exchange only considers the valence electrons of nearest neighbour atoms. Different forms of exchange interaction have been discovered which provide magnetic ordering in different chemical situations.

Super-exchange is the coupling of the magnetic moments of two magnetic cations that are both bonded to an intermediate anion, such as in Mn-O-Mn [40]. According to the Goodenough-Kanamori rule [41], the coupling is anti-ferromagnetic where the cations have

half-filled orbitals, which is usually the case, and ferromagnetic where one is half-fill and the other is full. This interaction is strongest when the cation-anion-cation bond angle is 180 degrees and minimal at 90 degrees. It is the dominant cause of magnetic ordering insulators, antiferromagnetic, ferrimagnetic or ferromagnetic.

RKKY exchange is named after the main contributors, Ruderman, Kittel, Kasuya, Yosida [42]. It is the theory of exchange coupling between 3d electron spins which is mediated by conduction band electrons and is the dominant cause of magnetic ordering in conducting ferromagnets.

Antisymmetric exchange or Dzayoshinskii-Moriya interaction (DMI) is found only in crystals with no inversion symmetry and it promotes canted spins instead of parallel/antiparallel spins [43]. It arising from the spin-orbit interaction and promotes helical, conical and skyrmion lattice phases. It is written in a similar form to the Heisenberg exchange except the scalar product is replaced with a vector product,

$$E_{DMI} = D_{i,j}[\mathbf{S}_i \wedge \mathbf{S}_k], \tag{2.16}$$

where E_{DMI} is the DMI energy between two spins S_i and S_j and D_{ij} is the DMI vector. In the case of the super-exchange interaction, the DMI vector $D_i j$ is proportional to the vector product of the vectors from the intermediary ion to the magnetic ions, $D_{ij} \propto r_i \wedge r_j$.

In ferromagnetic systems where the magnetisation varies slowly with respect to the lattice constant, the exchange energy can be expanded in the small angle limit. Now the exchange energy density for continuous magnetisation can be expressed as quadratic with respect to the gradient of magnetisation as,

$$\varepsilon_{\text{exch}} = A_{\text{ex}} \left(\nabla \mathbf{M}\right)^2, \tag{2.17}$$

where A_{ex} is the exchange constant of the material, $A = NJ/2a$, with N the number of nearest neighbours and a the lattice constant. The exchange stiffness is more useful as it is

abstracted from consideration regarding the crystal lattice and is measured experimentally by a variety of techniques [44]. However, DMI must be treated separately because it is qualitatively different.

On the mesoscopic scale, the different mechanisms of the exchange interaction are lumped together into an effective exchange stiffness as in Eq. (2.17). Moreover, this description is commonly used in micromagnetic simulations, regardless of whether the exchange interaction takes the form of direct exchange, super-exchange or RKKY interactions. Furthermore, the exchange interaction is usually considered to be isotropic, even when the structure of the material is not. The effect of the crystal lattice structure on the magnetisation is known as magneto-crystalline anisotropy.

2.1.4 Magneto-crystalline anisotropy

The crystal structure of a material is coupled to its magnetisation principally through the spin-orbit interaction [13]. This couples the spin moments to the orbital moments, which are coupled to the crystal electric field. The result is that magnetisation favours certain crystallographic axes or planes, known as easy axis or easy plane anisotropy. A much weaker contribution to anisotropy comes from the magnetic dipolar interactions between atoms in non-cubic crystal lattices. Both types of magneto-crystalline anisotropy can be described by a phenomenological model that parameterises the anisotropy energy in terms of the angle between the anisotropy axis and the magnetisation. It takes the form of a power series expansion, typically, only the first term is necessary,

$$\varepsilon_{\mathrm{a}} = -K_1 \left(\hat{M} \cdot \hat{u}_1\right)^2 - K_2 \left(\hat{M} \cdot \hat{u}_2\right)^4 \tag{2.18}$$

where K_n is the amplitude of anisotropy of the nth degree along the axis $\hat{u}_n$. Only even powers of the dot product are allowed because anisotropy does not prefer one direction over another. If K is positive then the energy is minimized when $\mathbf{M} \parallel \hat{u}$, which is known

as easy-axis anisotropy. The opposite case is known as hard axis, or easy plane anisotropy and this favours magnetisation to take some position on a plane $\mathbf{M} \perp \hat{u}$. Multiple axes of anisotropy may be present depending on the crystal, for example, cubic crystals have three axes of anisotropy, while hexagonal lattices tend to have one. The pattern of magnetic domains formed in a system depends on the magnetocrystalline anisotropy.

Consider a ferromagnetic film that has easy-axis anisotropy perpendicular to the plane (PMA), with no external fields applied. The PMA favours perpendicular magnetisation, whilst the shape of the film favours in-plane magnetisation. The ratio between the demagnetising and anisotropy energy determines whether the film is magnetised perpendicular or parallel to the plane. This figure of merit is known as the Q factor for magnetic films and takes the form,

$$Q = \frac{2K}{\mu_0 M_s^2} \tag{2.19}$$

where K is the magnetocrystalline anisotropy, M_s is the saturation magnetisation and Q is the quality factor. If $Q > 1$ the magnetisation is orientated perpendicular to the plane, giving rise to stripe domains and bubble domains can be formed as shown in fig. (2.6) [4]. In the case when $Q < 1$, magnetisation is uniform for infinite films, and forms in-plane domains in finite-size films, as shown in fig. (2.1), often called Landau or flux closure patterns [26].

2.1.5 Yttrium Iron Garnet

Yttrium Iron Garnet is an important material for the study of spin waves due to its exceptionally low damping, $\alpha 10^{-5}$, which gives spin-wave lifetimes many times greater than other magnetic materials [6]. It has a complicated garnet structure, with a cubic unit cell measuring 12.376 ± 0.004Å on each edge and containing 24 Y3+ ions, 40 Fe3+ ions, and 96 O2- ions. Super-exchange is responsible for the ferrimagnetic order of YIG, which comes from the 24 Fe3+ ions in the tetrahedral site (d) being anti-ferromagnetically coupled to the 16 Fe3+ ions in the octahedral site (a). Naively, this gives the unit cell a magnetic moment of

approximately 40 Bohr magnetons and therefore a magnetisation saturation of M_s $195kA/m$. However, the configuration is more complex and the experimental value is $Ms \approx 140$ kA/m [45].

Despite having 40 Fe3+ ions in the unit cell, only one band, known as the ferromagnetic band, lies within room temperature energies, making the mesoscopic scale approximation of YIG as a homogeneous ferromagnetic material valid at low temperature. The exceptionally low damping comes from two attributes. Firstly, the lack of conduction electrons which prevents coupling of spin waves to electron bands. Secondly, the 3d orbital of the Fe3+ ions are half full and therefore no net orbital moment L=0, which suppresses coupling to the crystal lattice, reducing the scattering from lattice vibrations and causing the magneto-crystalline anisotropy to be small. The latter is negligible when compared to the bias fields used in experiments and is typically discounted.

2.2 Effective magnetic field

The free energy functional takes the magnetisation function and returns the scalar value of the total free energy in the system. It takes the form of a volume integral of the free energy density,

$$E_{free} = \int_V \varepsilon dV, \tag{2.20}$$

where E_{free} is the total free energy and ε is the volume density of free energy arising from the various interactions within the ferromagnet, see Sec. (2.1). A small variation in magnetisation results in a small variation of the free energy,

$$\delta E_{free} = \int_V -\delta \mathbf{M} \cdot \frac{\delta \varepsilon}{\delta \mathbf{M}} dV, \tag{2.21}$$

where $\delta\mathbf{M}$ is a small variation in the magnetisation function. At equilibrium, the free energy must be minimal and therefore $\delta E_{\text{free}} = 0$. As the amplitude of $|M|$ is constant, $\delta\mathbf{M}$ is constrained to be perpendicular to $\mathbf{M}$. Thus, $-\delta\varepsilon/\delta\mathbf{M}$ is parallel to the magnetisation at equilibrium. In general this quantity acts as an effective magnetic field,

$$\begin{aligned}\mathbf{H}_{\text{eff}} &= -\frac{\delta\varepsilon}{\delta\mathbf{M}} \\ &= -\frac{\partial\varepsilon}{\partial\mathbf{M}} + \frac{\partial}{\partial r_i}\frac{\partial\varepsilon}{\partial\frac{\partial\mathbf{M}}{\partial r_i}},\end{aligned} \tag{2.22}$$

where $\mathbf{H}_{\text{eff}}$ is the effective field. It is so called as it combines all the interactions within a ferromagnet into a single effective magnetic field that exerts torque on the magnetisation just as a true magnetic field. This is a key quantity that feeds into the equation of motion of magnetisation.

This variational approach was used by Landau and Lifshitz to determine the structure of magnetic domains [26]. Where competition between the exchange energy, which dominates on local length scales, and the demagnetisation energy which dominates at longer lengths scales, naturally gives rise to domains of uniform magnetisation, separated by domain walls of tightly curving magnetisation. The domains cost demagnetising energy while the domain walls cost exchange energy.

The magnetic structure is further broken up by the presence of grain boundaries between different crystal grains in a material. In this way, ferromagnetic materials do not always possess a strong net magnetic moment. However, they can be induced to do so by application of a strong enough magnetic field to align the magnetisation. When the field is removed a net magnetic moment remains. The magnetisation state depends on the history of the magnetic field, a property known as hysteresis. It underpins magnetic data recording technologies.

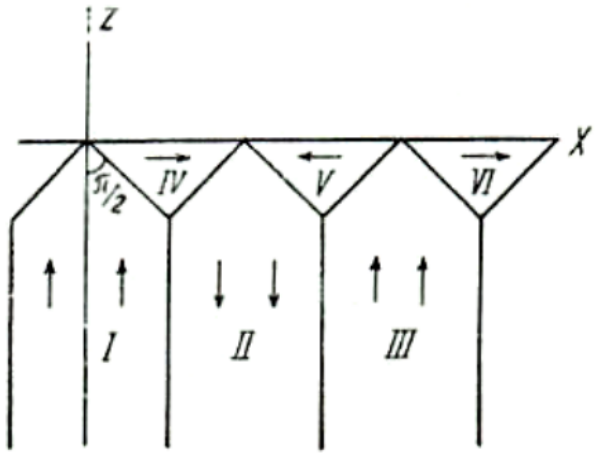

Fig. 2.1 Original sketch of magnetic domains at the edge of a ferromagnetic film. The orientation of domains are shown by arrows. Stripe domains terminating in triangle domains such that the magnetisation flux forms a closed loop, minimising the magnetostatic energy.

2.3 Equation of motion

The equation of motion for magnetisation was developed by Landau-Lifshitz, who predicted collective Larmour precession and showed that it was responsible for the high-frequency permeability of ferromagnets [26]. It described the damped precession of magnetisation under the influence of the effective magnetic field, Eq. (2.22).

$$\frac{\mathrm{d}\mathbf{M}}{\mathrm{d}t} = -\gamma \mathbf{M} \wedge \mathbf{H}_{\mathrm{eff}} + \lambda \mathbf{M} \wedge (\mathbf{M} \wedge \mathbf{H}_{\mathrm{eff}}), \tag{2.23}$$

where, γ is the gyromagnetic ratio [13, 23], λ is the phenomenological damping parameter.

Different variations of this equation can be found in the literature which have been developed to tackle particular problems, such when the magnitude of M_s is reduced due to demagnetisation [46], or to account for spin transfer torque [47]. However, the most common variation is that of Gilbert, which is equivalent to Landau and Lifshitz original equation when damping parameter is small [48]. It takes the form,

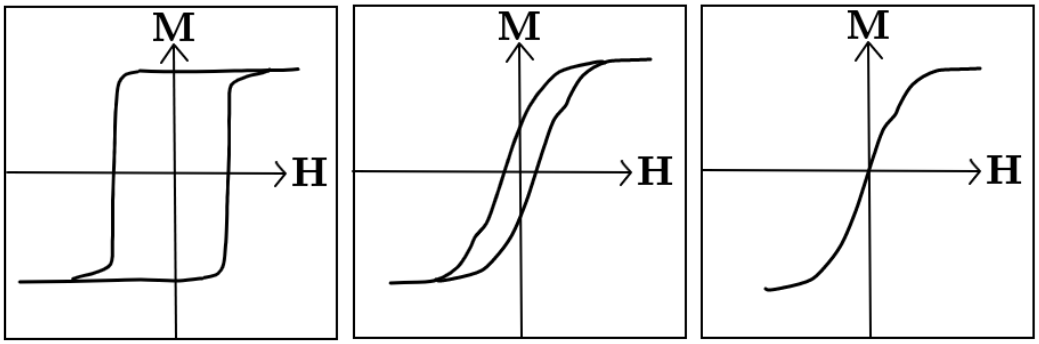

Fig. 2.2 Sketch of major hysteresis loops of ferromagnets. The Y-axis is the total magnetic moment, which at its maximum when the magnetisation is saturated, whilst the x-axis is the bias field. Left) Hysteresis of a hard ferromagnet along its easy axis of magneto-crystalline anisotropy. Centre) A soft ferromagnet. Right) A paramagnet, it has no spontaneous magnetisation when the external field is zero, but becomes magnetised when a field is applied.

$$\frac{\mathrm{d}\mathbf{M}}{\mathrm{d}t} = -\gamma \mathbf{M} \wedge \mathbf{H}_{\mathrm{eff}} + \alpha \mathbf{M} \wedge \frac{\mathrm{d}\mathbf{M}}{\mathrm{d}t}, \tag{2.24}$$

where α is the Gilbert damping parameter.

In the simplest case, all varieties describe the damped precession of magnetisation, which spirals in towards the equilibrium position, as depicted in fig. (2.3). However, it is a non-linear, integral differential equation with no general solution. The full range of phenomena is much greater and more interesting, from the formation of different domain patterns to the gyration of magnetic vortices and more. In general micromagnetic simulations are required to integrate a trajectory from initial conditions but an analytical solution can be found under certain circumstances. At low energies, the magnetisation does not deviate far from equilibrium and the LL equation can be linearized. The demagnetising field can be calculated analytically for systems with convenient symmetry.

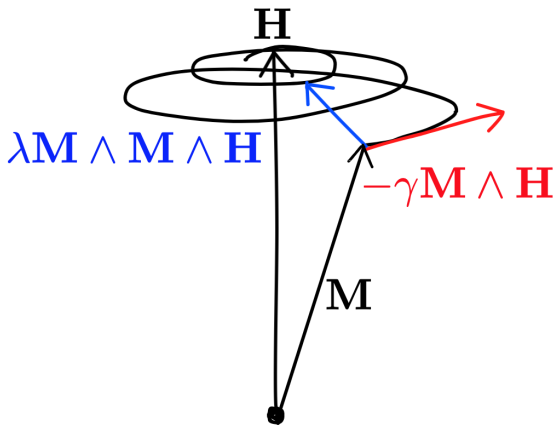

Fig. 2.3 Sketch of magnetic damped magnetic precession described by the Landau-Lifshitz equation. Red shows the precessional term, while Blue shows the damping term. The trajectory magnetisation deflected from equilibrium is a spiral inwards to the equilibrium. Note that the damping is exaggerated in this sketch to be visible.

2.4 Ferromagnetic resonance

In 1946, Griffiths measured an anomalous frequency-dependent conductivity in ferromagnets [49]. Two years later, Kittel successfully calculated the frequency of uniform, ferromagnetic resonance (FMR) of ellipsoids magnetised to saturation with his famous formula [50]. If an elliptical sample is magnetised by to saturation by bias field **H** that is orientated along one of the principle axes of the ellipse, the frequency of uniform precession is given by,

$$\omega_{\text{FMR}} = \gamma\sqrt{\mathbf{H}\left(\mathbf{H}+\bar{N}\mathbf{M}\right)}, \tag{2.25}$$

where **H** is the saturating external field and the demagnetising field is given as a proportion of the static magnetisation **M** according to the demagnetising tensor $\bar{N}$ of the system. It should be pointed out that as the magnetisation remains uniform throughout, therefore, the frequency does not depend on the exchange interaction at all. In the case of ferromagnetic films this reduces to,

$$\begin{aligned} \omega_{\parallel} &= \gamma\sqrt{\mathbf{H}\left(\mathbf{H}+4\pi M_s\right)}, \\ \omega_{\perp} &= \gamma\left(\mathbf{H}-4\pi M_s\right)\right), \end{aligned} \tag{2.26}$$

where $\omega_{\parallel}$ and $\omega_{\perp}$ are the FMR frequencies for a film magnetised parallel and perpendicular to its plane respectively. Magneto-crystalline anisotropy can be incorporated as an effective demagnetising field $H_K = -\bar{N}_K \cdot \mathbf{M}$, where K is the first order anisotropy constant, H_K is the effective field of anisotropy and $\bar{N}_K$ is the effective demagnetising tensor for anisotropy. For a film with perpendicular easy axis anisotropy, the FMR frequency is given by,

$$\omega_{\perp} = \gamma\left(\mathbf{H} + \frac{2K}{M_s} - 4\pi M_s\right), \tag{2.27}$$

where K is the first order easy axis anisotropy constant. In this case, the anisotropy reinforces the bias field and increases the frequency of FMR.

The Kittel formula describes uniform precession, which in Fourier space corresponds to $k = 0$. This can be considered a limiting case of the more general phenomena of waves of magnetic precession where $k \neq 0$. These waves of precession are known as spin waves.

2.5 Spin waves

First theorised by Bloch to explore the origins of ferromagnetism and explain the dependence of magnetisation saturation at low temperatures [51]. The study of spin waves has developed into a growing field of its own, known as Magnonics [5, 6].

The spin-wave spectrum has two distinct limiting cases of low and high k. The development of spin-wave theory grew from either limit and met in the middle.

In the limit, $k \to 0$, the exchange interaction contribution to the free energy tends towards zero. This is due to the exchange interaction being proportional to the change in

magnetic angle with position $\nabla\mathbf{M}$, which tends to zero when $\mathbf{M}$ is uniform. Therefore, the magneto-dipole interaction dominates in what is known as the magnetostatic regime. As the group velocity of spin waves are much lower than c, retardation effects can also be excluded. The dispersion of magnetostatic spin waves depends strongly on the geometry and equilibrium magnetisation configuration. In a confined system a discrete spectrum of standing modes is formed [52]. When positioned close enough these modes can interact and in an extended system, continuous bands of spin waves form [28, 53, 54]. The dispersion of these magnetostatic waves can be derived from Walker's micromagnetic equations [55] which themselves are a solution of Maxwell's equations in a medium with a chiral permeability [13, 34].

As k increases, the exchange interaction overtakes the demagnetising field as the dominant term in the effective field. This intermediate regime is known as the dipole-exchange regime and the dispersion relation of magnetostatic modes can be extended to include the effect of the exchange interaction [56].

Damon and Eshbach studied the spectrum magnetostatic spin waves in uniformly magnetised ferromagnetic films [28, 57]. They showed that the spectrum of magnetostatic waves spectrum smoothy transitions into the spectrum of exchange spin waves, tying together the quantum mechanical and classical theories of spin waves. They also showed the surface character of magnetostatic spin waves when $M \perp k$. For the case of uniformly magnetised ferromagnetic films there exists three limiting cases according to the relative orientation of the magnetisation and wave vector.

- $k \parallel \mathbf{M}$ and $\mathbf{M} \perp \hat{n}$, Backward volume geometry
- $\mathbf{M} \parallel \hat{n}$, Forward volume geometry
- $k \perp \mathbf{M}$ with $\mathbf{M} \perp \hat{n}$, Damon Eshbach geometry

where $\hat{n}$ is the surface normal of the film.

Kalinkos derived an approximate dispersion relation for the uniform thickness modes [56] which are used here. In principle there is a series of thickness modes for spin waves in the forward and backward volume geometries. In the latter these draw closer together as k sweeps away from $\mathbf{M}$, eventually coming together as one in the surface wave geometry, as shown in fig. (2.5). However, it is reasonable to restrict our analysis to the uniform thickness mode as they are most strongly excited by external fields and tend to dominate the dynamic response [13]. Furthermore, in the limit of $k \to 0$ they are the only modes with finite group velocity. They take the following forms,

$$\omega^2 = \begin{cases} \omega_{ex}\left(\omega_{ex} + \omega_M \frac{1-e^{-kd}}{kd}\right), & \text{Backward volume} \\ \omega_{ex}\left(\omega_{ex} + \omega_M\left(1 - \frac{1-e^{-kd}}{kd}\right)\right), & \text{Forward volume} \\ \omega_{ex}\left(\omega_{ex} + \omega_M\right) + \frac{\omega_M^2}{4}\left(1 - e^{2kd}\right), & \text{Surface} \end{cases} \tag{2.28}$$

where ω_{ex} is the contribution to the frequency from the internal field and exchange interaction, while ω_M is the contribution from the dynamic demagnetising field field $\omega_M = \gamma M_s$,

$$\omega_{ex} = \begin{cases} \gamma H + A_{ex}\omega_M k^2, & \text{Backward volume and Damon-Eshbach geometry,} \\ \gamma(H - M_s) + A_{ex}\omega_M k^2, & \text{Forward volume geometry,} \end{cases} \tag{2.29}$$

where the term $A_{ex}\omega_M k^2$ is the contribution to the dispersion from the exchange interaction. It is quadratic at low k, at higher k this model breaks down as the spin-wave dispersion must flatten out at the Brillouin zone of the crystal lattice.

For larger k, the exchange interaction dominates the effective field and the profound difference that different geometries made in the magnetostatic case are drastically minimised and serve only to perturb the dispersion [13, 58, 59]. In Yttrium Iron Garnet, the parabolic

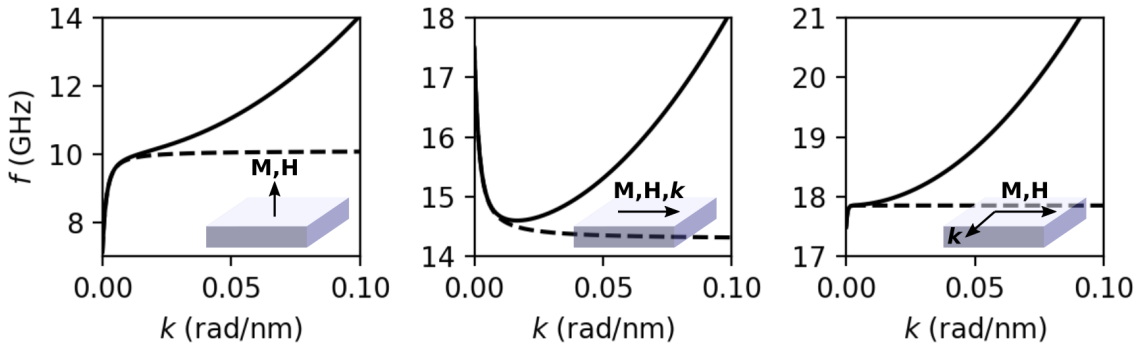

Fig. 2.4 Spin wave dispersions for spin waves in a film [56], $Ms = 0.25$ T, $|H_{\text{ext}}| = 0.5$ T, $A_{\text{ex}} = 5.34e-17$ m^{-2} and thickness $d = 1\,\mu$m. Left. Forward volume geometry, the dispersion is isotropic in the plane of the film. Centre. Backward volume geometry. Right. Surface spin wave geometry. The orientation of magnetisation, external field and wave vector are shown as a sketch inset to each panel. The dispersion in the dipole-exchange and magnetostatic regimes are shown as solid and dashed lines respectively.

dispersion obtained by micromagnetics has been shown to deviate from the measured dispersion by 5% for $k \approx 10\%$ of the way towards the BZ boundary along the $\Gamma - \text{H}$ direction, representing 0.1% of the BZ by volume, see [60]. In the simplest model of a chain of spins modelled with the Heisenberg Hamiltonian eq. (2.15), the dispersion takes the familiar cosine shape found in tight-binding models of electrons [13].

2.5.1 Magnonic crystals

Chapters 3 and 5 are concerned with spin-wave propagation in periodic magnetic media known as magnonic crystals [5]. The periodic modulation is used to open band gaps in the spin-wave spectrum, which are in turn used to control the propagation of spin waves. For this reason, they are considered an important component of future magnonic devices, where information is carried by spin waves. In this respect, they can be considered the magnonic equivalent of semiconductors, or photonic crystal which take similar roles in electronics and photonics [61].

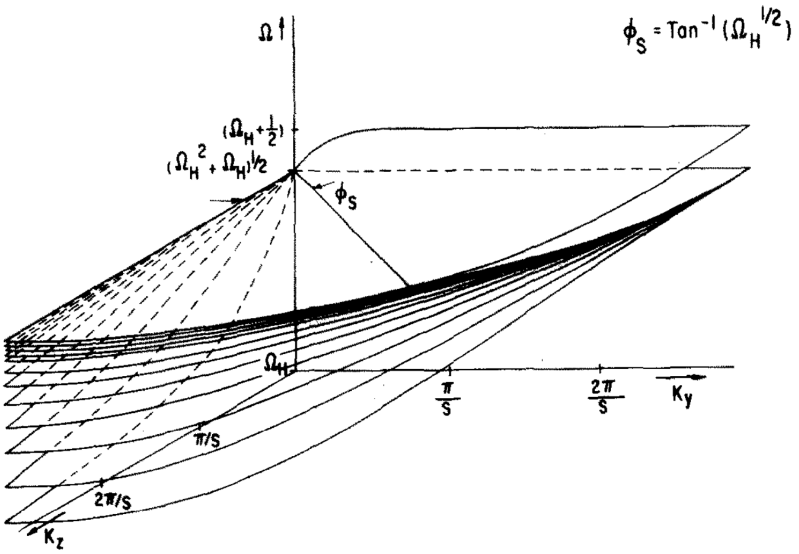

FIG. 3. Magnetostatic mode spectrum of a ferromagnetic slab magnetized in its plane.

Fig. 2.5 Damon and Eshbach's original sketch of the dispersion of magnetostatic spin waves in a ferromagnetic film magnetised in its plane along the z axis [28]. The spin wave modes split from ferromagnetic resonance at $k = 0$, into many backward volume thickness modes which sweep up into a single surface wave as the angle of k changes from parallel to perpendicular to the static magnetisation.

In principle, magnonic crystals can be realised by periodic modulation of any parameter that affects spin dynamics [62]. Traditionally, geometrical patterning is used [63–66] but magnonic crystals made using different magnetic materials, [67, 68] modulated applied magnetic field [69] or heating [70, 71] have also been studied. Of these methods, only periodic modulation of the temperature or applied field can be switched on and off. This dynamic control is desirable, however, these methods require a constant delivery of energy and additional components which take up space. One promising solution is the development of magnonic crystals which use periodic modulation of the magnetisation configuration to open band gaps [72–75]. They are of special interest as they may enable reprogrammable magnonic crystals and other devices. For a review of this topic see [14].

2.6 Bubble domains

Magnetic bubble domains make multiple appearances in this work so it is convenient to introduce them here. They are cylindrical domains of reversed magnetisation, in an otherwise uniformly magnetised sample, fig. (2.6). They can be formed in magnetic films and platelets that have easy axis magneto-crystalline anisotropy directed perpendicular to the plane. The ground state of such films, in the absence of an external field, is a labyrinth of perpendicularly magnetised stripe domains. When an external field is applied perpendicular to the film, the domains parallel to the field are enlarged, at the expense of the domains opposing the field. As the field increases, the stripe domains break into individual bubble domains. Ultimately, above a critical field, these bubble domains are unstable and collapse into a uniformly magnetised state. An example of this behaviour is shown experimentally in Chapter 4.

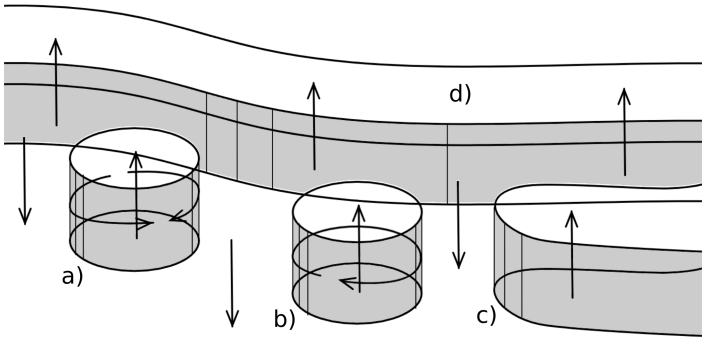

Fig. 2.6 A sketch of magnetic domains in a perpendicularly magnetised film. Arrows indicate the direction of magnetisation while shaded surfaces indicate domain walls. a) Bubble domain in the onion state. b) Bubble domain in the skyrmion state. c) A stripe domain terminating. d) A continuous stripe domain.

In the 1970s, bubble domains were a hot topic of research as their mobility and long lifetimes led to their application in bubble memory devices proposed by Bobeck, [4, 76]. Traditionally research was focused on the stability [77], size and mobility of the bubbles [78]. From the LLG equation Eq. (2.24), Thiele derived an equation of steady state motion for magnetic domains and used it to predict the translational motion of bubble domains [29]. It takes the form,

$$\mathscr{G} \wedge \mathbf{v} - \mathscr{D} \cdot \mathbf{v} + \nabla U = 0, \tag{2.30}$$

where U is the potential energy as a function of position of the spin texture, $\mathbf{v}$ is the velocity, $\mathscr{G}$ is the magnetic gyro-vector, $\mathscr{D}$ is the dissipation dyadic, which take the form,

$$\begin{aligned} \mathscr{G} &= -\iint \frac{1}{M_s \gamma} \mathbf{M} \cdot (\nabla_x \mathbf{M} \wedge \nabla_y \mathbf{M}) dxdy, \\ \mathscr{D} &= -\iint \frac{\alpha}{M_s \gamma} \nabla_i \mathbf{M}_k \nabla_k \mathbf{M}_j dxdy, \end{aligned} \tag{2.31}$$

The gyro-coupling vector has its genesis in gyration term of the Landau-Lifshitz equation and it causes spin textures to gyrate about their equilibrium position, whilst the dissipation term is derived from the damping term and is responsible for the return to equilibrium. While all spin textures have a dissipation dyadic, only certain spin textures have a gyro-coupling vector. It is determined by the topological winding number of the magnetisation unit vector field onto a unit sphere.

A central example is the magnetic bubble domain. There are different forms of magnetic bubble, depending on how the magnetisation in the domain wall is aligned. The two important cases for this thesis are the skyrmion like bubble domain and the onion bubble domain, both are sketched in fig. (2.6). The difference is that the skyrmion like bubble domain has a domain wall in which the magnetisation circulates continuously, with no defects, either clockwise or anticlockwise. The magnetisation unit vector field wraps the unit sphere once. This is the definition of a magnetic skyrmion and it comes with a finite gyro-coupling vector. On the other hand, the onion bubble domain is characterised by half the domain wall circulating clockwise and half circulating anti-clockwise. This results in two magnetic poles, one where the magnetisation is converging and one where it is diverging, giving the onion bubble domain a finite in-plane dipole moment. In this case, the magnetisation of one half wraps half the unit sphere, but the other half unwraps it to give a net-zero wrapping. Therefore, the onion state does not have a gyro-coupling vector.

In this treatment, the spin textures were assumed to be rigid. Whereas in reality domain walls are at liberty to flex and oscillate [79]. In the case of bubble domains, the oscillation of the domain walls gives the moving domain an effective mass that has implications for the translational movement of bubble domains and skyrmions. Thiele's approach can be extended to consider the density of gyro-vector along the 1D line of the domain wall and it has been shown that in a skyrmion like a bubble domain, spin waves have a different group velocity depending on which direction they are travelling in [80]. This has motivated various studies into the internal modes of bubble domains [81, 80, 82].

2.6.1 Internal modes of a skyrmion-bubble domain

Several internal modes of skyrmion like bubble domains have shown to reside below the spin-wave continuum [83]. These internal modes consist of oscillations in the domain wall with $k_m = \pm m/r$ which are non-reciprocal with respect to clockwise and counter-clockwise due to the gyro-coupling effect [84]. It has been shown that as the bias field increases, the number of internal modes below the magnon continuum decreases [82], thus only the low order modes need be considered and typically only the lower frequency direction is observed. We enumerate them below and their corresponding diagrams are shown in fig. (2.7).

- $m = 0$, breathing mode, uniform expansion and contraction of radius
- $|m| = 1$, gyration mode, orbit of the domain centre about its equilibrium position
- $|m| = 2$, elliptical deformation, rotating ellipse
- $|m| = 3$, triangular deformation, rotating triangle

In the cases where the internal modes intersect with the spin-wave continuum, it has been shown that spin waves scatter asymmetrically from skyrmions, creating a hall effect for spin waves and imparting momentum to the skyrmions [85].

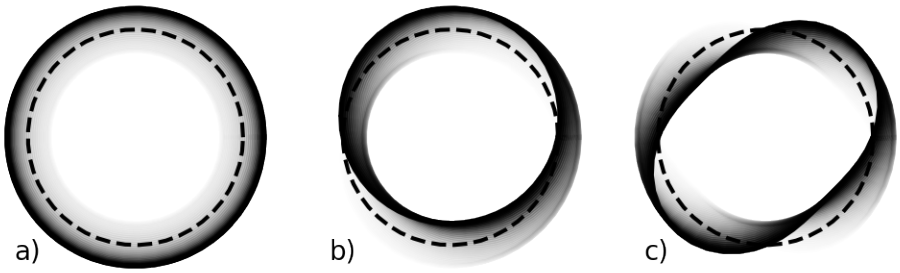

Fig. 2.7 Illustration of the low frequency modes of a bubble domain wall at an instance in time. a) Breathing mode b) gyration mode c) elliptical mode. The dashed loop indicates the equilibrium position of the domain wall. The loop line shows the current position of the domain wall whilst faded lines show the preceding positions.

Fig. (2.7), shows a schematic of the internal modes of a bubble domain. The most important mode is the breathing mode, where m=0, the bubble expands and contracts uniformly [86]. It is the only mode which changes the dipolar moment of the domain and thus can be excited by an A.C. magnetic field directed perpendicular to the film. Expansion of the domain wall costs exchange energy, whilst the contraction costs demagnetisation energy. Next is the clockwise and counterclockwise gyration modes, $m = \pm 1$. These are the only modes which change the centre mass position of the domain or leave the domain shape unchanged. The lower frequency of the pair is a Goldstone mode that corresponds to the translational motion of the domain or lattice of domains. The action of clockwise and counter-clockwise modes together results in a hypo-cycloidal orbit around the equilibrium position [87]. Finally, we consider the elliptical modes, where $m = \pm 2$, they take the form of an elliptical deformation of the domain which rotates clockwise or anti-clockwise at different frequencies. To describe the internal modes of skyrmions and skyrmion like bubbles, how they interact with spin-wave continuum and accurately predict their inertia, remain the subject of ongoing research in this field.

2.7 Micromagnetic simulations

Micromagnetic simulations have become an important tool in magnetism research ,[30–32]. They form the third pilar, after theory and experiment and compliment both by helping to interpret results and guiding new efforts. They integrate the Landau-Lifshitz equation in incremental steps, evaluating the effective field according to equation (2.22) before updating the magnetisation configuration typically using an adaptive time step integration scheme such as Runge-Kutta 4/3 [88]. The volume is discretised into a mesh of cells each with its magnetic moment that represents the average magnetisation in that volume [89]. There are two choices in how the mesh is generated, finite difference methods use cuboid cells which are less demanding in memory so have the advantage of higher cell resolution, while finite element methods use a variable mesh of tetrahedra enabling the more accurate representation of curved geometries. In both cases the angle between neighbouring spins must remain small at all time, otherwise, the small-angle approximation used to calculate the exchange fails.

In this thesis, numerical simulations were performed with Mumax3, a GPU accelerated micromagnetic package which boasts high performance for large simulations. It uses a finite difference time domain (FDTD) methods to solve the Landau-Lifshitz equation eq. (2.23). Details of the design and verification of Mumax3 can be found in reference [32]. The practical considerations include the maximum number of cells which is determined by the available memory on the graphics card, as simulations must fit entirely into a single card. Another consideration is that the maximum angle in magnetisation between adjacent cells must be small, as the exchange interaction energy uses a small angle approximation which will overestimate the exchange energy of large angles. For Mumax3 a maximum angle of 20 degrees is recommended [32].

Chapter 3

Bloch and Zener oscillations of spin-waves

3.1 Introduction

In 1929, Bloch made the surprising prediction that electrons in a perfect lattice, when subject to a uniform electric field, do not propagate. Instead, they oscillate back and forth around a stationary mean position, the electric field increases the electron wave-vector until it reaches the band edge, where it is reflected, in a phenomenon known as Bloch oscillations (BOs) [90]. Alternatively, the electron can tunnel across to the next band, in a process as resonant Zener tunnelling or Zener breakdown. This occurs when the electric field is strong or the bandgaps are small [91]. The combination of Bloch oscillations and Zener tunnelling is known as Bloch-Zener oscillations (BZOs). Here electrons tunnel across the many bands before being reflected, resulting in oscillations periods which are an integer multiple of the BO period.

This result contradicts the common knowledge that a current will flow through a conductor when a bias voltage is applied across it. The reason is that perfect crystals do not exist in nature. Scattering from imperfections breaks the coherence of electrons, killing BOs and

enabling current to flow. Imperfections can take the form of vacant lattice sites, impurities, plane and line dislocations like grain boundaries. In natural materials, these imperfections cause the mean scattering time to be much shorter than the time period of BOs, T_B. The period of BO is inversely proportional to the lattice constant, so to reduce the time period artificially patterned materials with much longer lattice periods were required. In 1992, improvements in fabrication technology provided semiconductor superlattices of sufficient quality that Bloch oscillations of electrons were measured for the first time when a bias voltage was applied, [92]. This was soon followed by experiments showing electronic BOs at room temperature [93] and emitting THz radiation [94] among other novelties.

There is no law which gives electrons a monopoly on Bloch oscillations. In general, any periodic system which supports waves can be induced to perform BOs through a gradual change is a relevant parameter across the lattice. Recently, Bloch oscillations & Zener tunneling have been studied in optical [95–97], acoustic [98–100] and cold atom systems [101–103], while analogous effects were observed in Josephson junctions [104, 105].

On the other hand, Bloch oscillations of spin-waves have not been measured experimentally as the time period of oscillations is much greater than the spin-wave lifetime. However, the development of high-quality magnonic crystals, introduced in chapter 2, section 2.5.1, provides a solution to this problem by opening bandgaps in the spin-waves spectrum and greatly reducing the Brillouin zone. In this role, magnonic crystals perform the same function for spin-waves that semiconductor superlattices did for electrons.

On the theoretical side, spin-wave BOs have been studied in a 1D chain of Heisenberg spins, where a gradient in the bias field is used to induce Bloch oscillations [106]. This model has the advantage of being a strong analogue for tight binding electrons, replicating the same physics [23]. However, it is far removed from experimental works on magnonic crystals where dipolar and dipole-exchange waves are typically used as they are more readily excited and detected.

In this chapter, the Bloch and Zener oscillations of spin-waves in artificially periodic Yttrium Iron Garnet films are studied. First, a classical theory of Bloch oscillations is developed and then applied to the case of backward volume magnetostatic spin-waves. Micromagnetic simulations are then used to validate this theory for backward volume spin-waves in two different magnonic crystals. BOs and BZOs of spin-waves are observed in the simulations which show close agreement with the theory in the limit that the bias magnetic field is greater than the magnetisation saturation of the material. Moreover, realistic parameters are used throughout in order to describe a feasible experiment to observe Bloch oscillations of spin-waves for the first time.

3.2 Theory

Consider a spin-wave packet with a central frequency ω_0 that propagates in a magnonic crystal which is subject to a static bias magnetic field $H(x)$ that varies linearly along the x coordinate with a gradient $G = \partial H/\partial x$. The central frequency remains constant,

$$\omega_0 = \omega(k(x), H(x)) = const, \tag{3.1}$$

where $k(x)$ is the packets central wave number, which we assume to follow adiabatically with the magnetic field so as to ensure that the spin-wave dispersion relation $\omega(k,H)$ may still be introduced and satisfied for each value of x. This assumption is justified when the bias field gradient is small, $G \to 0$, such that wave-vector is effectively constant over the length scale of the lattice constant. Differentiating Eq. (3.1), we obtain,

$$\left(\frac{\partial \omega}{\partial k}\right)_H dk + \left(\frac{\partial \omega}{\partial H}\right)_k dH = 0 \tag{3.2}$$

where the first and second terms may be interpreted as the changes in kinetic and potential energy of the wave packet respectively. To conserve the frequency, the two changes must be equal and opposite. Differentiation with time we can write Eq. (3.2) as,

$$\frac{\partial k}{\partial t} = -G\left(\frac{\partial \omega}{\partial H}\right)_k = F, \tag{3.3}$$

which can be identified as the equation of motion of the wave packet under the action of the effective force F due to the non-uniform magnetic field. The central wave-vector of the wave-packet increases under the influence of this force, until it reaches the Brillouin zone boundary, where $\omega(k = \pi/a) = \omega_0$.

Bloch oscillations (BO) occur due to the wave packet making round trips within the Brillouin zone after being backscattered from the Brillouin zone boundary. In other words, the wave packet is accelerated by the gradient in the magnetic field, trading its potential energy for kinetic energy. However, it is then reflected by the lattice at the Brillouin zone boundary, trading it's kinetic energy back for potential energy and repeating the cycle. This is an adiabatic process, where the wave-packet remains in its original state. Zener tunnelling, (ZT), is a diabatic process, where the wave packet tunnels across the bandgap and into the next band. The combination of BOs and ZT is known as Bloch Zener oscillations (BZOs) and occur when wave packets perform oscillations that traverse multiple bands. First, we consider the case of Bloch oscillations in a single band.

3.2.1 Bloch oscillations in an isolated band

The period of Bloch oscillations T_B is obtained by integrating the equation of motion (3.3) as

$$T_B = -\int_{k_0}^{k_0+2\pi/a} \frac{dk}{F} \tag{3.4}$$

When F does not depend on x, it must also be independent of k, due to Eq. (3.1). Then, the wave number is expected to depend linearly on time, while Eq. (3.4) reduces to the conventional form,

$$T_B = \frac{2\pi}{aF} \text{ or } \omega_B = aF \tag{3.5}$$

where ω_B is the angular frequency of Bloch oscillations and a is the lattice period. For instance, in the previously considered case of exchange spin-waves, $F = -\mu_0\gamma G$, where μ_0 is the permeability of free space, γ is the gyromagnetic ratio, while $G < 0$ for waves with a positive group velocity. This mirrors the frequency of electronic Bloch oscillations, $\omega_{B_{electronic}} = eEa/\hbar$, where e is the electronic charge, E is the electric field and $\hbar$ is the reduced Planck constant. In the case of spin-wave Bloch oscillations, the role of the electric field E is played by the gradient of the magnetic field G, whilst the factor $e/\hbar$ is taken by $\mu_0\gamma$. For a quantum-mechanical particle, we can associate H with the potential energy, then $F = -\hbar^{-1}G$, with $-G$ being the usual mechanical force.

The trajectory of a spin-wave packet is described by the integral of the group velocity over time,

$$x(t) = \int_{t_0}^{t} \frac{\partial\omega}{\partial k} dt. \tag{3.6}$$

It is helpful to substitute Eq (3.3) to change the variable of integration from t to k. This yeilds,

$$x(t) = \frac{\partial x}{\partial\omega} \int_{k_0}^{k(t)} \frac{\partial\omega}{\partial k} dk, \tag{3.7}$$

where $\partial x/\partial\omega = 1/F = 1/\gamma G$. Evaluating the integral yields,

$$x(\omega_0, t) = \frac{1}{\gamma G} \left[\omega\left(k_0 + \gamma G t\right) - \omega(k_0)\right] + x_0(\omega_0), \tag{3.8}$$

where $\omega(k)$ is the band structure in the unperturbed system when $G = 0$. The perturbation of $G > 0$ is accounted for by the time evolution of wave-vector, $k(t) = \gamma G t + k_0$, where k_0 is the initial wavenumber and x_0 is the initial position.

$$x_0 = \omega_0 \frac{\partial x}{\partial \omega}, \tag{3.9}$$

which represents the position where $\omega(k = 0) = \omega_0$.

Eq (3.8) shows that when $G > 0$, wave-packets perform Bloch oscillations which follow a trajectory in space and time that has the same curve shape as the band structure of the unperturbed system in frequency and wave-vector respectively.

3.2.2 Zener tunneling

Zener tunnelling (ZT) is the diabatic transition from one energy level to another that can occur when the Hamiltonian is varying in time such that the separation of the two states is a linear function of time [91, 107]. In the context of the band theory of solids, ZT manifests as wave-packets tunnelling from one band to the next when accelerated by an external driving force F. As the central wave-vector approaches the avoided crossing, there is a probability that it will tunnel across to the next band (ZT) instead of being reflected (BO). Under the Landau-Zener conditions, [1], the probability of such a transition is given by the Landau-Zener formula,

$$P_D = e^{-\frac{\Delta_E^2}{h} \frac{1}{\partial_t (E_1 - E_2)}}, \tag{3.10}$$

[1]

- Separation in energy levels is linear in time
- Perturbation parameter in Hamiltonian is a known, linear function time
- Diabatic states are not coupled by the perturbation

where Δ_E is half the bandgap of the adiabatic energy levels, which avoid one another. E_1 and E_2 are the diabatic energy levels, they are not coupled and so cross one another. In our system, the diabatic states can be identified with the dispersion of backward volume spin-waves in a uniform film, folded back at the band edge to give a gapless band structure as shown in red in Fig. (3.3). Whilst the bandgap can be obtained from the band structures obtained from simulations of periodically modulated films shown in greyscale in Fig. (fig:band-gaps-forming). The diabatic bands can be approximated as linear in k by taking a Taylor expansion of the backward volume spin-wave dispersion curve at the band edge.

$$\begin{aligned} E_1 &= \hbar\omega(k) \rightarrow mk + c, \\ E_2 &= \hbar\omega\left(k + \frac{2\pi}{a}\right) \rightarrow -mk + c, \end{aligned} \tag{3.11}$$

where $m \approx \partial\omega/\partial k(n\pi/a)$ as derived from the dispersion of backward volume spin-waves, Eq. (3.13). Substitution into Eq. (3.10)

$$P_D = e^{-\frac{\Delta_E^2}{\hbar}\frac{1}{2m\gamma G}}, \tag{3.12}$$

where the bandgap $2\Delta_E$ is measured from the simulation of band structures. The intuitive result is that ZT increases when the bandgap decreases or the accelerating field increases.

3.2.3 Backward volume spin-wave Bloch oscillations

For the case of backwards volume spin-waves, the first order thickness mode is the dominant mode and has a dispersion given by Eq. (2.28) which we reprint here for backward volume spin-waves in the magnetostatic limit,

$$\omega^2 = \omega_H\left[\omega_H + \omega_M\left(\frac{1 - e^{-kd}}{kd}\right)\right], \tag{3.13}$$

here, d is the film thickness, $\omega_H = \gamma H$ and $\omega_M = \gamma M_s$ with γ being the gyromagnetic ratio in units of rad / Ts. In this limit, $k \ll \pi/c$, where c is lattice constant of the medium. Therefore the Brillouin zone (BZ) boundary associated with the lattice unit cell of the medium is inaccessible and band structure of this mode is a single curve.

The acceleration due to the field gradient is given by the partial derivative of the dispersion relation with respect to the position, $\partial\omega/\partial x$. For a linear increase in the bias magnetic field, $\partial H/\partial x = G$ it is given by,

$$\frac{\partial \omega}{\partial x} = \gamma G \frac{1 + \frac{M}{2H}\frac{1-e^{-kd}}{kd}}{\sqrt{1 + \frac{M}{H}\frac{1-e^{-kd}}{kd}}}, \tag{3.14}$$

which is non-linear and diverges when $H \to 0$ and $k \to 0$. This is problematic as the theory developed in section 3.2 assumes a uniform acceleration that does not depend on k. Fortunately, a uniform acceleration can be achieved in the limit $M_s/H \ll 1$, as Eq (3.14) tends towards a constant value.

$$\lim_{\frac{M_s}{H}\to 0} \frac{\partial \omega}{\partial x} = \gamma G, \tag{3.15}$$

In practice, it is impossible to have $M_s/H = 0$ as finite M_s is necessary for spin-waves. However, it can be approximated by subjecting the system to a uniform bias magnetic field that is much greater than the saturation magnetisation, $H_0 \gg M_s$. Therefore the angular frequency of backward volume spin-waves Bloch oscillation is,

$$\omega_B \approx a\gamma G, \tag{3.16}$$

This is analogous to the electronic case where $\omega_B = aeE/\hbar$, where e is the electronic charge, E is the electric field and $\hbar$ is the reduced Plank's constant. In the case of spin-waves, γ takes the role of $e/\hbar$ while G takes the role of E.

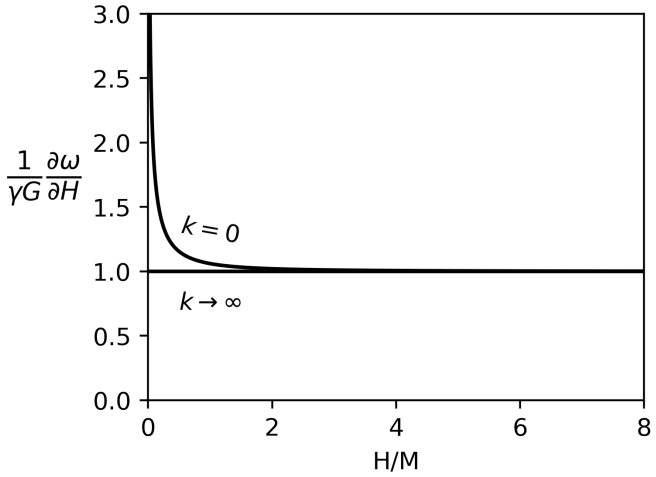

Fig. 3.1 Plot of Eq.(3.14), showing the acceleration term for backward volume spin-waves. Iso-wave-vector curves are plotted showing the limits of acceleration found at either edge of the spin-wave manifold. At $H/M_s \to 0$ the accelerating term diverges, while at $H/M_s > 2$ it is approximately linear.

Substitution of the dispersion relation Eq. (3.13) and the accelerating field Eq. (3.15) into Eq. (3.8) gives an approximate expression for the trajectory of backward volume spin-wave BOs in the limit $H >> M_s$,

$$\lim_{M_s/H \to 0} x(t) = \frac{H}{G}\sqrt{1 + \frac{M_s}{H}\left(\frac{1-e^{-kd}}{kd}\right)}\Bigg|_{k_0}^{k(t)} + x_0, \tag{3.17}$$

The dispersion relation ω is in general dependent on H, which depends on position as $H = H_0 + Gx$. This dependence is eliminated by applying a binomial expansion of the square root, $\sqrt{1 + M_s/H} \to 1 + M_s/2H$ to yield,

$$x(t) \approx -\frac{H_0}{2G} - M_s\left(\frac{1-e^{-kd}}{kd}\right)\Bigg|_{k_0}^{k(t)} + x_0 \tag{3.18}$$

where x_0 is the position of the band in space dependent on the frequency of the wavepacket ω_0. It corresponds to the position of the first band where $k = 0$. From Eq. (3.13) the frequency

is $\omega_0 = \sqrt{\omega_H(\omega_H + \omega_M}$. Rearranging to find x the expression for the position is,

$$x_0 = \frac{-(2H_0 + M_s) + \sqrt{-2H_0^2 + M_s^2 - 2H_0M_s + 4\left(\frac{\omega_0}{\gamma}\right)^2}}{2G} \tag{3.19}$$

Substitution of this expression in to Eq. (3.17) gives the trajectory of a spin-wave packet with a given angular frequency ω_0 and an initial wave-vector k_0 in the limit where $H \gg M_s$ which in it's explicit form reads,

$$\begin{aligned}\lim_{\frac{M_s}{H}\to 0} x(\omega_0, k_0, t) = &-\frac{H_0}{2G} - M_s\left(\frac{1 - e^{-(-\gamma G t + k_0)d}}{(-\gamma G t + k_0)d}\right) + M_s\left(\frac{1 - e^{-k_0 d}}{k_0 d}\right) \\ &+ \frac{-(2H_0 + M_s) + \sqrt{-2H_0^2 + M_s^2 - 2H_0M_s + 4\left(\frac{\omega_0}{\gamma}\right)^2}}{2G}\end{aligned} \tag{3.20}$$

3.3 Numerical methods

A semi-infinite film is simulated using MuMax3. A stripe of YIG like material measuring 6.144 mm along the x-axis, 1 µm along the y-axis and 1 µm along the z-axis, is discredited into $16384 \times 1 \times 1$ cuboid cells with dimensions of $0.375\mu m \times 1\mu m \times 1\mu m$, respectively. To simulate a semi-infinite film, two dimensional (2D) periodic boundary conditions are applied along the x and y-axis. This configuration has two key limitations. Firstly, magnetisation cannot vary in along either y or z directions. Therefore, the only spin-waves that can be simulated are uniform in thickness and width, $\mathbf{k} = k_x\hat{x}$. Secondly, the lengths of the cell edges are all greater than the exchange length of YIG, which is 10 nm. This means that the exchange interaction cannot be accurately simulated. However, as the equilibrium magnetisation is uniform and only perturbed by long wavelength, magneto-static spin waves the exchange interaction does not play a role in this investigation. Therefore, in this limit the simulation still provides accurate results. This is a consequence of the small-angle approximation used in MuMax 3 to calculate the exchange energy between neighbouring cells [32]. If

the simulation cell size is greater than the exchange length, non-uniform equilibrium states cannot be accurately simulated as their exchange energy is overestimated. Despite these limitations, this configuration was chosen as it enables the simulation of magnetostatic spin-waves with a high resolution in k_x, whilst staying within the graphic memory limitations associated with MuMax3.

We use material parameters similar to high-quality YIG samples. YIG is the ideal material because its low damping enables the observation spin-wave BOs as the spin-wave lifetime must be longer than the time period of BO. For a discussion of the properties of YIG, see [108, 109]. The saturation magnetisation of 200 kA / m, the exchange stiffness of $4pJ/m^3$, and zero magneto-crystalline anisotropy. The assumed value of the Gilbert damping parameter is 5×10^{-5}.

The sample is always magnetised along the x-axis due to a bias magnetic field. As spin-waves in this simulation can only propagate along the x-axis, the system is said to be in the backward volume magneto-static spin-wave geometry [13]. In a typical simulation, localised magnetic field pulses excite the uniform backward volume magnetostatic spin-wave mode and the time evolution of magnetisation is recorded by saving the unit vector of magnetisation, $\hat{M}$, periodically. As the equilibrium magnetisation is saturated along the x axis only the $\hat{y}$ and $\hat{z}$ components of magnetisation are analysed. To avoid aliasing in the frequency domain, the sampling rate is 60 GHz, yielding a maximum resolvable frequency of 30 GHz that is greater than the maximum exciting frequency of 20 GHz. Simulations were run for 2184.53 ns, gathering 2^{17} samples in time and giving a frequency resolution of 0.457 MHz.

Fourier transforms techniques [36] are used to convert results of real space - time-domain simulations into more informative representations in reciprocal space and/or frequency domain. This allows us to recover the dispersion and other characteristics of spin-waves in our system.

3.4 Periodic modulation of bias field

3.4.1 Introduction

A miniband structure can be induced by periodic modulation of any parameter that affects the magnetic energy, section (2.5.1). One way to open bandgaps this is to modulate the bias magnetic field periodically which can be achieved by the Oersted field from an array of current-carrying wires near the sample [69, 110].

$$\mathbf{H}(x) = \left[H_0 + Gx + h_0 \sin\left(\frac{2\pi}{a}x\right) \right] \hat{x}, \tag{3.21}$$

where H_0 is the bias field strength at the left edge of the sample $x = 0$, x is the position along the sample, G is the gradient of the magnetic field, h_0 is the amplitude of periodic modulation and a is the period of modulation.

To be observable, the period of Bloch oscillations must be smaller than the BVMSW lifetime in YIG, which is typically of the order of hundreds of nanoseconds [108, 109]. According to Eq. (3.16), this favours greater lattice constants and field gradients. At the same time, the lattice constant must remain much smaller than the length of the system L, within which the wave packet oscillates back and forth (Fig. 3.2 (a)), so that we could justify our approximation of an adiabatic variation of the wave-vector. To maintain the field gradient, the increase in size L required to accommodate a greater lattice constant needs to be matched by an increase of the bias magnetic field. However, the strength of the field (and therefore its gradients) achievable in the lab is limited. Here we explore the onset of Bloch oscillations as the field gradient is increased from 0 to 60 T/m. This should be feasible (albeit challenging) to achieve experimentally.

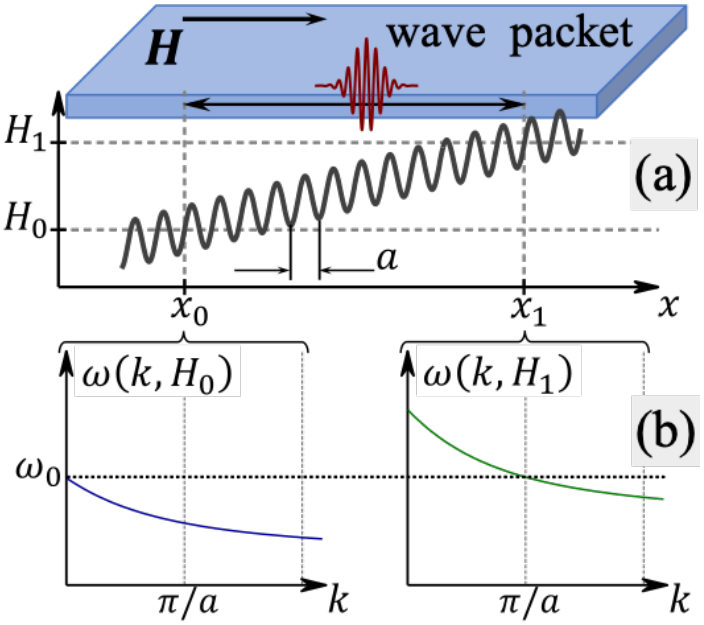

Fig. 3.2 The geometry of the problem is shown schematically. (a) Non-uniform magnetic field $H(x)$, combining the gradient and sinusoidal contributions, is applied to a uniform film of YIG along the direction of spin-wave propagation. (b) The field corresponds to the uniform ferromagnetic resonance (FMR) frequency ($k = 0$) in point x_0 (field H_0) and to the first Brillouin zone boundary ($k = \pm\pi/a$) in point x_1 (field H_1), for which the BVMSW dispersion is schematically shown. The spin-wave wave packet is excited by a uniform microwave magnetic field in point x_0 and then bounces back and forth periodically between points x_0 and x_1.

3.4.2 Opening bandgaps

The first step is to introduce a periodic modulation to the bias magnetic field. The Zeeman energy is proportional to the bias magnetic field strength and therefore it takes the role of the magnonic potential. This breaks the band structure of spin-waves in the uniform film into many minibands, just as a crystal lattice breaks the free electron dispersion into bands. Fig. (3.3) shows the opening of bandgaps as the amplitude of periodic modulation of the bias is increased.

Fig. 3.3, shows the magnonic dispersion relation calculated from the results of dynamic simulations with a broadband excitation (both in the frequency domain and reciprocal space [111]) for a uniform bias magnetic field of 0.5 T. Although the bias field and sample are

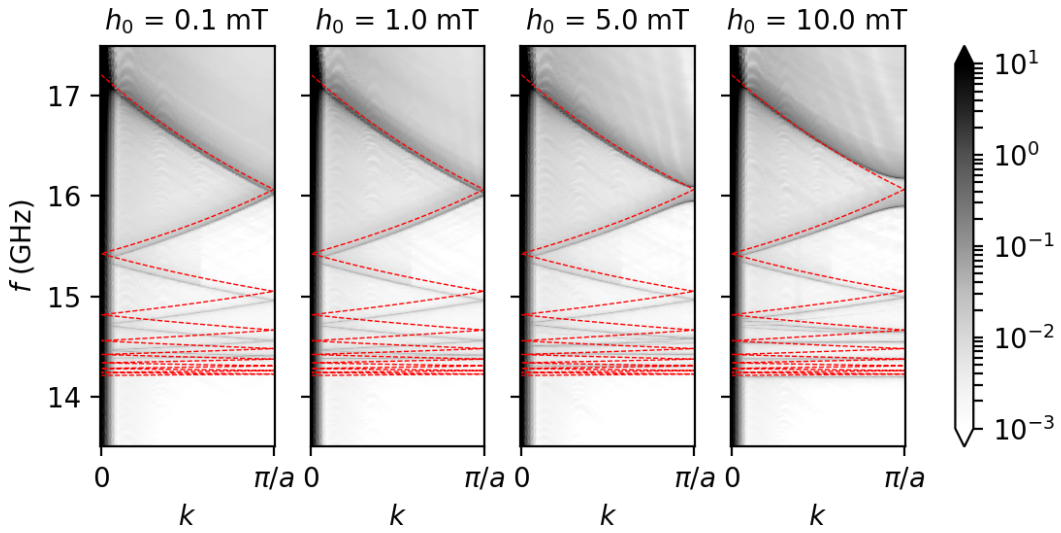

Fig. 3.3 Mini band structures induced in a uniform film through the application of periodically modulated bias fields, of varying amplitude h_0, all with a period $a = 3\mu m$ and in addition to a uniform bias field of 0.5 T. Dashed lines show the empty lattice approximation of the miniband structure; the dispersion of the uniform backward volume spin-wave in a uniform field, as described by Eq.(2.28), folded back into the 1^{st} BZ. Good qualitative agreement between the empty lattice approximation and simulated band structure is observed as $h_0 \to 0$. As h_0 is increased, bandgaps are observed to open, the largest gap being between the 1^{st} and 2^{nd} bands. The strong signal centred at $k = 0$ and extending over all frequencies is interpreted as an artefact arising from the uniform relaxation of the equilibrium state and not directly related to propagating spin-waves.

both uniform, we use the empty lattice approximation and show the dispersion folded back into the first Brillouin zone corresponding to the same sample but spatially modulated by an additional sinusoidal static magnetic field with a period of $3\mu m$. The band structure for different amplitudes of periodic field modulation from 0.1 - 10 mT are shown. Starting at the Brillouin zone centre, ($k = 0$) at the FMR frequency of about 17 GHz the frequency descends as k increases. The group velocity is negative, and so the magnonic bands are ordered in frequency from top to bottom. The periodic sinusoidal modulation induces a large first bandgap at a frequency of about 16.1 GHz, while the other (higher-order) bandgaps are significantly smaller. Since the dispersion flattens at large k values, the higher-order magnonic bands also become increasingly flat.

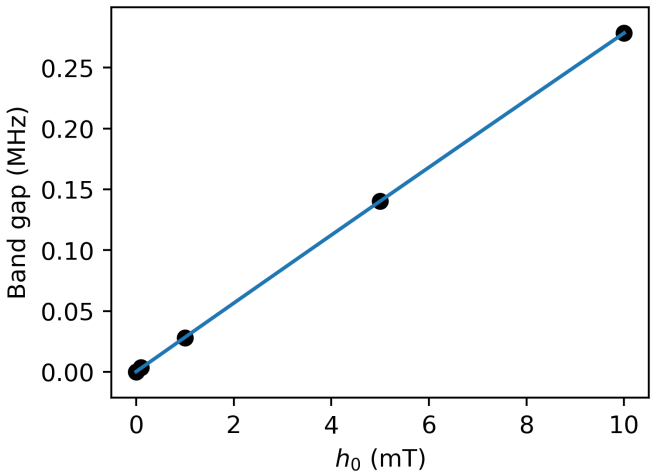

Fig. 3.4 The bandgap widths as a function of the amplitude of periodic modulation, h_0. The 1^{st} bandgap is observed to increase linearly with h_0 at a rate of 27 GHz / T.

Fig. (3.4) shows the width of the first bandgap as a function of the amplitude of periodic modulation. Therefore, the 1^{st} bandgap can be interpolated as,

$$\Delta_f = 27h_0, \tag{3.22}$$

where Δ_f is the width of the 1^{st} bandgap in units of GHz and h_0 is the amplitude of periodic modulation in units of Telsa. This interpolation can be used to inform the bandgap width parameter in the ZT probability equation, Eq. (3.12).

3.4.3 Band structure Bloch oscillations

According to Eq. (3.8) a single wave-packet should trace out a trajectory that has the same shape as the mini-band that it originates from. To reveal the shape of BOs in every band, the system was excited using a spatially uniform pulse that has a Gaussian profile in time with a central frequency of 18 GHz and a full width at half maximum of 10 MHz. This principally excites spin-waves at the edge of the 1^{st} BZ where $k = 0$ rad/m and $\omega(k = 0) = 2\pi 18$ GHz. The edge of higher BZs, where $k = n\pi/a$, are more weakly excited. The result is the synchronous generation of identical wave-packets in every band that goes on to perform BOs which are in phase with one another.

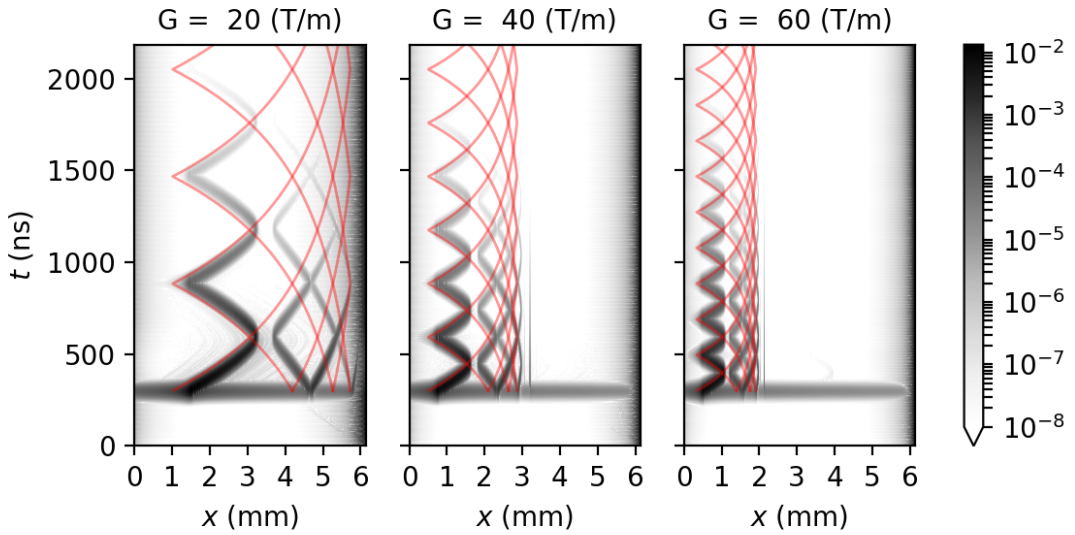

Fig. 3.5 The trajectory of spin-waves packets excited by a spatially uniform pulse centred at 18 GHz $\pm$10 MHz shown in the time/position domain. The greyscale image shows deflection angle of magnetisation from its equilibrium state saturated along the $\hat{x}$ direction. Theoretical predictions given by Eq. (3.17) are shown in red.

Simulations were conducted using a magnetic field of the form,

$$\begin{aligned}\mathbf{H}(x,t) = &\left[H_0 + Gx + h_0 \sin\left(\frac{2\pi}{a}x\right)\right]\hat{x} \\ &+ \left[Be^{-(t-t_0)^2/2\sigma^2} sin(\omega_0 t)\right]\hat{y},\end{aligned} \tag{3.23}$$

where the field oriented along the x axis is the static bias field and the field orented along the y axis is the excitation pulse. The bias field has three terms. The first is a uniform field term of 0.5 T, the second is a linear increase in the bias field with position and this provides the accelerating force on the spin-wave packet. The same bias field is used throughout this section. The final term in the bias is the periodic modulation which is responsible for opening a band structure. The excitation is uniform in space and Gaussian in time, centred at 18 GHz, with a full width at half maximum of 10 MHz and arriving at $t = 300$ ns.

Fig. (3.5) shows the trajectory of spin-wave packets excited by the pulse at $t = 300$ ns. Spin wave packets are excited at the edge of each band and perform synchronous BOs. The frequency of BOs extracted from the simulations show close agreement with Eq. (3.16),

$$\omega_B / a\gamma G = 1 \pm 0.17, \tag{3.24}$$

which is accurate within the uncertainty associated with the linewidth of the spin-wave-packets. Comparing the simulation results, shown in greyscale, against Eq. (3.17), shown in red, there is a strong agreement on the time period of oscillation, whilst the trajectory of spin-wave packets show only a loose agreement. This is expected as the BO frequency only depends on the lattice constant a and the derivative of the dispersion relation with respect to position $\partial_x \omega$, Eq. (3.16). It is independent of the shape of the original band structure. In contrast, the trajectory of spin-wave packets performing BOs depends explicitly on the original band structure, Eq. (3.17). Since the empty lattice approximation was used to calculate this band structure, the error is carried forward to yield inaccuracies, foremost of which is the lack of bandgaps and differences in position. The simulation results show a

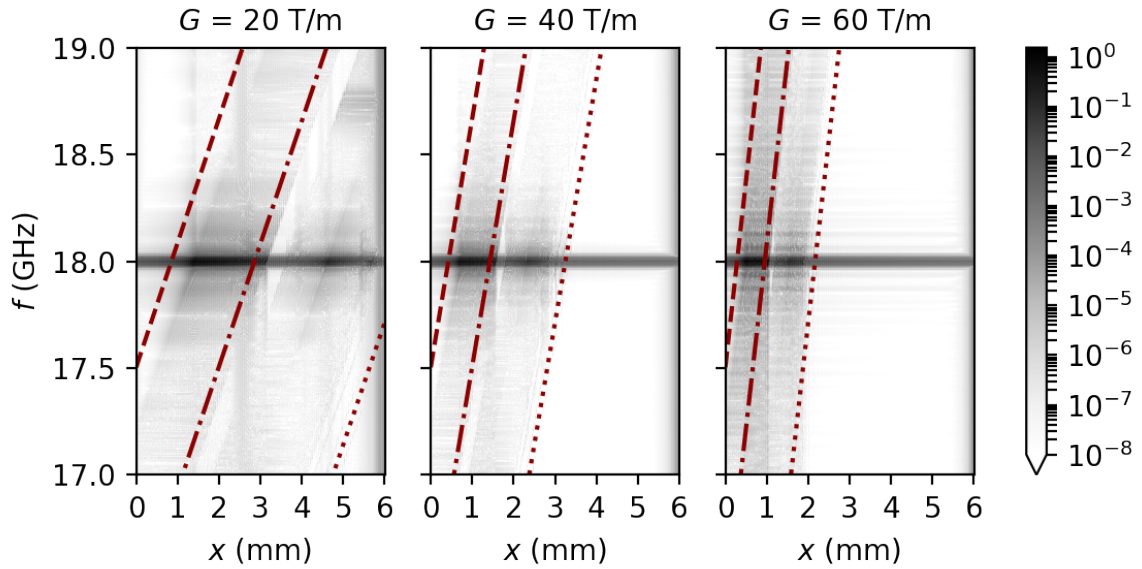

Fig. 3.6 The position/frequency representation of Fig. (3.5) obtained by Fourier transform along the time domain. Grey scale shows the deflection of the unit vector of magnetisation from the equilibrium whilst dashed lines show iso-wave-vector contours of the uniform backward volume spin-wave mode Eq. (3.13) with $k = 0$ (dashed line), $k = \pi/a$ (dashed and dotted line) and $k \to \infty$ (dotted line). An external field pulse is applied to the system at rest, exciting spin-waves. The pulse is uniform in space and has a gaussian profile in time that is centred at 18 GHz and has a full width at half maximum of 10 MHz. This excites spin-wave packets at the point on the edge of each Wannier Zeeman ladder where the conditions $k = n\pi/a$ and $\omega(k) = 18$ GHz are met.

significant bandgap between the leftmost band and its neighbour, with no discernible band-gaps between subsequent bands. This result is consistent with simulations of the mini-band structure of the film when $G = 0$ Fig. (3.3). Indeed, comparing figures (3.3,3.5) it can be seen that when rotated by 90°, the mini-band structure and wave-packet trajectories follow very similar curves.

Also, the spin-wave packets show very little broadening across many oscillation periods due to the spectral purity of the excitation pulse. Moreover, the period is the same for all minibands which indicates that the ratio of $H/M_s > 2$ is sufficiently large to justify the approximation of the acceleration term as $\partial k/\partial t \to \gamma G$, independent of k.

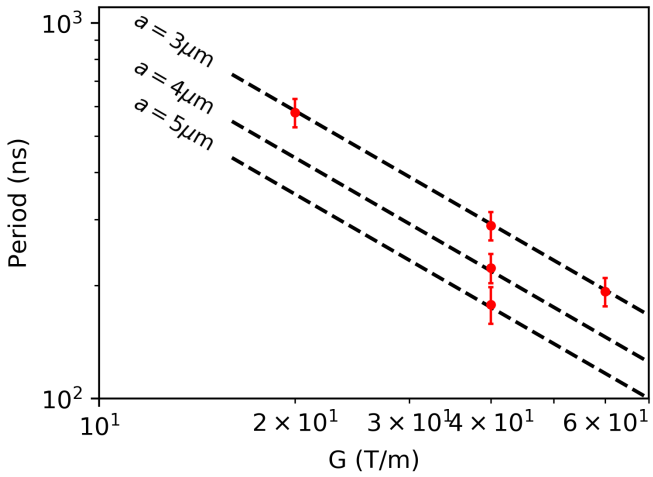

Fig. 3.7 Bloch Oscillation time periods plotted in a log/log scale as a function of field gradient. The dashed lines shows the linear theory Eq. (3.16) for different periods of field modulation, which are labelled. The red crosses show the time period taken from simulations. BOs do not occur when $G = 0$.

Fig. (3.6), show the same data, represented in the position, frequency domain. The pulse creates a strong horizontal line at 18.0 GHz. In the case where $G = 0$, the pulse excites the $k = 0$ state off-resonance, resulting in a strong line at 17.2 GHz. For the case where $G > 0$, spin-waves are excited when it intersects the Wannier ladder. The discrete Wannier states are not resolved in Fig. (3.6) as they are spaced at the $f_B = a\gamma G/2\pi$ which is on the order of 1 MHz.

3.4.4 Breathing mode Bloch oscillations

The "breathing mode" is characterised by the periodic expansion and contraction of spin-waves at the BO frequency. It is generated by an external magnetic field pulse that is tightly focussed in time and space and broadband in wave-vector and frequency, exciting every available spin-wave state at the location of the pulse. These spin-waves then propagate from the origin to perform BOs. Since every band is initiated at every possible phase of BO, the result is a bulbous envelope that expands and contracts at the BO frequency. As all states

are occupied, the envelope has reflection symmetry about the position axis, even though all constituent wave-packets have asymmetric trajectories, as shown in Fig. (3.5).

Simulations to show the breathing mode were conducted using a bias magnetic field of the form,

$$\begin{aligned}\mathbf{H}(x,t) = &\left[H_0 + Gx + h_0 \sin\left(\frac{2\pi}{a}x\right)\right]\hat{x} \\ &+ [B\,\mathrm{sinc}(\omega_C(t-t_0)\mathrm{sinc}(k_C(x-x_0))]\,\hat{y},\end{aligned} \tag{3.25}$$

where $H_0 = 0.5$ T, giving a minimum ratio of $H/M_s = 2$ which is sufficiently high to expect the acceleration of wave packets to be independent of k. $G = 0, 20, 40, 60$ T/m, in order to explore the effect of field gradient on the time period of oscillation, $A = 10$ mT, $B = 0.1mT$ and the sinc pulse excites frequencies up to $\omega_c/2\pi = f_c = 30$ GHz[2], $t_0 = 300$ ns, $k_c = \pi/0.33$ rad/ns, which is the edge of Brillouin zone of the simulation mesh.

Fig. (3.8) shows the BO breathing mode for $G = 0, 20, 40, 60$ T/m. In the case where $G = 0$, there are no BOs and spin-waves propagate with a constant velocity until they are reflected from the edge of the sample. For the simulations where there is a field gradient, BOs are induced. In all cases, the uniform mode is most strongly excited and therefore dominates the signal. This manifests in a classic breathing mode envelope which refocuses with Bloch frequencies $\omega_B/(a\gamma G) = 0.98 \pm 0.17$ which is in strong agreement with Eq. (3.16). A weaker, secondary signal is also observed which appear to have a much longer period. These are identified as the higher-order modes, which are less strongly excited by a spatially uniform pulse and have lower group velocities. The BO period of these modes appears to be much longer, which indicates that ZT between some of these bands is occurring, producing BZO which have a time period that is a multiple of the BO time period. This is likely due to the much narrower bandgaps between these bands, shown in Fig. (3.3). Tunnelling between bands is more closely inspected in subsection (3.4.5). Also, the

[2]The Fourier transform of a sinc function is a "top hat" function : $\mathscr{F}(sinc(k_0 x) = (1 \text{ where} - k_0 < k < k_0 | 0 \text{ elsewhere})$

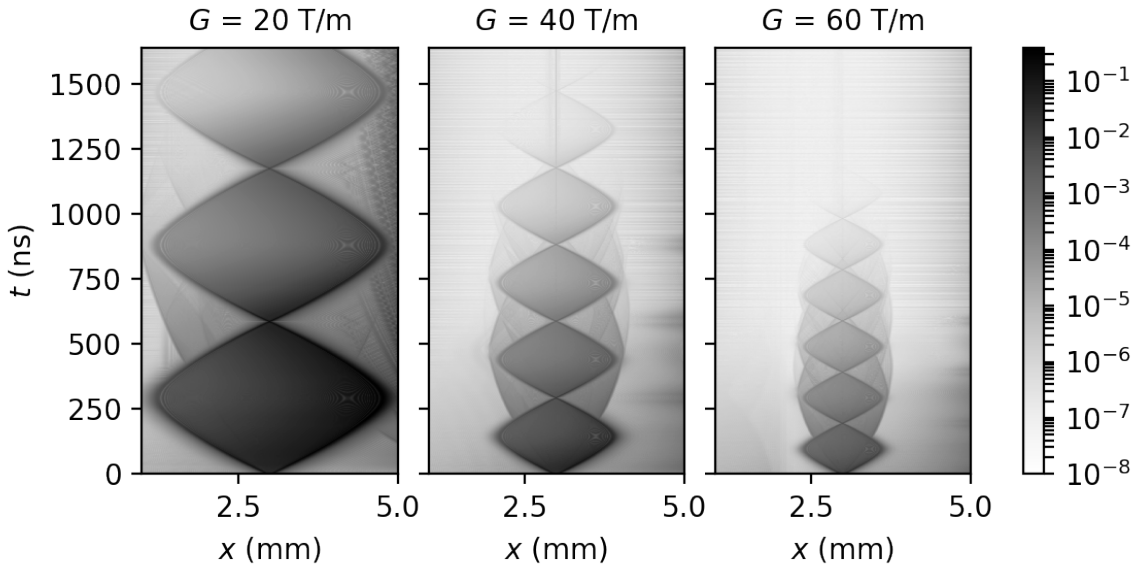

Fig. 3.8 Panes show the propagation of spin-waves excited by a broadband sinc pulse focused at $x = 3$ mm, $t = 0$ ns, for different values of bias field gradient G, as labelled inset. The deflection angle of magnetisation from the equilibrium state is shown in real-time and real space by the grey-scale colour map. At $t = 0$ ns, spin-waves with all allowed wave-vectors and frequencies are excited. They propagate from the centre of the sample at different group velocities, forming a cone of diverging spin-waves. In the case where $G = 0$, the spin-waves propagate in straight lines before being reflected at the simulation edge. In the case where $G \neq 0$, spin-wave-packets perform BOs. Individual wave-packet follows an asymmetric trajectory, identical in shape to those in Fig. (3.5). However, since all wave-vectors are excited, BOs are initiated in every possible phase of BO. Thus when viewed as a collective, they form a repeating pattern of uniform expansion and contraction that has reflection symmetry around their origin at $x = 3$ mm. magnetisation dynamics at the edge of the system at $x = 6$ mm are considered to be artefacts of simulation.

magnetisation procession observed emanating from the right edge of the sample is thought to be an artefact of simulation where further relaxation towards equilibrium occurs after the simulation is initiated.

The same data in the frequency domain is shown in Fig. (3.9). The excitation pulse is the broadband vertical line located at $x_0 = 3mm$. It directly excites all spin-wave state that intersects this position. For the case where $G = 0$ the spin-wave states are continuous bands of Bloch waves which extend across the entire sample. The 1^{st} band is most strongly excited and also has the greatest group velocity and it propagates to reflect from the edges

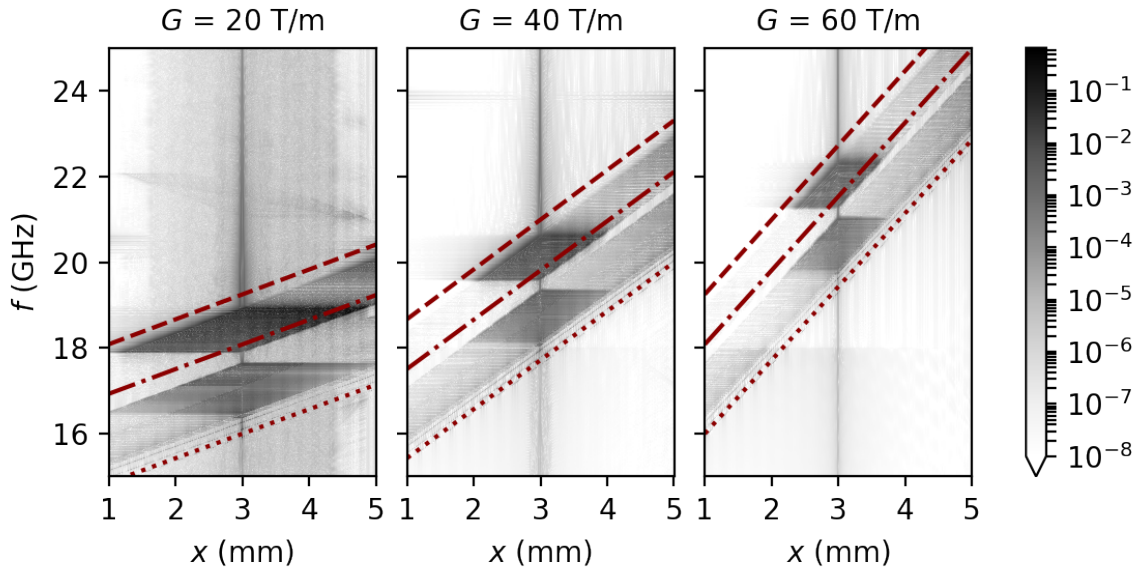

Fig. 3.9 Position frequency plot showing the Wannier-Zeeman ladder states for different field gradients. Red dashed lines show iso-wave-vector curves, indicating the upper and lower frequency bounds and the position of the first bandgap as calculated by Eq. (3.13).

of the sample while the higher-order modes have lower group velocities which decrease as frequency decreases. This manifests as shorter and shorter propagation lengths. When $G > 0$, these appear as a distinctive rhombus shape centred on the pulse and correspond to the breathing modes shown in Fig. (3.8). The rest of the ladder states are indirectly excited and are therefore very weak. Iso-wave-vector curves are plotted to show the frequency and position where $k = 0, \pi/a, \infty$ the regions where the ladder states are expected according to Eq. (3.13).

3.4.5 Zener tunneling simulations

Zener tunnelling is where a wave-packet tunnels through the bandgap into the next band. It is a diabatic transition that is caused by the acceleration of the wave-packet towards the bandgap. The probability that a single magnon makes such a transition is described by the Landau-Zener formula, Eq. (3.10). Applied to a classical wave-packet, this gives the

proportion of the packet that is transmitted across the bandgap. The remainder is reflected to perform a Bloch oscillation.

Eq. (3.12) gives the approximate transmission coefficient for spin-wave-packets accelerated toward a band gap of width Δ_ω by a gradient in the bias field G T/m. Applied to backward volume spin-waves this yields,

$$P_D(k_n, d, \Delta_\omega, G) \approx \exp\left(-\frac{1}{h}\frac{2\Delta_\omega^2}{\gamma G \frac{k_n d^2 e^{-k_n d} - d(1-e^{-k_n d})}{k_n d}\frac{\omega_m \omega_H}{\sqrt{\omega_H^2 + \omega_M \omega_H \chi}}}\right) \tag{3.26}$$

where $k = n\pi/a$, d is the film thickness, Δ_ω is the bandgap width in frequency, G is the gradient in bias field, whilst $\omega_M = \gamma M_s$ and $\omega_H = \gamma H$. It has been shown in Fig. (3.4) that the bandgap is linearly dependent on h_0, thus we can interpolate $\Delta_\omega/h_0 \approx 27$ MHz per mT. Both the numerator and denominator of the exponent in Eq. (3.26) can be controlled independently, by varying the bias field gradient G, or the amplitude of its periodic modulation h_0. This is crucial for controlling the behaviour of spin-waves.

To study this relationship, simulations were performed with $G = 20, 40, 60$ T/m and for each value of G, with $h_0 = 1, 2, 3, 4, 5$ mT. In each simulation, spin-wave-packets are excited in each band by a spatially uniform pulse centred at 18 GHz with a full width at half maximum of 10 MHz. To isolate the effect of transmission or reflection at the band gaps, damping of magnetisation precession was not included in these simulations.

Fig. (3.10) shows the results of these simulations. A spin-wave packet, in the first band, approaches the bandgap separating it from the other bands. When $h_0 = 0$, there is no band gap and the packet continues undisturbed. As h_0 increases, there are no effects on either T_B or the spatial amplitude of BOs whilst the transmission coefficient decreases rapidly until there is no transmission, only BOs in the first band. Conversely, as G increases, the Bloch period, T_B and spatial amplitude of oscillation both decrease, while the transmission coefficient can be seen to increase. It should be noted that the transmitted fraction of the wavepacket does

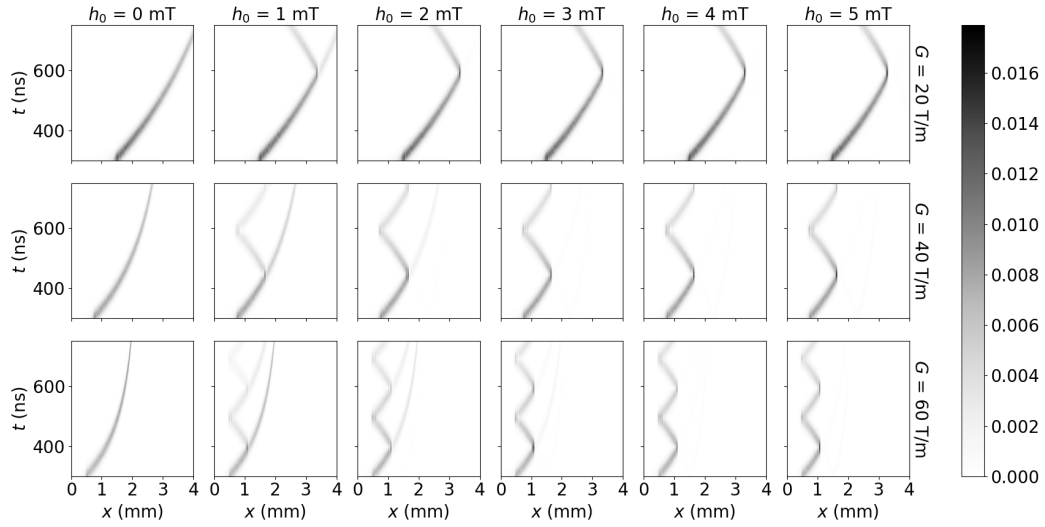

Fig. 3.10 Grid of position, time plots showing the deflection angle of magnetisation in a linear grey-scale colour map. Columns share the same amplitude of periodic modulating field h_0 (mT), whilst rows share the same gradient of bias field G (T/m).

not appear to be reflected at the next bandgap. This is likely since the first bandgap is much wider than any of the others. Therefore, by Eq. (3.26), transmission between higher-order bands is much more likely, giving rise to Bloch Zener Oscillations where a wave-packet crossing these bands is only reflected at the edge of the set of bands.

The transmission and reflection of spin-waves at the first bandgap were studied. The first band is the most strongly excited, making it the most pertinent band to study. Furthermore, the first bandgap is the widest, making it the easiest to control. Coefficients were extracted from the simulation data by the following method. Firstly, a subset of total data is extracted that contains the time and position that the spin-wave packet approaches the band edge. Secondly, the subset of data is split into two parts at the point in space that the bandgap manifests. The two parts are then integrated along the x axis to create a time series of integrated magnetic deflection in either band. The time series are normalised by their sum to yield the proportion of total magnetic deflection in either band as a time series. Finally, the time series are compared before and after the bandgap to determine the transition and reflection coefficients. The results are shown in Fig. (3.11).

The magnetic deflection angle is used instead of energy density as the simulation package used, MuMax3, does not compute energy density with sufficient precision to resolve the spin-wave-packets. Unfortunately, this substitution is a significant source of error as the relationship between deflection angle and energy density is neither local nor linear.

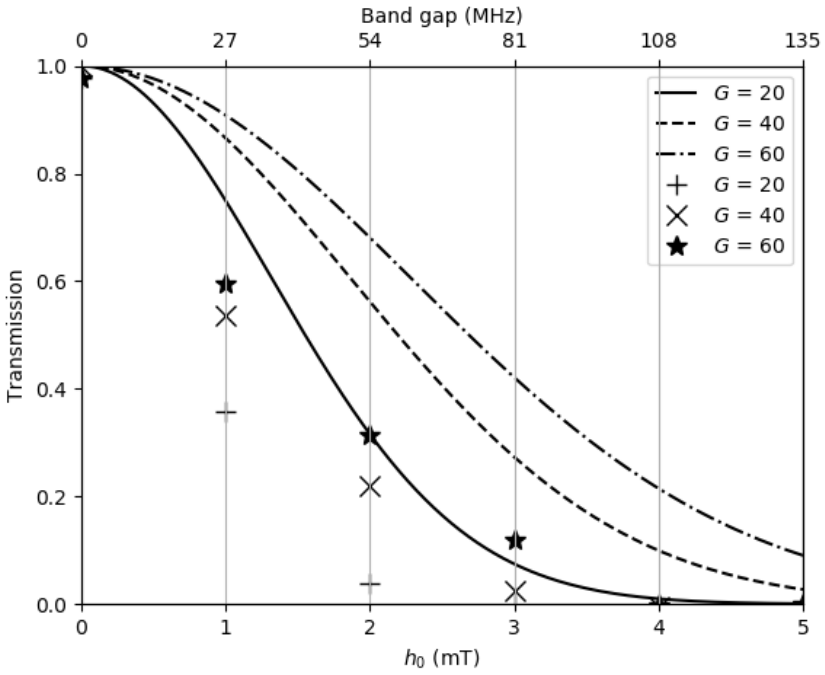

Fig. 3.11 Transmission coefficient of spin-waves at the 1^{st} band gap as a function of bias field modulation amplitude h_0 and bias field gradient G. Lines show theoretical predictions and markers show the results of simulations, each are labelled inset.

Fig. (3.11) shows the extracted transmission coefficient and that predicted by Eq. (3.26). A similar dependence on G and h_0 is observed for both simulation and theory, however, the predicted values significantly under-estimate the transmission probability. This discrepancy is likely due to the simulation data being based on magnetic deflection angle as a substitute for energy density.

In this section, we show that Zener tunnelling of spin-wave-packets can be promoted or suppressed by modifying the bias field gradient, G, and amplitude of periodic modulation h_0. It can be concluded that ZT occurs in this system. Moreover, ZT appears to be the rule,

rather than the exception for all bands gaps bar the first. Reflection at these boundaries is very minimal due to the band gaps being very narrow. This leads to the formation of BZOs that span the higher-order bands and have a period that is a multiple of the BO period. This shows that BZOs are responsible for the oscillations observed in Fig. (3.8) that exhibit a time period that is multiple of the Bloch period.

3.4.6 Low bias field regime

The theory presented in Sec. (3.2.3) is valid for the limit $H >> M_s$ and becomes increasingly inaccurate as the ratio of bias field approaches zero, $H \to 0$. This is a direct consequence of the dispersion relation of backward volume spin-waves, Eq. (3.13) which gives the width of the spin-wave manifold as,

$$\omega(k=0) - \omega(k \to \infty) = \gamma H \left(\sqrt{1 + \frac{M_s}{H}} - 1 \right), \tag{3.27}$$

which tends to a constant, γM_s when $M/H << 1$ and reduces down to 0 as $H \to 0$. In the latter case, Eq. (3.5) is expected to underestimate the Bloch frequency. To study this breakdown a simulation was performed in which the bias field starts at 0 at $x = 0$ and increases with a gradient $dH/dx = G = 100$ T/m,

$$\begin{aligned} \mathbf{H}(x,t) = &\left[Gx + A\sin\left(\frac{2\pi}{a}x\right) \right] \hat{x} \\ &+ \left[B\,\mathrm{sinc}(\omega_c(t-t_0)) \right] \hat{y}, \end{aligned} \tag{3.28}$$

where $G = 100$ T/m in order to include different regimes of H/M_s from 0 to above 2. The sinc profile in time evenly excites frequencies up to $\omega_c/2\pi = f_c = 20$ GHz. Whilst the pulse is uniform in space and so excites the band edges $k = n\pi/a$. The aim of this is to excite all spin-wave states, to resolve the entire Wannier ladder of spin-wave states in the frequency position domain for a range of H/M values.

Fig. (3.12) shows the results of the simulation that has been Fourier transformed into frequency and position space. Iso-wave-vector curves calculated using Eq. (3.13) are shown by dashed red lines for the $k = 0$, $k = \pi/a$ and $k \to \infty$ which show the upper and lower frequency bounds of the first band and other bands respectively. As the bias field approaches 0, the ladder states tamper to a point and intersect the frequency axis $x = 0$ at $\omega(0) = 0$.

The diagonal stripes are composed of many confined spin-wave states known as Wannier levels. These form a ladder, where the frequency step between levels is equal to the Bloch frequency of ω_B, which in this case is expected to be 8.6 MHz. Too small to be resolved in this figure.

The darker stripe is the ladder that corresponds to the 1st band, which is most strongly excited. The lighter stripe corresponds to a collection of higher-order bands, separated from one another by small bandgaps such that they appear as a single band. Indeed, spin-wave-packets have been shown to tunnel between these bands rather than be reflected, resulting in BZOs.

In the limit where $H > M_s$, Wannier ladders appear as stripes of constant thickness that have a gradient of $\gamma G/2\pi$, as shown by the straight dotted line. As H is reduced, the Wannier levels start to taper and bend downwards. The inset axes highlight the behaviour as $H \to 0$. Band gaps appear, splitting the higher-order bands from one another. Ultimately the bands collapse into a single point at $H = 0$. Their envelope closes in qualitative agreement with the spin-wave frequency limits shown by the dashed lines calculated by Eq. (3.13).

While the frequency gap between levels is too small to be observed, the Bloch frequency is proportional to the gradient of the frequency with respect to position. Therefore it is evident that ω_B is a constant for $H >> M_s$ and increases as $H \to 0$.

Fig. (3.13) is composed of two subsets of Fig. (3.12 which show the discrete ladder of Wannier states at two different points, with different ratios of H/M_s. In each case, the separation between frequency levels is equal to the Bloch frequency of f_B. Eq. (3.5) gives a

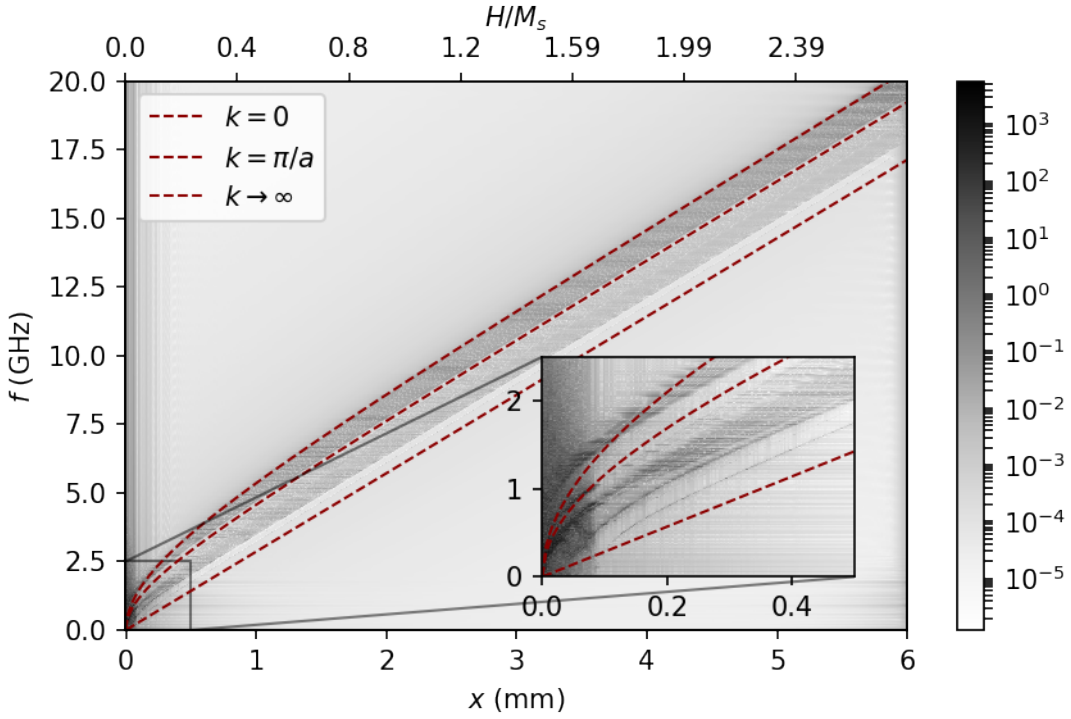

Fig. 3.12 Frequency and position plot showing the Wannier ladder of spin-wave states created by a bias field that starts at 0 at $x = 0$ and increase with $G = 100$ T/m. The ratio H/M_s is shown as a second x axis along the top of the figure. Dashed lines show iso-wavevector curves of Eq. (3.13), they correspond to the upper bound and lower bound of the dipolar spin-wave manifold, with the first bandgap in between. The inset axes highlight the region where $H/M_s \to 0$. In this limit, the Wannier ladders taper in width and bent in frequency towards zero, in a manner consistent with Eq. (3.13). As H increases,

.

predicted Bloch frequency of $f_B \approx 8.6$ MHz. In the top panel, where $H/M_s \approx 2$, $f_B \approx 8.7$ MHz, whilst in the bottom panel, where $H/M_s \approx 0.2$, $f_B \approx 12.5$ MHz for the first band and 10 MHz for the second band. This shows that different bands start to behave differently as $H/M_s \to 0$. In this regime, the approximation of the Bloch frequency as $f_B = a\gamma G$ breaks down due to the dependence of the acceleration term on the wave-vector.

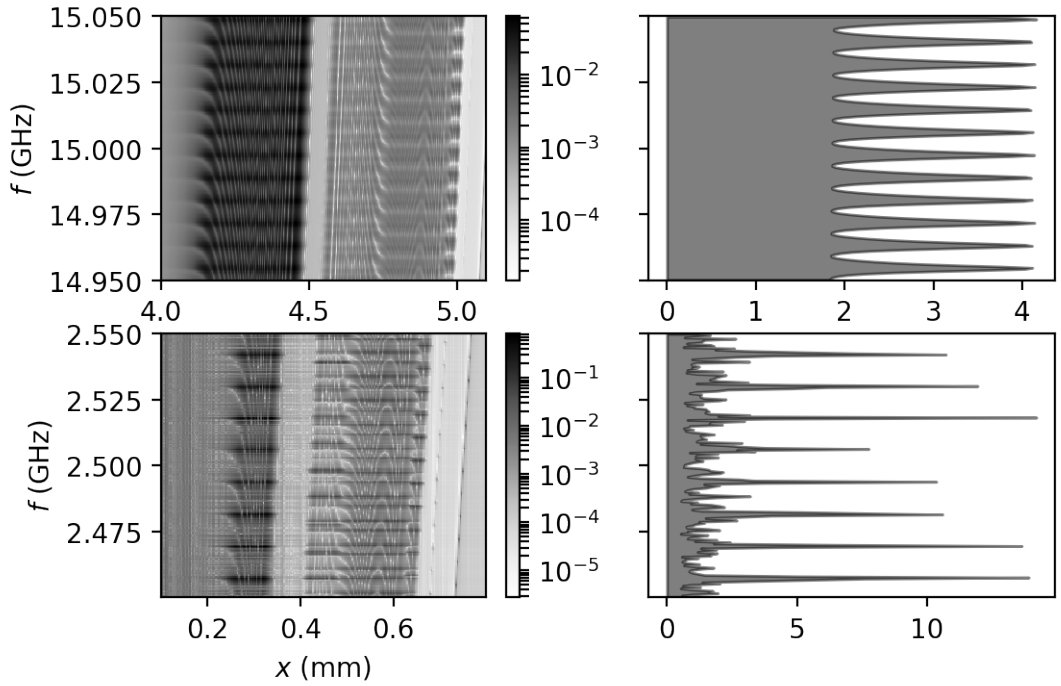

Fig. 3.13 Left panels. Subsets of Fig. (3.12) showing the individual Wannier levels in position and frequency space. Right panels show their frequency spectrum, computer as the sum over position. The top panels show the Wannier levels at $f = 15.05 \pm 0.1$ GHz, where $H/M_s \approx 2$. The difference between levels is approximately, 8.7 MHz and consistent between bands. The bottom panels show the Wannier states at $f = 2.5 \pm 0.1$ GHz, where $H/M_s \approx 0.2$. The difference between levels is approximately, 12.5 MHz for the first band, reducing to 10 MHz for the second band.

3.5 M_s modulated YIG film

Periodic modulation of the magnetisation saturation can be used to open bandgaps in the spin-wave spectrum. It can be achieved by creating a two-component magnonic crystal or by using lasers to locally heat a periodic pattern where magnetisation saturation is reduced. The latter can be switched on and off and has the potential for reconfiguration. To study the effect that modulating M_s has on Bloch oscillations, simulations were performed for a magnetic film composed of alternating stripes of different magnetisation saturation.

The physical system is a magnetic film, 1μm in thickness and composed of two sublattices that have different magnetisation saturation values, with a period of 2.93 μm. The first

sublattice has a fixed value $M_s = 200kA/m$ and occupies 7 out of 8 cells, stripes 2.563 μm in width. The second sublattice has a variable magnetisation saturation $0 \geq M_s' \geq M_s$ and occupies the remaining 1/8 cells in 0.365 μm width stripes. The same film as used in the previous section is recovered when $M_s' = M_s$.

The bias magnetic starts at 0.185 T and increases across the sample with a gradient of 40 T/m. It is not periodically modulated as this function is performed by modulation of the magnetisation saturation instead. A magnetic field pulse directed perpendicular to the film is used to excite spin-waves. The pulse is uniform in space and Gaussian in time, with a central frequency of 10 GHz $\pm$ 10 MHz. This excites spin-wave packets at the edge of each band which proceed to perform BOs due to the field gradient. For a fixed frequency, each band is spatially separated such that the bands do not overlap and according to Eq. (3.8) their trajectory will trace out a curve similar to the original band structure.

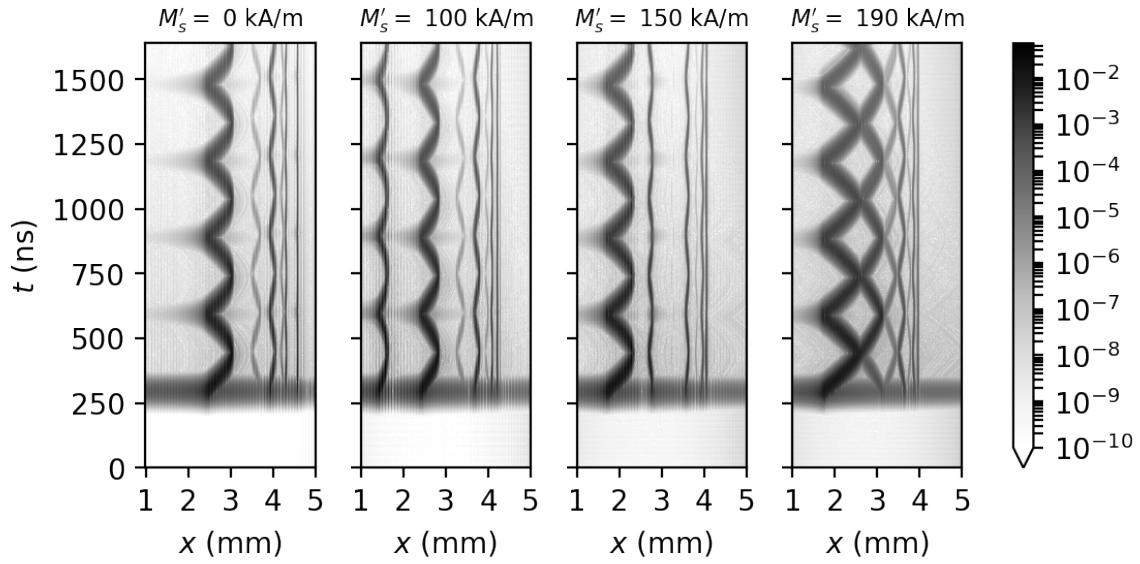

Fig. 3.14 Time position plot showing the trajectory of spin-wave packets excited by a spatially uniform pulse centred at 10 GHz $\pm$ 10 MHz. The bias field gradient is shown inset. The data shown is the deflection angle of magnetisation from the uniform state.

Fig. (3.14), shows the trajectory of spin-waves packets as they perform BOs. In all cases, the simulated oscillation period is $T_B = 288 \pm 25ns$ which agrees with the theoretical

prediction of 291 ns. This demonstrates that the period of oscillation is independent of the mode of patterning and is, therefore, the most predictable feature of BOs. It is, therefore, a good feature to measure experimentally to confirm the existence of spin-wave BOs. The shape of the BOs, in time and space, vary with the respect to the value of M_s'. As $M_s' \to M_s$, the periodic patterning is removed and the bandgaps close. This is most clearly seen in the right-hand panel of Fig. (3.14), where the BO trajectories resemble the empty lattice approximation of the band structure.

3.6 Proposed experiment

Although we have been unable to perform an experimental investigation of the results presented here. We show that the period of spin-wave Bloch oscillations are predictable when the bias field is much greater than the saturation magnetisation. In this section, an experiment to measure spin-wave BOs is proposed.

A periodically modulated YIG film positioned between two magnetic poles, one a sharp point and the other a uniform slab. The two magnetic poles provide a constant flux density gradient, as the field diverges from the sharp pole to the slab-shaped pole. The nature of the periodic patterning is left to be decided by the experimentalist. We have simulated periodic modulation of the saturation magnetisation and bias field, there is no reason that other forms of periodic patterning cannot be used to obtain the desired effect. A coplanar waveguide (CPW) is positioned across the centre of the sample and connected to an arbitrary signal generator and a high-frequency oscilloscope. The CPW is used as a transducer for both exciting the spin-wave packets in the system and for recording the spin-waves which return.

By sending a broadband pulse which is tightly focused in space, spin-waves of all wave vectors would be excited. However, they will all have the same T_B and so return at the same time, as shown in Fig. (3.8). This should result in a spike in the recorded current signal which occurs every T_B.

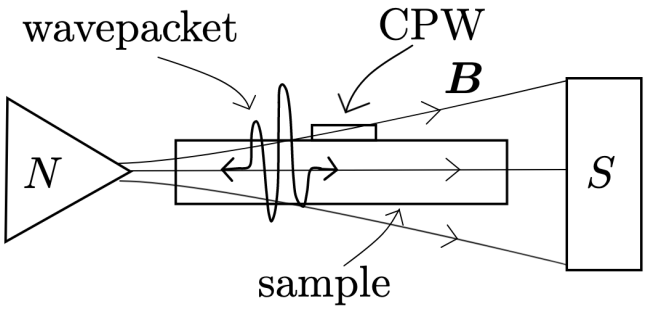

Fig. 3.15 Proposed experiment for the measurement of BO of spin-waves. Periodically modulated YIG film is positioned between two magnetic poles which produce a gradient in flux density which acts to accelerate spin-wave packets. Excitation and detection of spin-waves packets is achieved through the Orsted field of a coplanar waveguide (CPW).

In order to measure BOs, they must have a period long enough to be measured by the apparatus, yet shorter than the mean scattering time of spin-waves in YIG. An additional consideration is that the bias field gradient exerts a force on the magnetic film $F = M_s V G$, where V is the volume of the film. This is potentially a threat to the structure of the sample. Therefore, it is recommended that the lattice constant is sufficiently large enough that BOs can be measured at a bias field gradient that is sufficiently small not to damage the sample. In practice, the bias field gradient should be carefully increased from zero so that all possible values are measured in case of failure in high fields. A larger lattice period has the added advantage that it will be easier to fabricate. The details of these considerations depend upon the particulars of the apparatus and sample and we leave them to be addressed by those who may attempt such an experiment.

3.7 Conclusions

In conclusion, we have used micromagnetic simulations to demonstrate Bloch oscillations, Landau-Zenner tunnelling and Wannier-ladder spectrum for magneto-dipole spin-waves in the backwards-volume geometry under rather realistic experimental conditions. Scanning

Brillouin Light Scattering (BLS) microscopy and vector network analyzer (VNA) based spin-wave spectroscopy appear to be the best candidates to observe these phenomena in YIG-based systems experimentally. The requirement of a uniformly large gradient of the bias magnetic field appears to be the most stringent limitation. However, it could be overcome either through magnet engineering or using alternative ways to create the required graded magnonic index [9] These ideas could be extended to other magnonic geometries, systems and concepts. Augmenting the graded magnonic index with a time dependence [112, 113] appears a particularly interesting avenue for further research.

Our theory accurately predicts the time period of Bloch oscillations in the case where $H/M_s >> 1$. Furthermore, it provides an estimate of the wave packet trajectory which is good enough to inform micromagnetic simulations which can yield more accurate results necessary for the support of future experimental efforts.

Chapter 4

X-ray holography imaging of magnetic biskyrmions

4.1 Introduction

In this chapter, X-ray holography results are presented which suggest that recent reports of a novel magnetic texture, known as a Bi-Skyrmion, are possibly traditional bubble domains that were misinterpreted. Further analysis of Lorentz Transmission Electron Microscopy images confirms this hypothesis. Papers reporting the imaging of an exotic spin texture called biskyrmions have been published [114–117]. They are effectively two skyrmions with opposite chiralities bound together, fig. 4.1 and have been reported in $La_{1.37}Sr_{1.63}Mn_2O_7$ [15] and MnNiGa [114]. All of these reports rely on images of in-plane magnetic flux density taken using Lorentz Transmission Electron Microscopy (LTEM)[118].

LTEM is so-called because high energy electrons are directed onto a magnetic sample, where they are deflected as they pass through by the Lorentz force that arises from magnetic flux density in the magnet. Deflection by the Lorentz force makes it is sensitive only to the flux density component orthogonal to the beam and it cannot discriminate between elements. However, the spatial resolution is very high, $2nm$, whilst the time resolution is $40\mu s$,

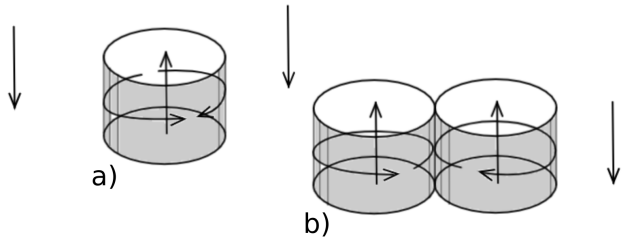

Fig. 4.1 Sketch of magnetisation in a film showing a) A bubble domain in the onion state. b) A biskyrmion. Each of which exists within a single contiguous domain of opposing magnetisation. Arrows indicate the orientation of magnetisation. These two structures formed into competing hypotheses during the investigation.

too slow to measure spin dynamics. Different modes of operation may be used to obtain contrast from this effect. The most common mode is the Fresnel mode, in which the electron beam is defocused. Domain walls appear bright for under-focus and dark for over-focus, however uniform flux density cannot be imaged. Images formed in this manner are difficult to interpret, especially when the magnetic texture is non-uniform. Micromagnetic simulations are often used to help interpret these images and synthetic LTEM images can be generated for a direct comparison. Furthermore, maps of the magnetic flux orthogonal to the beam can be reconstructed from several Fresnel mode images, taken at different degrees of defocus and using them to solve the transport of intensity equation (TIE)[119]. The in-plane flux density is co-linear with the in-plane magnetisation under the condition that magnetisation configuration has a flux closure structure in the plane. Therefore, structures such as domain walls, vortices and skyrmions, are readily identified from LTEM flux maps. However, if this condition is broken, in-plane magnetisation is no longer co-linear with in-plane magnetic flux, and it is more difficult to infer the magnetisation from the flux map.

We use X-ray holography to search for biskyrmions in MnNiGa. This technique directly measures the element-specific magnetisation component that is parallel to the X-ray beam direction. Thus it complements LTEM by being able to measure the out of plane component

of magnetisation at normal incidence [120]. Two lamellae of MnNiGa were extracted from a single crystal. One was measured in LTEM by our collaborators and the other we measured using X-ray holography with extended references and linear differential operator (HERALDO) [121], the details of which are described below.

Measurements were conducted on the SEXTANTS beamline at the X-ray light source Synchrotron SOLEIL [122]. Circularly polarised X-rays are generated from the relativistic electrons by a periodic structure of permanent magnets, known as undulators, and diffracted by our samples. The X-ray Circular Magnetic Dichroism (XMCD) effect yields a diffraction pattern dependent on the magnetic configuration and circular polarisation, giving sensitivity to magnetic moments parallel to the incident beam. Fourier transform holography is then used to reconstruct the magnetic configuration of the sample in real space.

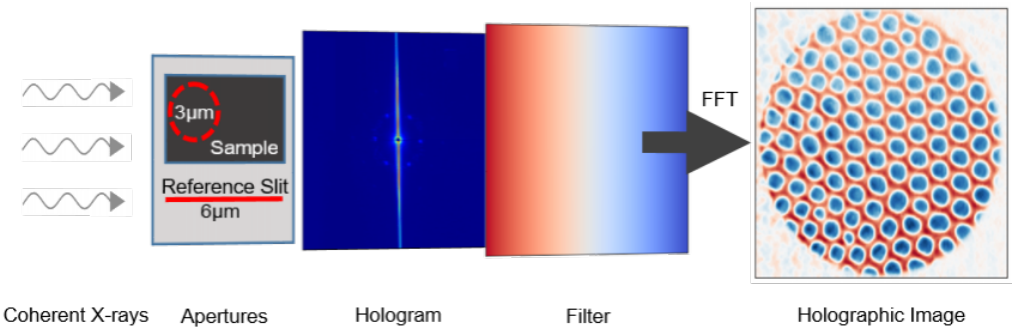

Fig. 4.2 The key elements of the HERALDO method. Circularly polarised, coherent x-rays diffract from the reference slit and sample aperture, forming an interference pattern known as a hologram that is imaged by a CCD. The difference between left and right circularly polarised X-rays carries the magnetic signal. The reference slit is deconvolved from the sample utilizing a differential filter. Finally, a Fourier transform is applied to represent the magnetic contrast in real space.

Experiments at SOLEIL were a joint effort between Exeter and Durham university staff and formed one part of a larger effort across the UK Skyrmion project [1]. The focus of this chapter is the X-ray holography experiments in which my contribution was to analyse experimental results and advise the experimental effort. To support this I also developed

[1] UK skyrmion project homepage, https://www.skyrmions.ac.uk/

holographic reconstruction routines that were used throughout this investigation and have been adopted by our collaborators. The code is a fresh implementation of the HERALDO algorithm, with the extension of automated reconstruction, a choice of deconvolution methods and visualisation tools, see appendix A.1. Sample preparation, complementary experiments using LTEM and micromagnetic simulations were performed by other members of the wider collaboration as assigned in the project work breakdown structure.

4.2 HERALDO: Holography with Extended References And Linear Differential Operator

4.2.1 SEXTANTS beamline

We worked on the Sextants beamline which was designed for elastic, inelastic and coherent scattering experiments with soft X-rays. In particular, we are interested in circularly polarised, soft X-rays in the region of 700 eV, to observe the XMCD effect.

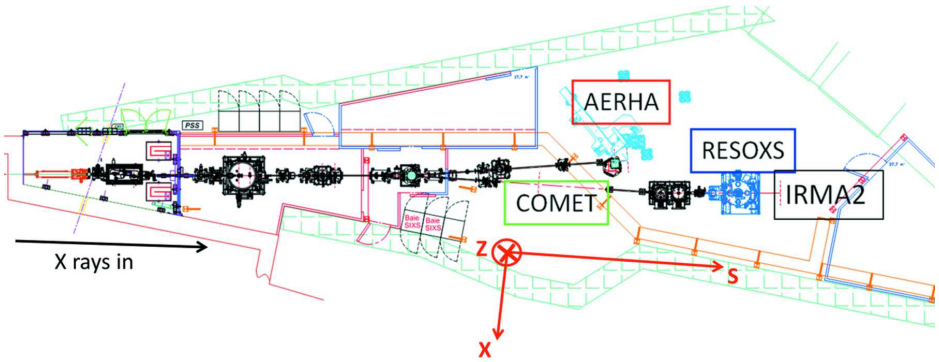

Fig. 4.3 Schematic of the SEXTANTS beamline,[122] showing the COMET detector in the centre.

X-rays are emitted by electrons in the storage ring when accelerated by the magnetic fields of the 2 x HU44 APPLE 2 undulators. These are periodic arrangements of magnets along the path of the electron beam which provide control over the polarisation of emitted

X-rays. They work by inducing lateral oscillations in electron beam through the Lorentz force, causing them to radiate X-rays. Polarisation is determined by the nature of the lateral oscillations; if they are confined to a single plane the X-rays are linearly polarised and if they are helical the X-rays are given a circular polarisation determined by the helicity. X-rays generated in this way are considered partially coherent, with a finite coherence length transverse and longitudinal to the direction of the beam.

A monochromator is used to filter the X-rays by their energy and increase the longitudinal coherence of the beam. The X-rays are diffracted from a grating at an angle determined by their wavelength and grating period. Only those diffracted at 5 degrees continue down the beamline. Fine control of wavelength can be achieved by rotating the diffraction grating to aim different wavelengths down the beamline, whilst coarse adjustments are made by swapping the grating for one with a different period. In addition, bandwidth can be traded for efficiency by changing the groove depth of the gratings. The depth of the grooves vary with position across the gratings, therefore a translation of the gratings changes the depth of groove upon which the X-rays are focused. This process improves the longitudinal coherence of the beam up to $12\mu m$.

Switching mirrors are used to direct the beam down the right-hand branch, to illuminate our holography experiments housed within COMET experimental chambers. The beam that illuminates the sample and mask has a transverse coherence of $25\mu m$ both horizontally and vertically, which is greater than the size of the sample mask which is approximately $15\mu mx15\mu m$. This is vital for Fourier imaging techniques, including HERALDO, as they depend on interference pattern between the sample and a reference. If light from these apertures is not coherent, then the interference pattern is scrambled and the real space image cannot be reconstructed.

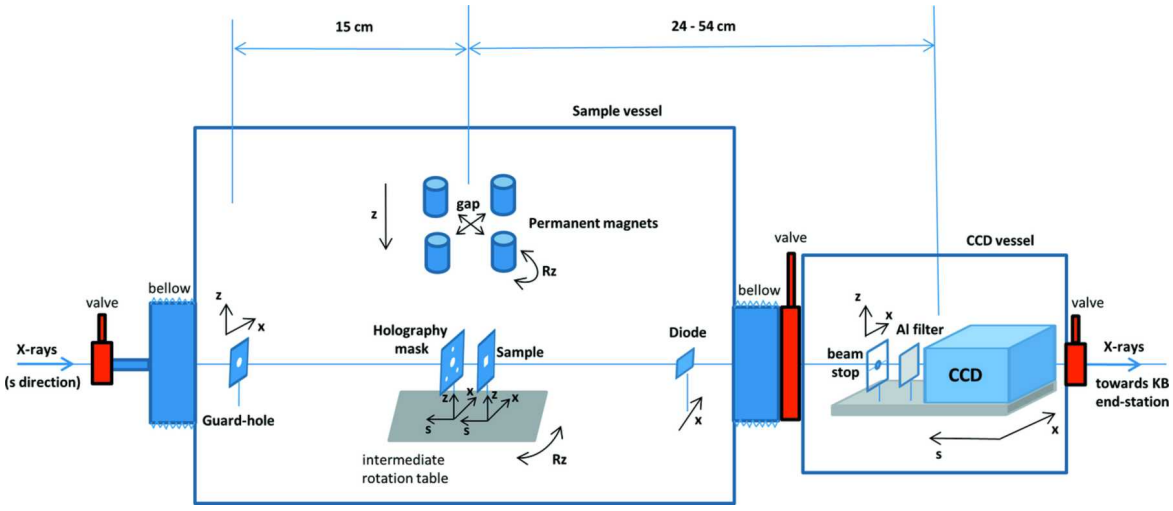

Fig. 4.4 Diagram of the COMET detector showing the key features of the two chambers. The sample vessel holds the sample on the rotating table, with a quadrupole magnet to control the bias field. The CCD vessel houses the CCD detector which is used to record the diffracted X-rays,[122].

4.2.2 COMET experimental chambers

COMET (COherent Magnetic scattering Experiments in Transmission) is an experimental chamber, shown in fig. 4.4, that is designed for elastic scattering of coherent X-rays to study the magnetisation of samples [122]. The key components and layout are shown in fig. 4.4.

X-rays enter the sample vessel, via a pinhole that skims the incoming beam, illuminating the chosen region of the sample. The sample and holography mask are mounted on a rotating table, enabling incident angles between 0 and 45 around a single axis. A quadrupole magnet provides control over the bias field by moving the position and orientation of permanent magnets. Details of the sample stage and quadrupole magnetic are shown in fig. 4.5.

A 1cm × 1cm Al-capped AXUV-100 diode is placed 15cm behind the sample in order to perform energy scans to find the absorption edges related to the magnetisation of the sample and aide with the alignment of the sample and beam. X-rays are scattered by the sample and detected by a 16 bit PI-MTE CCD camera from Princeton Instruments that measures 27.7mm x 27.7mm with 2048 x 2048 pixels. It is positioned 24cm behind the sample and 100nm thick Al filter prevents visible light from reaching the CCD. Finally a spherical beam-stop roughly

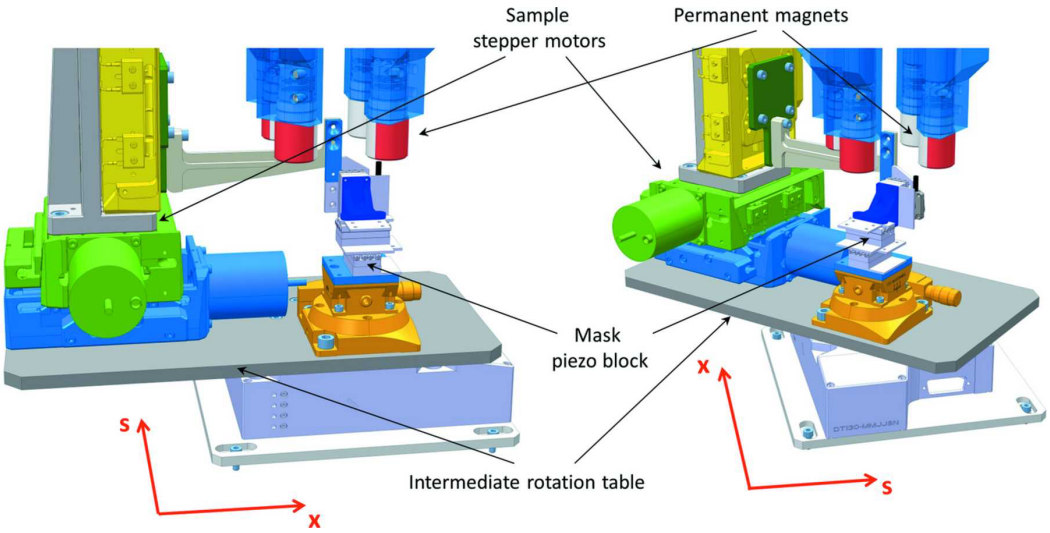

Fig. 4.5 Sample holder stage. Left and right show setup for normal and 45 degrees incidence respectively. The sample is mounted between the four permanent magnets,[122].

2um in radius is positioned 2cm in front of the CCD, protecting it from the non-diffracted X-rays.

4.2.3 Holography mask and sample holder

In typical X-ray holography experiments the holographic mask and sample are separate objects. In our case, they are combined in a single object. A circular aperture and a reference slit are milled into a gold plate. The sample is mounted on a Si_3N_4 membrane which is transparent for X-rays and positioned to cover the aperture but not the reference slit. The aperture is our window onto the sample.

One advantage of the slit, over traditional pinhole references, is that it allows the rotation of the sample to access different incident angles. This allows the in-plane component of magnetisation to be detected. Also, it provides a greater flux which gives a stronger interference pattern. Ideally, the reference and aperture have identical flux so that their interference patterns have the maximum contrast.

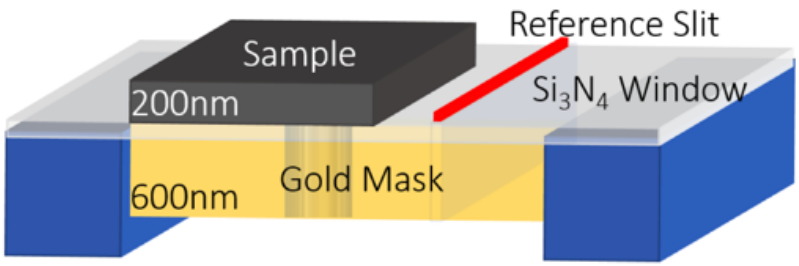

Fig. 4.6 Diagram of sample mounted onto the holographic mask. Sample is deposited on a Silicone Nitride membrane and positioned ontop of the gold holography mask's circular aperture. A reference slit enables holographic reconstruction.

4.2.4 XMCD: X-ray Magnetic Circular Dichroism

Circular Dichroism is the circular polarisation dependent absorption of light. It occurs in materials with broken inversion symmetry, or when time-reversal symmetry is broken by a magnetic field. X-ray circular magnetic Dichroism is an example of the latter and is distinguished from magneto-optical effects such as the Faraday effect by the use of X-rays instead of visible light. In both cases, the magnetic signal is obtained from the difference in transmission spectra between photons of opposite circular polarisation.

The mechanism of XMCD is the absorption of circularly polarised X-rays to induce an electric dipole transition of core p orbitals into d valence orbitals. Consider a ferromagnetic 3d transition metal, such as Fe. Its 3d orbital is responsible for its magnetic moment as it is partially filled, with a spin population of 5 up, 1 down. The 2p orbital is spin split into $j = 1/2$ and $j = 3/2$, where the spin-orbit interaction is coupled antiparallel and parallel respectively. Spin-orbit coupling correlates the circular polarisation of incident X-rays with the spin of the excited electrons, providing a source of spin polarised excited electrons that need to find a hole to occupy in the 3d valence orbitals. The transition $2p_{1/2} \rightarrow 3d$ is the L2 absorption edge, whilst $2p_{3/2} \rightarrow 3d$ is the L3 edge. These are electric dipole transitions between orbitals of odd, p and even, d centrosymmetry. As the parity of the electron must switch during a transition and given that the orbital component is inverted, the spin component must be conserved during the transition.

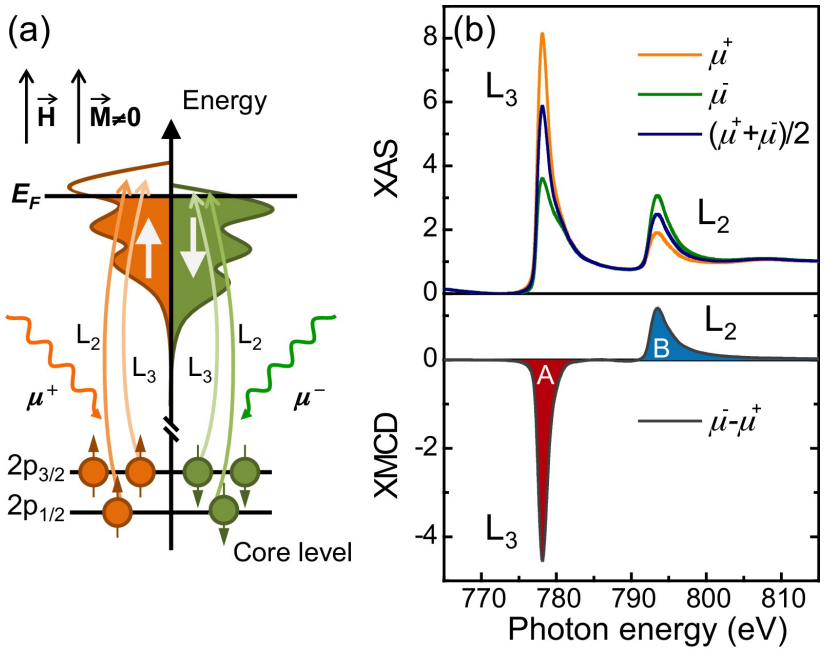

Fig. 4.7 a) Electric dipole transition of electrons from 2p orbitals to 3d by left and right circularly polarised X-ray photons μ. b) X-ray absorption spectra for different circular polarisations and corresponding XMCD obtained by the difference between left and right polarisation. The positive and negative XMCD signal, for L2 and L3 absorption edges respectively, is due to the opposite spin orbital coupling of the orbitals. Figure taken from [123]

As the 3d orbital has more holes with spin down than spin up, the absorption of circularly polarised X-rays depends on the component of the magnetic moment of the Fe atom co-linear with the X-ray path. Thus XMCD can be used to detect the element-specific magnetic moment co-linear to the incident X-ray beam. This is achieved by taking the difference between the diffraction patterns for the left and right-hand polarised X-rays. If the intensity of both images is equal, the subtraction cancels out the charge scattering, leaving only magnetic information. In this experiment, the L3 edge of Mn at 637.5 eV was used as it gave the greatest signal.

4.2.5 Reconstruction

The inverse scattering problem is the determination of the scatterer from its diffraction pattern. In the long-distance limit, the diffracted fields are simply the Fourier transform of the scatterer. In theory, an inverse Fourier transform of the complex diffracted fields yields the original scattering object. However, in practice detectors only measure the intensity of the diffracted fields, known as the diffraction pattern. With the loss of the phase information, different methods are required to reconstruct the scatterer from the absolute value of the diffraction pattern. Iterative phase retrieval algorithms are one approach.

Fourier transform holography is a way of achieving this in a single, deterministic step. It utilises a known reference source that has a well-characterised diffraction pattern. The diffracted X-rays from the reference interfere with those from the scatterer according to their relative phase. Thus the phase of the diffraction pattern is encoded into the interference pattern. This enables a deconvolution and inverse transform to reconstruct the original scatterer from the diffraction pattern.

4.2.6 Diffraction in the far field regime

When the plane of observation is far enough away from the aperture that the path distance from two most remote parts of the aperture to a point on the detector differ less than one wavelength then the diffraction pattern is said to be in the far-field regime,

$$\frac{W^2}{L\lambda} << 1, \tag{4.1}$$

where W is the width of the aperture, L is the distance to the detector and λ is the wavelength. In our experiment, the CCD detector is positioned 24cm from the holography mask and sample. The illuminating radiation has a wavelength on the order of 1.7nm and the aperture a diameter approximately 3μm. This gives $W^2/L\lambda \approx 0.021$, Therefore the diffraction pattern can be said to be in the far-field regime.

The Fraunhofer diffraction equation gives the diffraction pattern of a scatterer in the far-field regime. It states the complex scattered field is proportional to the Fourier transform of the complex field at the aperture.

$$\lim_{\frac{W^2}{L\lambda}<<1} F(x,y,z) \propto \iint_{dx'dy'} f(x',y') e^{-i\frac{2\pi}{\lambda z}(x'x+y'y)}\, dx'\, dy', \tag{4.2}$$

$$F \propto \mathscr{F}\{f\}, \tag{4.3}$$

where F is the complex diffracted field, f is the incident field and A is the area of the aperture. The primed coordinates are at the mask plane, while the unprimed coordinates are at the detector. We use the shorthand of the second equation where the capitalised letter is the Fourier transform of the lower case variable.

In our experiment, there are two apertures, the sample and reference, which are illuminated by the same coherent source. The total diffracted field F is the product of their respective Fourier transforms. The CCD measures the intensity of the diffracted X-rays,

which is given by the square of the modulus of the diffracted field,

$$F_{\pm} \propto (R_{\pm} \cdot S_{\pm})(S_{\pm} \cdot R_{\pm}), \tag{4.4}$$

where F_+ and F_- are the measured intensities of right and left-handed X-rays, R and S are the Fourier transform of the reference and sample respectively. Because there is only magnetic material in the sample aperture, $R_{\pm} = R$ and $S_- \neq S_+$.

4.2.7 Magnetic contrast

The magnetic diffraction pattern is given by the difference between the left and right-hand polarised X-rays diffraction patterns while the charge diffraction pattern is given by their sum.

$$M = F_+ - F_-, \tag{4.5}$$

$$C = F_- + F_+, \tag{4.6}$$

We are interested in the magnetic signal. In an ideal world there is no noise and the two images $F_{\pm}$ have equal intensities. In practice there is some noise but the intensity of the images can be normalised. Assuming the ideal case and expanding the terms out,

$$M = (R \cdot R + S_+ \cdot S_+ + R \cdot S_+ + S_+ \cdot R) \tag{4.7}$$

$$- (R \cdot R + S_- \cdot S_- + R \cdot S_- + S_- \cdot R), \tag{4.8}$$

where the $R \cdot R$ terms cancel out, everything else does not. We can simplify things by recognising $S_m = S_+ - S_-$, where S_m is the diffraction pattern of the magnetisation of the

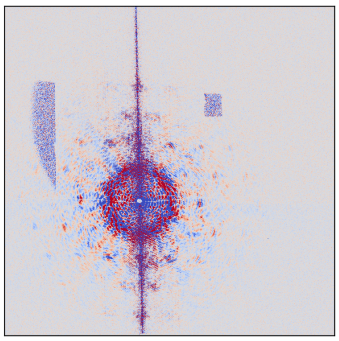

(a) $M = F_+ - F_-$

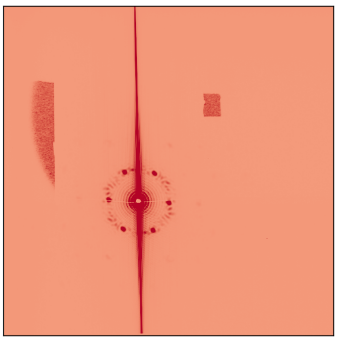

(b) $C = F_- + F_+$

Fig. 4.8 Sum and difference diffraction patterns. Left. The subtraction image containing mainly magnetic information via the XMCD effect. Right. The sum image containing mainly charge information. The blade shape in the upper left quadrant and the square in the upper left are both stray light artefacts.

sample,

$$M = S_m \cdot S_m + R \cdot S_m + S_m \cdot R. \tag{4.9}$$

4.2.8 Convolution theorem

The signal is still in reciprocal space and a Fourier transform is required to obtain the real space contrast. The convolution theorem states that the convolution of two functions, p and q, is equal to the inverse transform of the product of the Fourier transform of one function with the Fourier transform of the other,

$$p * q = \mathscr{F}^{-1}\{P \cdot Q\} \tag{4.10}$$

where P and Q are the fourier transforms of the functions p and q. Inverse Fourier transform of the intensity to the real space gives,

$$m = \underbrace{s_m * s_m}_{\text{Autocorrelation}} + \underbrace{r * s_m + s_m * r}_{\text{Crosscorrelations}}, \tag{4.11}$$

where the first term is the convolution of the sample with itself, this is also known as auto-correlation. Autocorrelations are always centred at the origin, every object is collocated with itself after all. The latter terms are the convolution of the reference and slit and slit with the reference, also known as cross-correlations. The displacement between the reference and the sample means that these images appear displaced from the origin in equal and opposite directions as convolutions do not commute. These terms show the convolution of the reference slit with the magnetic sample, therefore deconvolution is required to separate them and recover just the magnetic sample.

4.2.9 Deconvolution

Traditionally the aperture is a pinhole, so the reference is approximately a point. The convolution of a function with a point function simply yields the original function. In this special case, a direct inverse Fourier transform of the diffraction pattern yields the real space image. In general, deconvolution of the reference and sample aperture is necessary to recover the sample. If the diffraction pattern of the reference is known, then the measured diffraction pattern can be divided by the reference diffraction pattern R, to yield the Fourier transform of the sample itself. Only an inverse transform is now required to image of the sample,

$$f = \mathscr{F}^{-1}\left\{\frac{P}{Q}\right\} \tag{4.12}$$

however, in general, the diffraction pattern of the reference is not always known. In this case, information about the reference can be used to estimate it's Fourier transform and replicate key features.

In our experiments, a quick method is to divide the difference of the left and right-hand diffraction patterns with their sum before performing an inverse transform, i.e.

$$s_m \approx \mathscr{F}^{-1}\left\{\frac{M}{C}\right\}, \tag{4.13}$$

which is an approximation because the sum data, corresponding to the scattering by charges, is dominated by the diffraction pattern of the reference slits. Meanwhile, the difference data is dominated by the magnetic information of the sample. Due to the approximation, this method produces inferior results, as shown in fig. 4.9.

To produce the figures in this thesis and publications, a more accurate method is used. A gradient filter is applied to deconvolve the sample from the reference. The reference slit can be considered a line source. The convolution of an image with a line yields a smeared image. A gradient operation along its axis will yield two copies of the original image, separated by the length of the slit and with positive and negative contrast respectively.

$$r(x) = \begin{cases} 1, & \text{if } 0 < \mathrm{x} < \mathrm{L} \\ 0, & \text{elsewhere} \end{cases} \tag{4.14}$$

$$\nabla r(x) = \delta_{0,x} - \delta_{L,x} \tag{4.15}$$

Therefore application of a gradient filter to the inverse transformed data gives four images of the magnetic contrast. Two from each cross-correlation, separated by L,

$$m = \underbrace{\nabla(s_m * s_m)}_{\text{Autocorrelation}} + \underbrace{s_m * (\delta_{0,x} - \delta_{L,x}) + (\delta_{0,x} - \delta_{L,x}) * s_m}_{\text{Magnetic images}}, \tag{4.16}$$

where the first term is the autocorrelation of the sample with itself and the other terms are the magnetic images. In practice, this filter is applied directly to the diffraction images which are in the reciprocal space. Here the filter takes the form of an array with a linear gradient

orientated along the slit. Careful alignment of this filter is important for the quality of results. An inverse Fourier transform of the filtered data, with its origin at the centre of the diffraction pattern, yields the real space data. Once the reconstructed magnetic image is obtained, further

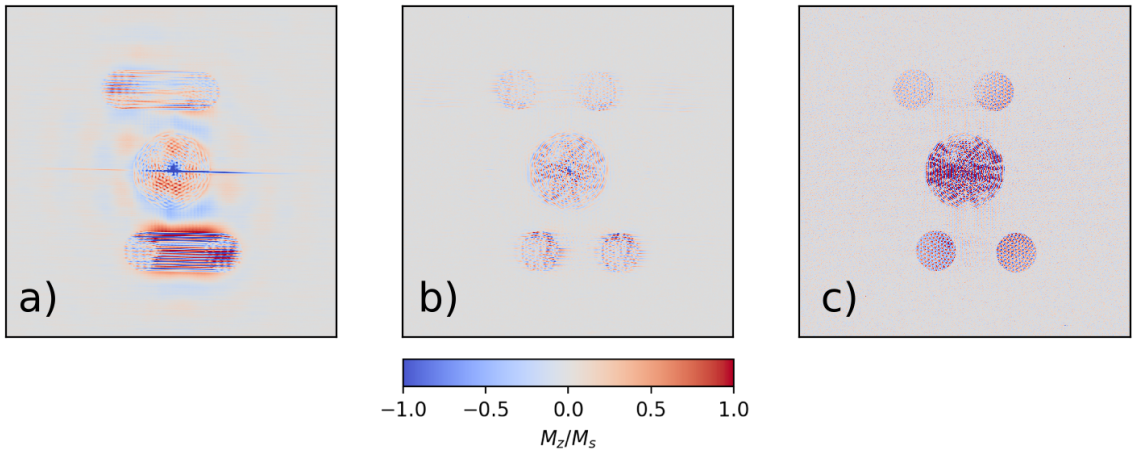

Fig. 4.9 Real space magnetic contrast, red and blue show $\pm M_z$ respectively. a) The convoluted image, b) the deconvoluted image using the division method 4.13 and c) shows the deconvoluted image using the gradient operator method 4.14. The Autocorrelation of the sample with itself is in the centre. The sample aperture is circular so the autocorrelation is a circle of double the radius. The four satellites are the recovered magnetic sample duplicated due to the cross correlations being deconvolved.

image processing is then applied to isolate the magnetic signal from the noise. This is an important part of the process because the signal to noise ratio is typically very low as the autocorrelations are naturally very intense. Furthermore, stray light, hot pixels and other unwanted artefacts can obscure the magnetic signal. These issues are not discussed here. A guide to the common issues and how to solve them is available in the user guide for hero.py attached in appendix A.1[2].

4.2.10 Resolution

A resolution of down to 20nm has been achieved in practice using this technique. Spatial resolution is predominantly determined by the reference slit as it gives the spatial resolution

[2]also on GitHub https://github.com/AngusLaurenson/HERALDO

of the phase on the detector. Temporal resolution is determined by the width of the X-ray packets in time, from 100 ps to 10ps, depending on the filling mode of the storage ring [122]. In this experiment, a resolution of 25nm is achieved.

4.2.11 Sample

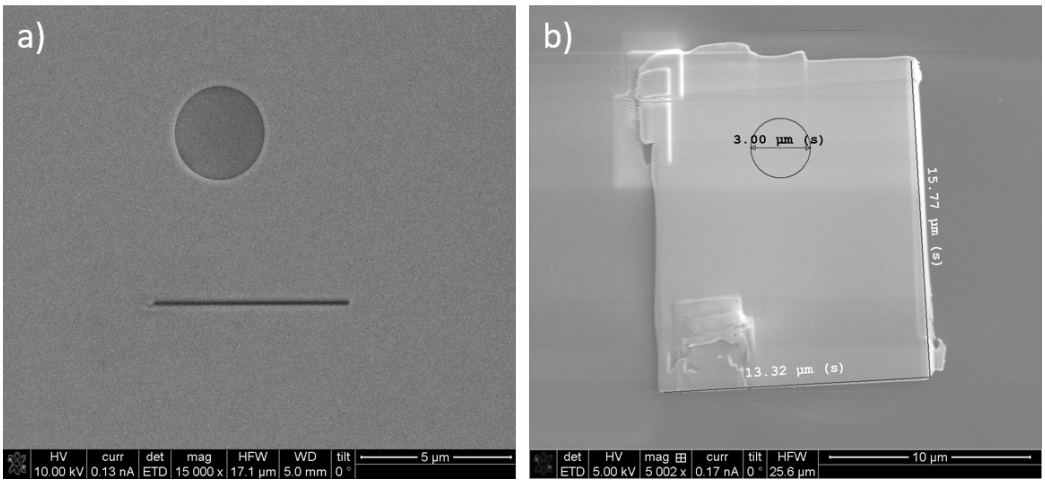

Fig. 4.10 Scanning electron microscope image of sample mask. a) the gold mask, circle is the aperture and the slit is the reference. b) Sample film deposited onto the gold mask. Annotated circle shows the position of the aperture.

The sample is a 200 nm thick, $10 \times 5\,\mu$m single crystal plate of MnNiGa that is orientated with its large surfaces normal to the magnetic easy axis, giving the plate a perpendicular magneto-crystalline anisotropy (PMA). It was cut from a polycrystal using gallium ion milling and lifted out with a micro-manipulator. Two identical platelets were prepared in the same manner, from the same single crystal. One for X-ray holography to gather new results and the other for LTEM, for direct comparison with published results [109].

MnNiGa has a hexagonal crystal structure with space group P63/mmc and lattice parameters a=b=4.15 Å and c=5.33 Å, Fig. (4.11). It has a Curie temperature of $T_c = 350$ K. Its hexagonal structure gives rise to an easy-axis magneto-crystalline anisotropy normal to the 001 plane. The film was cut such that the large surfaces are parallel to the 001 plane within 7 degrees. As the unit cell has inversion symmetry, asymmetric exchange interaction is

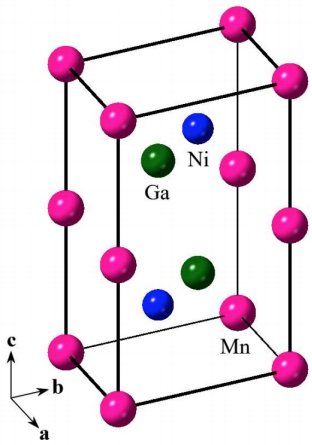

Fig. 4.11 The crystal structure of $Mn_{1/3}Ni_{1/3}Ga_{1/3}$. The vertical direction is the easy axis, normal to the 001 plane.

forbidden[43]. Therefore, the sample has no preference for the chirality of magnetic textures such as skyrmion like bubble domains that can form in it.

The material parameters of the sample are not known from direct measurement. Instead, they were inferred by fitting micromagnetic simulations to experimental data and informed by existing literature. The estimated magnetisation saturation, $\mu_0 M_s \approx 0.648T$ exchange stiffness $A_{ex} = 20$ pJm^{-1} [124].

4.3 Results

4.3.1 Formation of bubble domains from stripe domains

The formation of a sparse array of biskyrmions from stripe domains under the influence of a perpendicular bias field has been reported in MnNiGa using LTEM [114]. In this section, we attempt to replicate these results using HERALDO to measure the perpendicular component of the magnetisation.

The sample was orientated perpendicular to the incident X-ray beam and a field sweep from 0 to 310 mT was first carried out at room temperature, with the field applied normal to

the sample's surface, fig. (4.12). At the low field, stripe domains were observed. As the field was increased, those domains opposed to the field first narrowed and then fragmented at 250 mT to become a sparse array of single-cored bubble domains each with an average diameter of 120 nm separated by 650nm. This lattice of bubble domains was observed to be destroyed at 310 mT, being replaced with uniform magnetisation perpendicular to the surface.

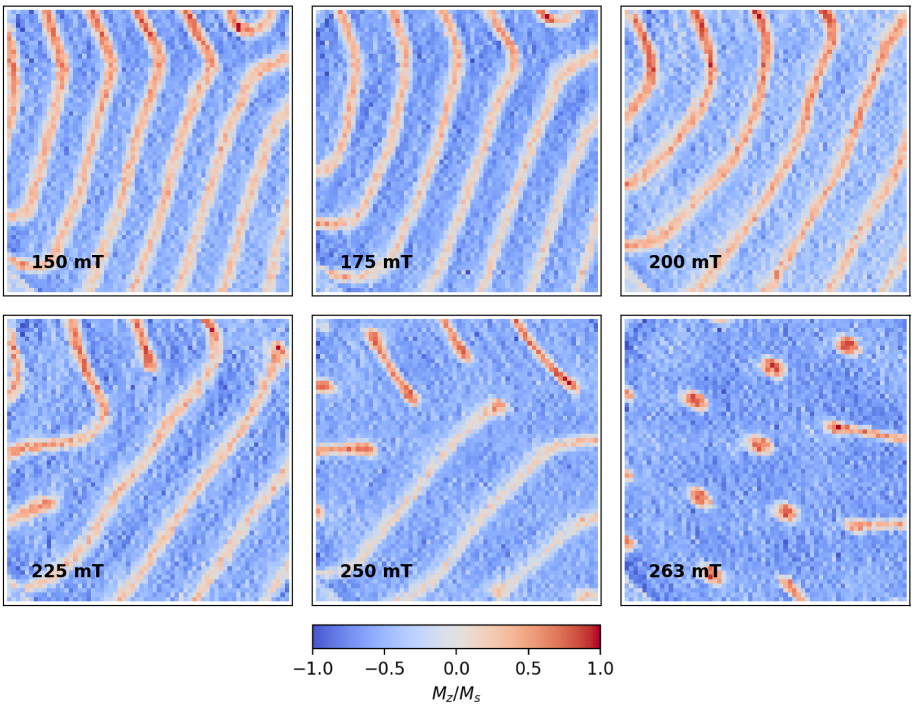

Fig. 4.12 Field sweep from 0 to 330 mT at room temperature. The colour scale red and blue indicates different values of the out of plane magnetisation component. The stripe domains move apart and finally break into a lattice of bubble domains. Stripes that have a weak out of plane signal are due to the movement of the stripe during the collection of the image.

Stripe domains are a typical ground state magnetisation for ferromagnetic films with perpendicular easy axis anisotropy when the bias field is weak. As the field increases, the stripe domains split and reduce down to a sparse array of bubble domains. Fig. (4.12) shows that the isolated domains formed have a single core structure and are therefore bubbles, not biskyrmions. Indeed, this method of stabilising bubbles has been well studied for its

application in magnetic bubble memory [125]. This suggests that such as genesis is indicative of magnetic bubble domains and not biskyrmions.

4.3.2 Field cooled formation of dense bubble lattice

Field cooling is a process whereby the bias field is held constant and the temperature is raised above the Curie temperature, erasing the magnetic order, before being reduced to a given temperature. The thermal disordering enables magnetic states to be accessed that cannot be obtained by continuous deformations of the magnetisation. Thus, field cooling is commonly used to induce the formation of skyrmion lattices in chiral magnets, where they appear as a metastable state near the curie temperature. A dense array of biskyrmions have also been reported to be created by this process [114]. We investigate the magnetic structures formed by field cooling using HERALDO.

The sample was heated above its Curie temperature (350 K) destroying the magnetic order and resetting the history of the magnetisation. It was then cooled back to room temperature under the influence of a perpendicular bias field. This process was repeated for bias fields between 0 and 175 mT, a subset is shown in fig. 4.13.

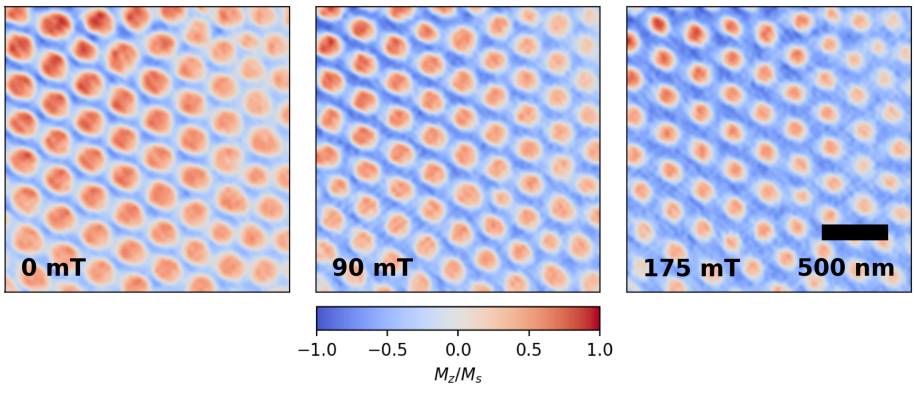

Fig. 4.13 Magnetisation configuration generated by field cooling from $350 \rightarrow 300K$. Red and blue show $\pm M_z$, the magnetisation component perpendicular to the film and bias field values are inset to each panel.

In all cases, a dense hexagonal array of circular, single-core perpendicular domains is stabilised. The magnetic state is created at high temperatures near the T_c and frozen in place by the cooling to form a highly resilient metastable state. As MnNiGa does not exhibit an asymmetric exchange interaction it would be surprising if these domains were magnetic skyrmions. Instead, they are most likely bubble domains. They form a hexagonal lattice that is stabilised by the magnetostatic interaction between the bubble domains.

4.3.3 Response of dense bubble lattice to external fields

A bubble domain lattice was generated by field cooling as in the previous section. It was then subject to perpendicular bias field swept from 0 mT to 400 mT. The bubble domains reduce in radius as the field increases, but their lattice constant does not change. At 400 mT the bubbles are reduced in size to roughly half their original radius but are not eliminated. This shows that a close-packed hexagonal array of bubble domains formed by field cooling has much greater stability than a sparse array of bubble domains created from stripe domains.

The perpendicular component of magnetisation is shown to be reduced between bubble domains along a specific axis of the bubble lattice. The magnetisation is assumed to be constant in magnitude throughout the sample. Therefore, there is a significant in-plane magnetic moment in between bubble domains along this axis.

Fig. (4.15) shows interpolated line scans of the M_z signal taken from centre to centre between bubble domains. It is shown that magnetisation does not fully reverse between bubbles along one direction, indicating an in-plane component of magnetisation. This indicates that the bubbles are of the onion configuration, (type 2). They appear to be arranged, head to toe, into chains that lie parallel to one another. This arrangement minimises the dipolar energy by compensating the magneto-static charges that are by the converging and diverging magnetisation in the domain walls of these type 2 bubble domains. Micromagnetic

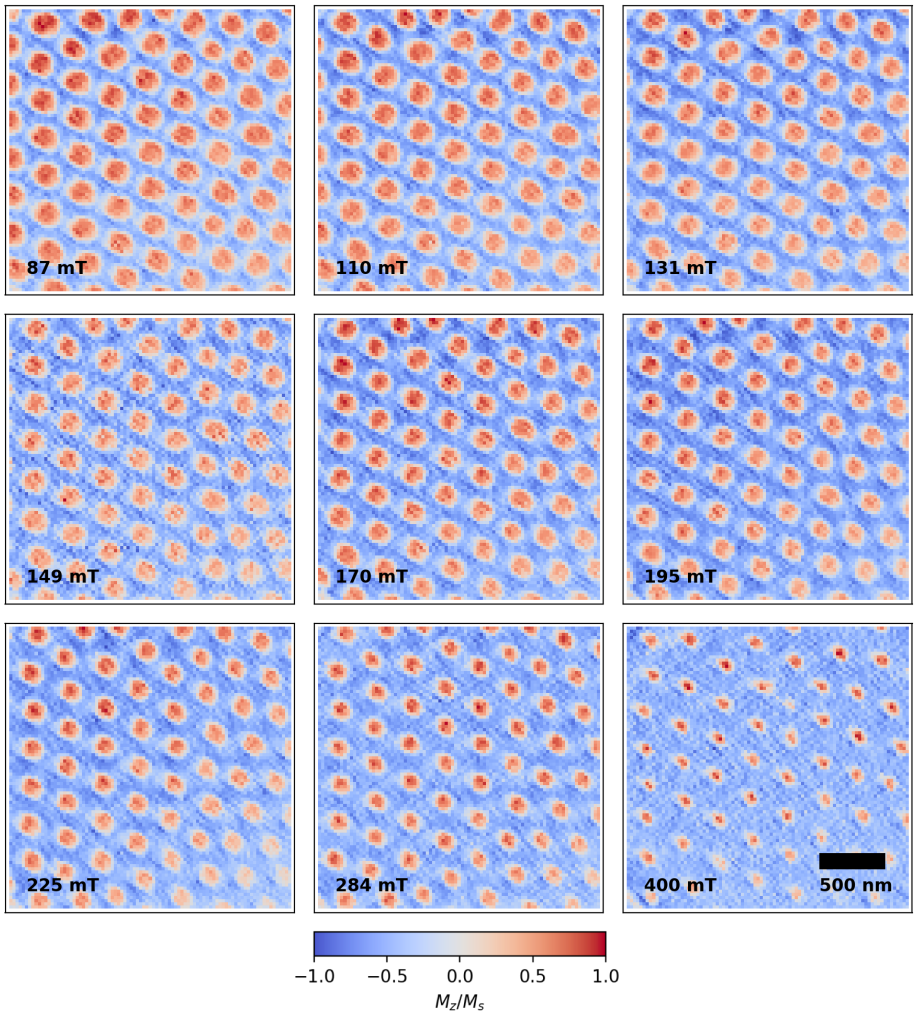

Fig. 4.14 Magnetisation configuration generated by field cooling from 350 → 300 K at 35 mT, then subject to a perpendicular bias field. Red and blue show $\pm M_z$, the magnetisation component perpendicular to the film and bias field values are inset to each panel.

simulations show that such arrangements do arise and help to explain the reduced out of plane magnetisation between bubbles in one direction [124].

4.3.4 Discussion

HERALDO was used to directly image the magnetisation component of the Mn sublattice that is normal to the plane, whereas LTEM measures the in-plane magnetic flux and the magnetic configuration is inferred from that. Therefore, HERALDO images are less ambiguous than

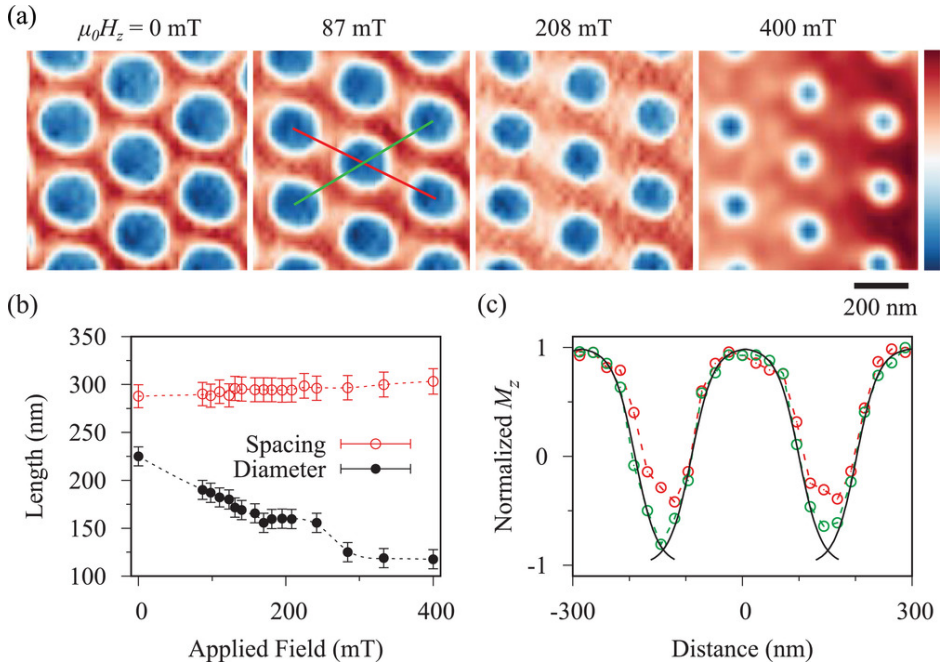

Fig. 4.15 a) Magnetisation normal to the surface for different bias fields labelled on top of the panels. Red, white and blue indicates the value magnetisation component normal to the sample at room temperature as $+M_s$ 0 and $-M_s$ respectively. b) The effect of increasing the applied field on the average centre-to-centre spacing of the bubbles and their diameter. c) Line-scans in the directions shown in (a) by the red and green lines. Solid black lines indicate hyperbolic tangent fits to the magnetic domain walls that yield a domain wall width of 47.5nm [124].

the LTEM images taken previously. Our images show a hexagonal lattice similar to those measured in LTEM. Only one out of plane magnetic core per lattice site was observed. At no point during the experiment were any double cores characteristic of biskyrmions observed. The 25nm spatial resolution of HERALDO is sufficient to discriminate the difference between a bubble domain and a biskyrmion, whose cores are separated by 100nm. This suggests that LTEM images of biskyrmions are bubble domains in the onion state or skyrmion like magnetic bubbles.

For traditional skyrmions and skyrmion like bubble domains, the in-plane magnetisation forms a closed-loop so there is no stray field. In this case, the in-plane field is directly proportional to the magnetisation. However, type 2 bubbles have a net magnetic moment

and the magnetic flux from these magnetic textures are not directly proportional to the magnetisation.

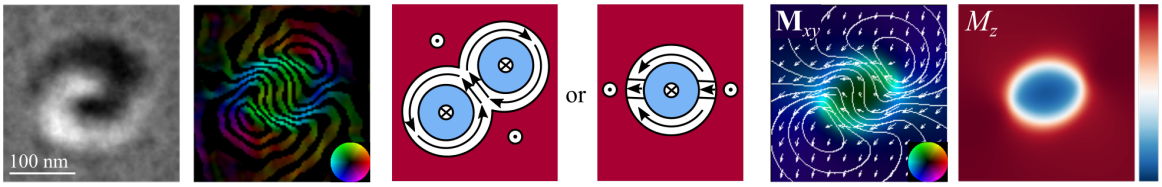

LTEM image | TIE B-field | Biskyrmion | Type-II bubble? | Type-II bubble: simulated magnetistaion (B-field lines overlaid in white)

Fig. 4.16 From left to right: LTEM image and corresponding reconstructed in-plane B field. Sketch of the magnetic biskyrmion, proposed as the source of this B field. Sketch of a bubble domain in the onion state, in-plane B field computed by micromagnetic simulation and magnetisation state from which the B field was computed. B fields are shown by contours which are coloured depending on the direction of the field. The sketch is coloured with Red showing perpendicular magnetisation points up out of the plane, Blue showing down into the plane and white with arrows showing in-plane magnetisation.

Fig. 4.16 was produced by our collaborators and it shows the competing hypotheses of a bubble domain or a biskyrmion. Micromagnetic simulations show that the in-plane magnetic flux density generated by a type 2 bubble domain is very similar to that measured in LTEM experiments of biskyrmions. This is because in both cases, the in-plane magnetic flux has a figure of eight circulation pattern, which similarly deflects the electrons. This insight supports our initial analysis that the biskrymion domains reported in the literature are likely to be bubble domains.

4.3.5 Conclusion

Images of biskyrmions in MnNiGa using Lorentz Transmission Electron Microscopy (LTEM) have been reported [114, 115]. We used HERALDO [121] experiments to directly measure the perpendicular component of magnetisation of a sample of MnNiGa in the biskyrmion lattice state [124]. However, instead of biskyrmions, a hexagonal lattice of type 2 bubble domains (onion state) was found, fig. 4.13. Analysis by our collaborators shows that the LTEM signal from type 2 bubble domains and biskyrmions are effectively indistinguishable

from one another, fig. 4.16. Moreover, there have been no mathematical models known developed that can explain the stability of biskyrmions [124]. On the weight of this evidence, and evoking Occam's razor, we conclude that LTEM images purportedly showing biskyrmions are highly likely to show lattices of traditional bubble domains. This work is published in Advanced materials [124].

Chapter 5

Collective excitation of bubble domains in an antidot lattice

5.1 Introduction

Magnonic crystals[1] are periodically modulated magnetic media which exhibit bandgaps in the spin-wave spectrum [5, 6]. These bandgaps can be used to control the propagation of spin-waves [10]. The most primitive scheme is to etch grooves into an otherwise continuous film [64] but this has the disadvantage that it cannot be switched on or off. One promising line of research is to use periodic modulation of the magnetisation itself to open the bandgaps [72–75]. The configuration of magnetisation in a system plays an important role in the propagation of spin-waves. If several metastable states exist in the system, there exists the possibility to switch between them. By doing so, the dynamic properties of the magnonic crystal are also changed [14]. Dynamic control of spin-wave propagation is important for the development of spin-wave switches and other devices of great utility in spin-wave logic circuits [126]. Bubble domains[2] are one candidate. They are cylindrical domains and their

[1] See section 2.5.1
[2] See section 2.6

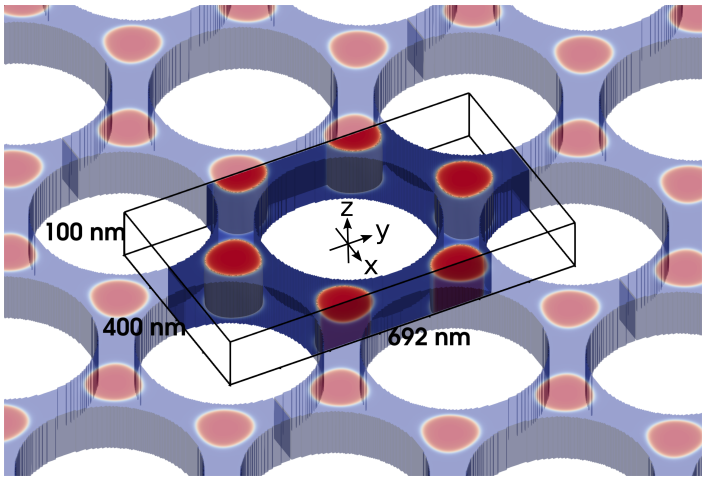

Fig. 5.1 The honeycomb array of magnetic bubble domains confined within a film with a hexagonal array of antidots. The highlighted cuboid is the unit cell used in simulations. It contains two of the diamond-shaped primitive cells of the bubble domain lattice due to the cuboid mesh. Red and blue indicate positive and negative values of the out-of-plane component of the magnetisation. The bubble domains are shown in red. They are confined to the node regions of the magnetic film and surrounded by a majority domain of opposite magnetisation, which is shown in blue.

stability and mobility enable them to store and carry information [4]. The recently discovered magnetic skyrmion is of particular interest [12]. It can be considered a special type of magnetic bubble domain which is defined by a topological winding number [127], which gives them greater stability against collapse [128], enabling them to be reduced in scale among other properties [129]. However, many authors distinguish skyrmions from bubble domains with the additional condition that they are stabilised by an asymmetric exchange interaction known as Dzyaloshinki-Moryia interaction (DMI) [43]. It is found in crystals that lack inversion symmetry and favours canted neighbouring spins rather than parallel neighbouring spins. This interaction means all the skyrmions in a crystal will have the same chirality. However, bubble domains with a skyrmion topology can still form in materials without any DMI interaction and these are known as skyrmion-bubbles. They have the same topological properties and similar internal modes but will not all necessarily have the same chirality. [130, 80].

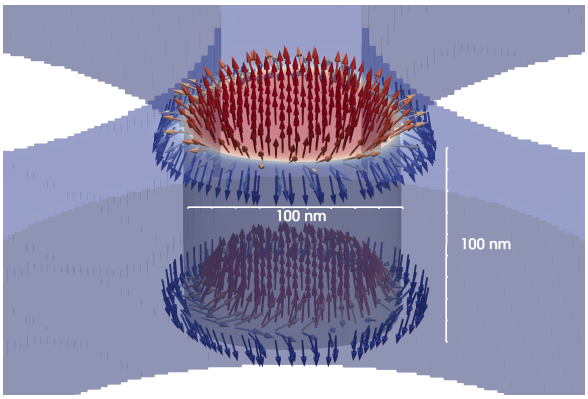

Fig. 5.2 The magnetisation configuration of a bubble domain confined within a node of the antidot lattice. Colour indicates the component of magnetisation perpendicular to the film while the direction of the arrows indicates the orientation of magnetisation the top and bottom surface of the bubble domain. The centre of the domain wall is shown by the grey cylinder which is defined as the contour where the magnetisation is entirely in the plane. In this case, it circulates around the domain wall.

In this context, the collective excitations of an array of skyrmion-bubble domains in a film patterned with a hexagonal array of antidots were studied using micromagnetic simulations. In this system, shown in fig. (5.1), the bubble domains are confined to node regions between antidots, forming a honeycomb array. The bubbles are stabilised by magneto-crystalline anisotropy orientated perpendicular to the film and by the shape anisotropy induced by the antidot lattice. The interaction between the dynamic modes of neighbouring bubble domains gives rise to a band structure. We use the width of the calculated bands emerging from different excited states of individual bubble domains as a measure of their magneto-dipole interaction strength. It is observed that only the breath modes give rise to magnonic bands of significant width and a group velocity large enough to enable energy to propagate through the system. Our findings are interpreted in terms of the spatial profiles of individual modes.

5.2 System

In Ref. [131], it was shown that a hexagonal array of magnetic antidots can support a variety of micromagnetic configurations, due to a complicated interplay between the exchange,

anisotropy and demagnetizing fields and depending on the value of the applied bias magnetic field. Furthermore, our subsequent micromagnetic simulations, which were performed using Mumax3 [32] and OOMMF [31] software, have shown an even greater range of metastable states exist when the parameters of the lattice and material are varied. Here, we focus on one case, in which an array of magnetic antidots supports a honeycomb array of magnetic bubble domains at zero bias magnetic field, fig. (5.1).

The antidot array is patterned from a 100 nm thick magnetic film. The antidots are 333 nm in diameter and form a hexagonal lattice with a lattice constant of 400 nm. We assumed the saturation magnetization of 600 kA / m, the exchange stiffness of 5.5pJ / m3, and the out-of-plane uniaxial magneto-crystalline anisotropy of 400 kJ / m, roughly corresponding to a cobalt-based magnetic superlattice. The assumed value of the Gilbert damping parameter was 0.001, i.e. artificially reduced to better resolve the magnonic band structure of the system.

5.3 Methods

A cubic mesh was used with cell dimensions 2.7 x 2.7 x 3.3 nm3, while the exchange length of the materials was 4 nm. Two dimensional (2D) periodic boundary conditions were used to approximate an infinite sample. The equilibrium magnetization configuration was established by relaxing the system under zero bias field from an initial state of saturated perpendicular magnetization with reversed magnetic cylinders at the node regions, to nucleate formation of bubble domains.

The magnetization dynamics were excited by a pulse of magnetic field oriented perpendicular to the film plane. Spatially, the pulse had a Gaussian profile (with a full width at half maximum of 140 nm) in the direction of propagation and was uniform in the two orthogonal directions. The temporal profile of the pulse was given by a sinc function with an amplitude of 10 mT and a cut-off frequency of 10 GHz. The results of real space - time-domain

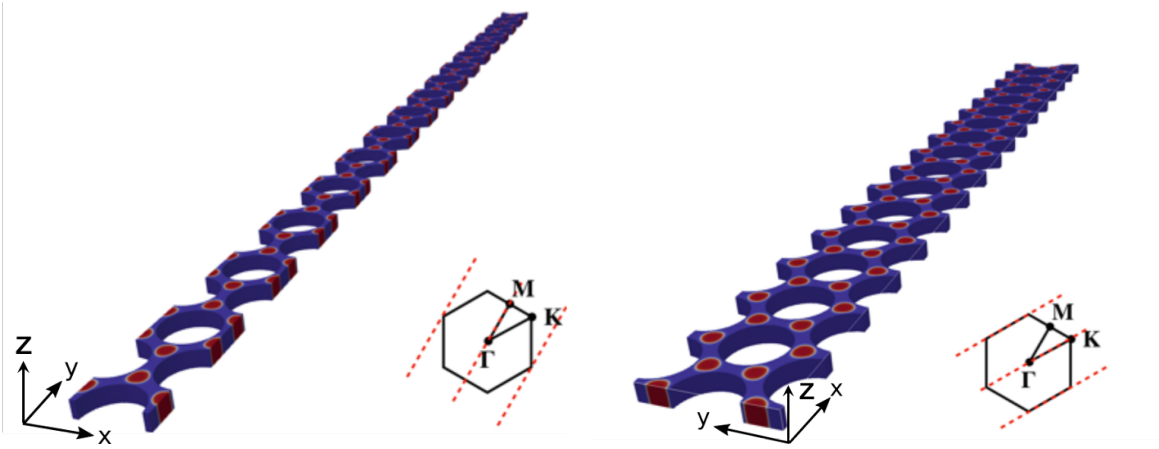

Fig. 5.3 Simulation volumes of 16 repeating units orientated along the principal symmetry axes left and right show Γ →M and Γ →K. Red and blue show positive and negative magnetisation component perpendicular to the plane. Inset figure shows the Weigner Ziets cell of the bubble domain lattice, the red dashed lines indicate the cuts accessed by the simulation.

simulations were converted, using Fourier transform, into reciprocal space-frequency domain, to recover the band structure and spatial mode profiles of observed magnetic excitations [36].

To obtain the full band structure, first waves travelling in all directions must be simulated before being transformed into reciprocal space. Unfortunately, the constraints of cell size, which must be smaller than the exchange length, simulation size, which must cover many Brillouin zones of the antidot lattice, combined with the limited available video card memory. Instead, the 2D periodic boundary conditions were applied to a stripe of 16 x 2 unit cells of the antidot lattice. Two unit cells are required across the short axis because the unit cell of the antidot lattice is diamond in shape while the mesh cells are cuboid. Uniform and antisymmetric modes are permitted across the width of the stripe. Spin waves are then sent down the long axis to approximate propagation in one direction through an infinite medium. We chose two important symmetry directions to investigate the dispersion at the M and K points in the reciprocal space. This produces two separate pairs of bands, one going through the centre of the Brillouin zone and the other along its edge, as shown in fig. (5.3).

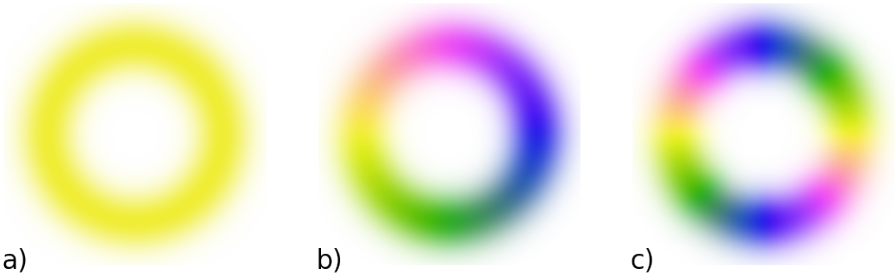

Fig. 5.4 Deformation modes of a bubble domain represented in the frequency domain. Panel a) Breathing mode, the phase is uniform around the domain wall, $m = 0$ b) gyration mode, phase varies by 2π around the domain wall, $m = 1$ c) elliptical mode, phase varies by 4π around the domain wall, $m = 2$. The phase is given by the cyclic colour map, while the intensity of the colour indicates the amplitude. The component of magnetisation perpendicular to the magnetic film is used as it is normal to the equilibrium orientation of spins in the domain wall.

The spatial character of the collective modes is shown for frequencies corresponding to the band centre and edge. The colour shows the phase, while the intensity shows the amplitude, of the out of plane component of magnetisation as it precesses. It is obtained by taking a Fourier transform of the data from the time to the frequency domain. Fig. (5.4a),b),c)) show the frequency domain representation of the breathing, gyration and elliptical modes of an individual bubble domain respectively.

5.4 Results

5.4.1 Band structure

Bubble domains interact with one another through their dipolar fields. In the static case, this provides a level of mutual stability, as demonstrated in chapter 3 for bubble domain lattices. In the dynamic case, oscillations in the bubble domain wall add a dynamic perturbation to their dipolar field. In a lattice of bubble domains, this dynamic dipolar interaction gives rise to the formation of a band structure, each band composed of the collective excitation of a single internal mode of the bubble domains. Four bands are expected from the simulations as

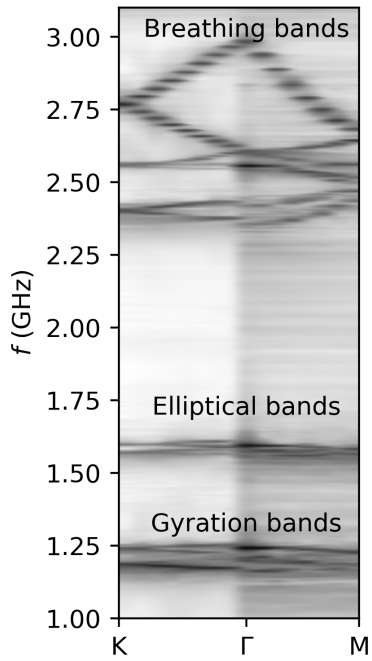

Fig. 5.5 Band structure of collective bubble domain oscillations along the $\Gamma \rightarrow K$, $\Gamma \rightarrow$M cuts.

the unit cell of the simulation contains to meta-atoms (bubble domains) in its basis, thus this method accesses two parallel cuts through reciprocal space, one through the centre and one along the edge as shown in fig. (5.3).

The band structure formed by the collective oscillation of bubble domains is shown in fig. (5.5). The frequency range is restricted to 3.1 GHz to clearly show the structure of the dispersive modes. Higher frequency bands appear flat and therefore do not correspond to propagating modes. Analysis of the spatial mode profiles shows that the widest bands arise from the collective breathing modes, whilst the flatter, lower frequency bands correspond to the collective gyration and elliptical modes. The spatial profile of these modes is shown for waves propagating along the y axis and their characteristics are discussed below. The profiles of waves travelling along the x axis are included in the appendix (B). One commonality of the modes that are shown is that they are uniform across the film thickness.

5.4.2 Collective breathing mode

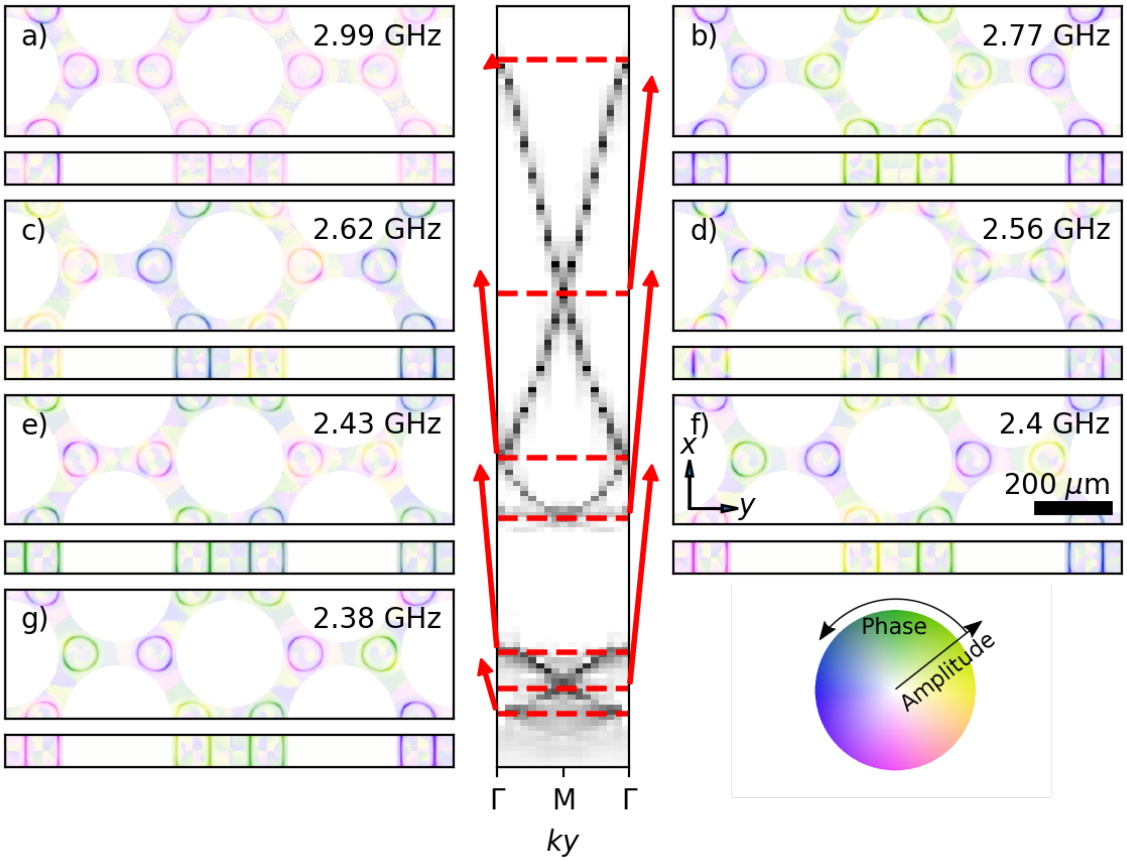

Fig. 5.6 The band structure of the collective breathing modes propagating along the y axis is shown in the centre, with the corresponding mode profiles on either side. For each frequency, a slice through the centre of the film is shown, along with a vertical slice along the length of the simulation showing the thickness mode profile. The colour shows the relative phase of precession and intensity the amplitude as shown in the inset colour wheel. A uniform phase around the domain wall of each bubble domains shows they are in the breathing mode. The difference in phase between neighbours shows the wavelength of the collective breathing modes.

Bubble domains in the breathing mode interact through the change in their dipolar moment, which is orientated perpendicular to the film and oscillates in amplitude with the periodic expansion and contraction of their radius. Consider two bubble domains located near enough to one another that their dipolar fields have a significant effect but not close enough that their domain walls are touching. Now the breathing mode of these domains split

into symmetric and anti-symmetric modes. The anti-symmetric mode has lower energy than the symmetric mode as it has a lower total magnetostatic energy. This gives the breathing mode in a linear chain of bubbles a negative group velocity, [67]. The strong dynamic dipolar interaction between breathing modes gives these bands the greatest width. The high frequency of the breathing mode is due, on one hand, to the restoring force associated with the exchange energy cost of an enlarged bubble and on the other, to the dipolar energy cost of a contracted bubble. Thus the frequency is greater than the gyration or elliptical modes.

Figure (5.6) shows the band structure and mode profiles of the collective breathing modes. The phase of magnetisation precession is shown by the colour, while the amplitude of is shown by the intensity, as described in fig. (5.4,a)). In all modes presented here, the phase is uniform through the thickness. Panels a)-d) show the modes where the phase is uniform across the stripe, whilst e)-g) show the modes where the bubbles on the edge of the stripe oscillate in anti-phase with those in the centre and therefore correspond to a cut along the edge of the Brillouin zone. These bands have the greatest width and group velocity which shows that the dipolar interaction between breathing modes is the strongest. Panels a) and c) show the symmetric and anti-symmetric mode at $|k| = 0$, where all unit cells oscillate in phase with one another. Panel b) shows the band edge where $k_y = \pi/a$, $k_x = 0$, the symmetric and anti-symmetric branches converge and appear to cross here. Panel d) shows the mode profile of an unexpected band which has non-uniform phase around the domain wall. The band structure of coupled dipoles in a honeycomb array is not always straightforward [132]. In this case, it is reminiscent of the flat band which is known to occur in Kagome lattices [133] and could be explained by considering collective mode structures more complex than a linear combination of isolated bubble domain modes. Panels e) and g) show the symmetric and anti-symmetric mode where the phase varies 2π across the stripe, corresponding to the BZ edge, $k_y = 0$, $k_x = \pi/2a$.

5.4.3 Collective gyration mode

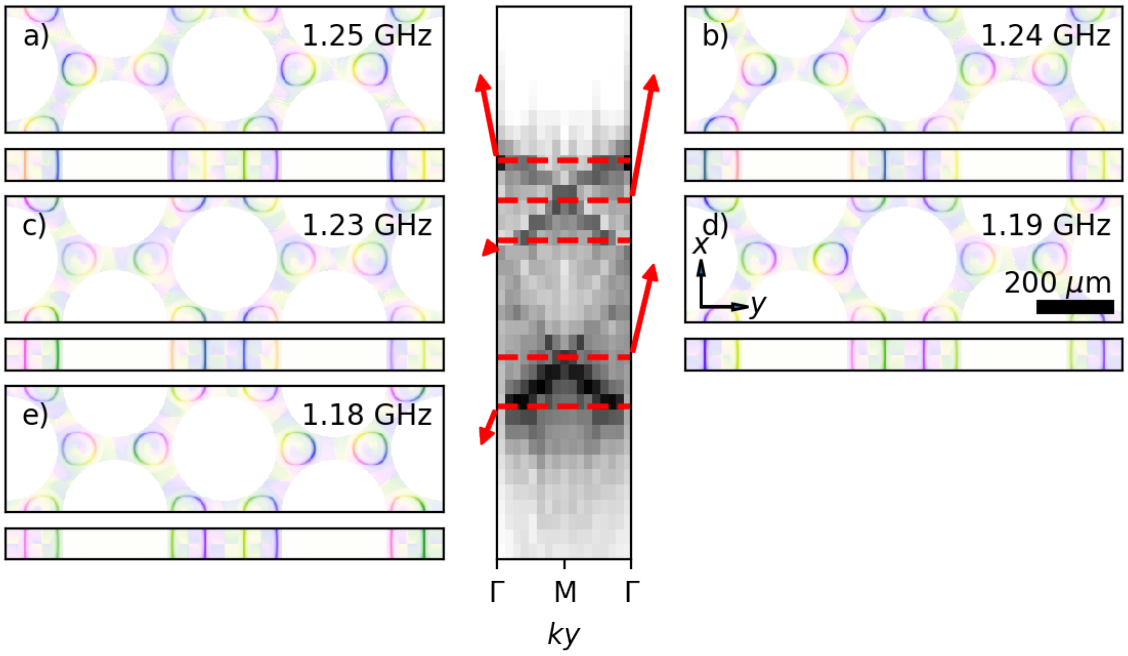

Fig. 5.7 The band structure of the collective gyration modes propagating along the y axis is shown in the centre, with the corresponding mode profiles on either side. the colour shows the relative phase of precession and intensity the amplitude. The phase rotates 2π around the domain wall of each bubble domains shows they are in the gyration mode.

In the gyration mode, the centre of mass of each bubble domain gyrates around its equilibrium position. When represented in frequency space, it corresponds to the phase of precession varying by 2π around the domain wall, as shown in fig. (5.4,b)). As the domain wall does not deform, there is no exchange energy associated with this mode, only the dipolar restoring forces. This gives the gyration bands the lowest frequency of any excitation in the crystal. The geometrical patterning provides a confining magnetostatic potential which prevents translational movement of the bubble domains and gives the collective breathing mode a finite frequency at $|k| = 0$. Furthermore, the dipolar moment of the domains do not change in amplitude, but they do oscillate in position with a gyration around the equilibrium position. This can be considered as an oscillation in the quadrupole moment of the bubble domain. The bandwidth is much thinner than for the breathing mode which shows the

interaction energy between neighbouring gyration modes is much smaller which is to be expected as the interaction energy of quadrupole moments drops off with distance more strongly than for dipole moments.

Fig. (5.7) shows the band structure and mode profiles of the collective gyration modes. In contrast to the breathing mode, the energy of the symmetric gyration mode is lower than the anti-symmetric mode as it preserves the distances between the bubble domains and therefore has no change in the interaction energy. There is however the confining magnetostatic potential due to the geometry, which gives this mode a finite frequency. Therefore the order of the modes in frequency is reversed with respect to the breathing mode. Panels a) and c) show the anti-symmetric and symmetric gyration modes for the case where the bubbles in the centre and edges of the stripe are in anti-phase. Panel b) shows the band edge where these two branches converge.

5.4.4 Collective elliptical mode

The elliptical mode is a wave in the domain wall with wavelength half the circumference. In frequency space, it appears as a ring with phase varying 4π around its circumference, as shown in fig. (5.4,c)). The bending of the domain wall costs exchange energy and this mode has a higher frequency than the gyration mode and in this system, lower than the breathing mode. There is very little demagnetising energy associate with this mode, its centre of mass does not move and the amplitude of the dipolar moment does not change either. Therefore the splitting of this mode is expected to be weak which is reflected in the bandwidth formed by the collective elliptical modes.

Fig. (5.8) shows the band structure and mode profiles of the collective elliptical modes. Once again the frequency order is reversed, with higher frequencies going to modes with neighbours oscillating in phase. Panels a)-c) show modes which are uniform in phase across the width of the stripe whilst d)-f) show the modes where the bubbles on the edge are in

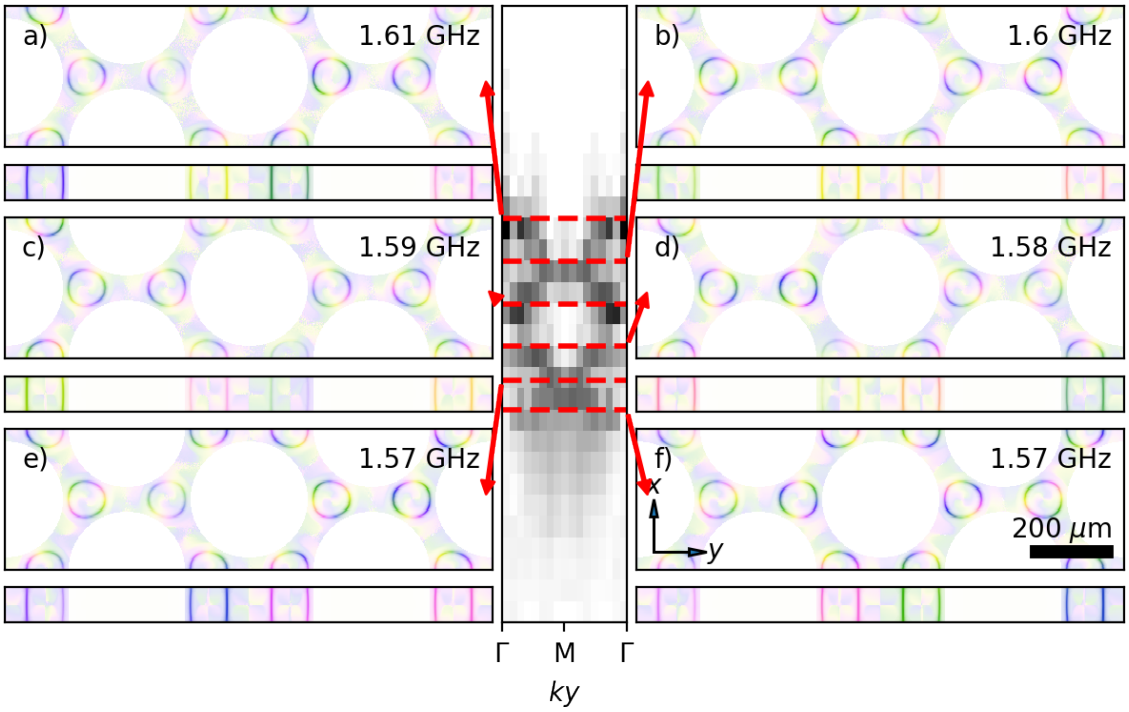

Fig. 5.8 The band structure of the collective elliptical modes propagating along the y axis is shown in the centre, with the corresponding mode profiles on either side. The colour shows the relative phase of precession and intensity the amplitude. The phase of precession rotates 4π around the domain wall of each bubble domain showing they are in the elliptical mode.

anti-phase with those in the centre. Panel a) has the highest frequency and all bubbles are oscillating in phase. Conversely, f) has the lowest frequency and all nearest neighbours are approximately in anti-phase. The small bandwidths mean that more wave vectors are measured as having the same frequency, therefore the mode profiles calculated are more uncertain than for more strongly dispersive modes such as the breathing mode.

5.5 Discussion

The band structure of collective modes of a honeycomb lattice of bubble domains, confined within a hexagonal antidot lattice, was simulated. The band-structure is populated by many flat, non-propagating bands. The prevalence of flat bands in the numerical dispersion indicates

that the coupling energy between excited bubble domains is small compared to the restoring potential energy of each bubble domain and that the system is in the weakly coupled regime.

We focus our discussion on the bands found between 0-3 GHz as they exhibit the greatest bandwidths and group velocities. Analysis of the spatial mode profiles in the frequency domain shows that these correspond to the collective breathing ($m = 0$), gyration ($m = 1$) and elliptical ($m = 2$) deformation modes. The collective breathing mode has the widest band and the highest group velocity. It also dominates the response of the magnonic crystal to external magnetic fields as it couples directly to uniform fields applied perpendicular to the film. These two features make it the most promising candidate for carrying information. Conversely, the other bands are both harder to excite and have many small bandwidths, group velocities and propagation distances. The bandwidth is observed to be inversely proportional to the mode number, m.

The width of a band is proportional to the interaction between energy between neighbouring domains. Given that the system is operating at frequencies below the spin-wave manifold and that the bubble domains are separated far beyond the exchange length $\lambda_{ex} \approx 4$ nm, neither spin-waves nor direct exchange interactions contribute to bubble domain coupling. Therefore, the principal coupling mechanism between domains is their dipolar interaction. As the bubble domain walls oscillate, transient magnetostatic charges are formed and destroyed at the surfaces, adding a dynamic perturbation to their stray magnetic field. These dynamic dipolar fields couple bubble domains and cause them to oscillate together, forming propagating bands. In the case of the breathing mode, the bubble domain radius expands and contracts uniformly, giving it an oscillating dipole moment. Gyration and elliptical modes do not have an oscillating dipolar moment but do have higher-order multipole moments which oscillate. As dipoles interact much more strongly with distance than higher-order multipole moment. The higher-order the bubble domain mode, the higher-order its dynamic multipole moment is and therefore the lower its bandwidth. This explains qualitatively the inverse relationship

between mode number and bandwidth. However, a more detailed analysis is required to make numerical predictions of the band structure.

5.6 Conclusion

In conclusion, we have used micromagnetic simulations to demonstrate that a hexagonal antidot lattice patterned from a film with a perpendicular magneto-crystalline anisotropy can support a honeycomb array of interacting magnetic bubble domains. The interdomain interaction has a magneto-dipole origin and gives rise to two dispersive collective magnonic bands, besides numerous flat bands. In principle, the dispersive bands are suitable for information transfer. Notably, the magnonic crystal presented here derives its properties from its micromagnetic configuration. Beyond this report, our simulations have revealed that a variety of other topologically complex micromagnetic configurations could be supported by similar antidot arrays with other magnetic and geometrical properties. Although systematic investigations of those systems and their dynamical properties is a subject of our ongoing research, our results show that non-uniform magnetic textures stabilized by patterned media radically change their response to the incident microwave magnetic field. Thus, as the magnetic samples naturally support multiple metastable states, such magnonic crystals and more generally metamaterials could offer an elegant way of achieving reconfigurable magnonic devices.

Chapter 6

Summary

Spin waves are the collective precession of magnetisation and have potential as information carriers in future spin wave devices. This requires control of their propagation which can be achieved by controlling their environment. The research in this thesis was aimed at both spin wave propagation in periodic media, and magnetic textures which could in the future find application in new magnonic crystals or other devices. In this context, the results presented in this thesis constitute a drop in the ocean.

In chapter 1, Bloch oscillations of spin waves are studied. They represent a novel means to control the propagation of spin waves. Micromagnetic simulations of a Yttrium Iron Garnet magnonic crystal, subject to a bias field that increases linearly across the system, show Bloch and Bloch-Zener oscillations of spin waves. These results are in good agreement with an analytical theory developed to treat the case of magnetostatic spin wave Bloch oscillations in the empty lattice approximation. The challenge now is to measure spin wave BOs in an experiment. This could be achieved using a YIG magnonic crystal, of which several have been studied, and placing between two poles of a magnet, one pointed and the other concave so as to produce a gradient in magnetic flux density. A coplanar waveguide could then be used to both excite and detect the breathing mode of spin wave BOs. Another interesting topic is the BO of dipole-exchange, backward volume spin waves as the dispersion of these

spin waves does not increase monotonically with wavevector but rather has a minimum at a non-zero value.

In chapter 4, X-ray holographic techniques were used to search for the recently reported and highly exotic magnetic texture known as biskyrmions, in a film of MnNiGa. With this technique we measured the perpendicular component of magnetisation which did not show the reported biskyrmion structure. Instead of a lattice of biskyrmions, our analysis revealed a lattice of traditional bubble domains. Complimentary experiments and further simulations by our collaborators confirmed this hypothesis and showed that the imaging technique used in other studies was unable to distinguish between the biksyrmion and bubble domain. Therefore we conclude that the existence of biskyrmions is doubtful. Routines for the reconstruction of real space magnetic contrast from the diffraction patterns was also developed. It is publicly available and has been adopted by other scientists.

Chapter 5 is a micromagnetic study of a magnonic crystal composed of bubble domains confined and stabilised within a hexagonal lattice of antidots. The dynamic modes of neighbouring bubble domains interact through their stray magnetic fields, forming a band structure of collective oscillations. However, only the collective breathing mode has a significant bandwidth and group velocity and an inverse relationship was observed between mode number of the bubble domain the width of the corresponding band structure. Given the low bandwidth and frequency of these modes in comparison to spin waves, they are not such promising candidates for carrying information. Further work in this area includes developing a theoretical model for the system, the investigation of other metastable, periodic magnetisation states and the transition between them.

In conclusion, a variety of numerical and experimental investigations are presented into new spin wave phenomena and domain structures. Micromagnetic simulations are used to demonstrate the Bloch oscillation of magnetostatic spin waves in a periodic magnetic film, representing a new way of controlling the spin wave propagation. Moreover an approximate

theory has been developed which matches the simulation results in the limit of high applied magnetic fields. This model could be used to develop a practical experiment to measure spin wave Bloch oscillations for the first time. An experimental investigation into the existence of a new magnetic domain known as a biskyrmion was conducted using elastic X-ray scattering holography. It was not found and a competing hypothesis was developed arguing that the biskyrmions imaging in previous works are more likely just traditional bubble domains. This demonstrates the strength of X-ray holography and the need to use complimentary imaging techniques. Finally the low frequency collective modes in a bubble domain lattice, confined withing a lattice of antidots, are simulated using micromagnetic simulations. It is found that only the collective breathing mode of the lattice has a significant group velocity and couples the strongest to applied magnetic field directed perpendicular to the plane. The multitude of equilibrium states possible in patterned films gives rise to the possibility of reconfigurable magnonic crystals for use in spin wave logic circuits. However the low bandwidth and frequency of collective bubble domain oscillation in comparison to spin waves means that they are not as good a candidate for carrying information.

Bibliography

[1] R. Sbiaa, H. Meng, and S. Piramanayagam, "Materials with perpendicular magnetic anisotropy for magnetic random access memory," *physica status solidi (RRL)–Rapid Research Letters*, vol. 5, no. 12, pp. 413–419, 2011.

[2] B. Terris and T. Thomson, "Nanofabricated and self-assembled magnetic structures as data storage media," *Journal of Physics D: Applied Physics*, vol. 38, no. 12, p. R199, 2005.

[3] M. N. Baibich, J. M. Broto, A. Fert, F. N. Van Dau, F. Petroff, P. Etienne, G. Creuzet, A. Friederich, and J. Chazelas, "Giant magnetoresistance of (001) Fe/(001) Cr magnetic superlattices," *Physical review letters*, vol. 61, no. 21, p. 2472, 1988.

[4] A. H. Bobeck, P. I. Bonyhard, and J. E. Geusic, "Magnetic bubbles—an emerging new memory technology," *Proceedings of the IEEE*, vol. 63, no. 8, pp. 1176–1195, 1975.

[5] V. V. Kruglyak, S. O. Demokritov, and D. Grundler, "Magnonics," *Journal of Physics D: Applied Physics*, vol. 43, no. 26, p. 264001, 2010.

[6] A. A. Serga, A. V. Chumak, and B. Hillebrands, "YIG magnonics," *Journal of Physics D: Applied Physics*, vol. 43, no. 26, p. 264002, 2010.

[7] M. Kostylev, A. Serga, T. Schneider, B. Leven, and B. Hillebrands, "Spin-wave logical gates," *Applied Physics Letters*, vol. 87, no. 15, p. 153501, 2005.

[8] A. Chumak, A. Serga, B. Hillebrands, and M. Kostylev, "Scattering of backward spin waves in a one-dimensional magnonic crystal," *Applied Physics Letters*, vol. 93, no. 2, p. 022508, 2008.

[9] C. S. Davies and V. Kruglyak, "Graded-index magnonics," *Low Temperature Physics*, vol. 41, no. 10, pp. 760–766, 2015.

[10] A. Chumak, V. Vasyuchka, A. Serga, and B. Hillebrands, "Magnon spintronics," *Nature Physics*, vol. 11, no. 6, pp. 453–461, 2015.

[11] U. Rößler, A. Bogdanov, and C. Pfleiderer, "Spontaneous skyrmion ground states in magnetic metals," *Nature*, vol. 442, no. 7104, pp. 797–801, 2006.

[12] A. Fert, N. Reyren, and V. Cros, "Magnetic skyrmions: advances in physics and potential applications," *Nature Reviews Materials*, vol. 2, no. 7, p. 17031, 2017.

[13] D. D. Stancil and A. Prabhakar, *Spin Waves*. Boston, MA: Springer US, 2009.

[14] M. Krawczyk and D. Grundler, "Review and prospects of magnonic crystals and devices with reprogrammable band structure," *Journal of physics: Condensed matter*, vol. 26, no. 12, p. 123202, 2014.

[15] X. Yu, Y. Tokunaga, Y. Kaneko, W. Zhang, K. Kimoto, Y. Matsui, Y. Taguchi, and Y. Tokura, "Biskyrmion states and their current-driven motion in a layered manganite," *Nature communications*, vol. 5, p. 3198, 2014.

[16] P. G. Morris, *Nuclear Magnetic Resonance Imaging in Medicine and Biology*. Oxford [Oxfordshire]; New York: Clarendon Press ; Oxford University Press, 1986.

[17] D. P. Arnold, "Review of microscale magnetic power generation," *IEEE Transactions on Magnetics*, vol. 43, no. 11, pp. 3940–3951, 2007.

[18] L. H. Lewis and F. Jiménez-Villacorta, "Perspectives on permanent magnetic materials for energy conversion and power generation," *Metallurgical and Materials Transactions A*, vol. 44, no. 1, pp. 2–20, 2013.

[19] J. Helszajn, *YIG Resonators and Filters*. New York: Wiley, 1985.

[20] H. C. Oersted, *Experiments on the Effect of a Current of Electricity on the Magnetic Needle*. C. Baldwin, 1820.

[21] D. J. Griffiths, *Introduction to Electrodynamics*. New Jersey: Prentice-Hall, 1999.

[22] P. Weiss and G. Foex, *Le magnétisme*. No. 71, A. Colin, 1926.

[23] R. P. Feynman, *Feynman Lectures on Computation*. Addison-Wesley, Jan. 1996.

[24] W. Heisenberg, "Multi-body problem and resonance in quantum mechanics," *Journal of Physics*, vol. 38, no. 6-7, pp. 411–426, 1926.

[25] P. A. M. Dirac, "On the theory of quantum mechanics," *Proceedings of the Royal Society of London. Series A, Containing Papers of a Mathematical and Physical Character*, vol. 112, no. 762, pp. 661–677, 1926.

[26] L. Landau and E. Lifshitz, "On the theory of the dispersion of magnetic permeability in ferromagnetic bodies," *Phys. Z. Sowjetunion*, vol. 8, no. 153, pp. 101–114, 1935.

[27] W. F. Brown Jr, "Theory of the approach to magnetic saturation," *Physical Review*, vol. 58, no. 8, p. 736, 1940.

[28] J. Eshbach and R. Damon, "Surface magnetostatic modes and surface spin waves," *Physical Review*, vol. 118, no. 5, p. 1208, 1960.

[29] A. Thiele, "Steady-state motion of magnetic domains," *Physical Review Letters*, vol. 30, no. 6, p. 230, 1973.

[30] J. Fidler and T. Schrefl, "Micromagnetic modelling-the current state of the art," *Journal of Physics D: Applied Physics*, vol. 33, no. 15, p. R135, 2000.

[31] M. Donahue, "OOMMF: Object Oriented MicroMagnetic Framework," 2016.

[32] A. Vansteenkiste, J. Leliaert, M. Dvornik, M. Helsen, F. Garcia-Sanchez, and B. Van Waeyenberge, "The design and verification of MuMax3," *AIP Advances*, vol. 4, no. 10, 2014.

[33] W. S. Ishak, "Magnetostatic wave technology: A review," *Proceedings of the IEEE*, vol. 76, no. 2, pp. 171–187, 1988.

[34] A. G. Gurevich and G. A. Melkov, *Magnetization, Oscillations and Waves*. New York: CRC Press Inc, 1996.

[35] P. Zeeman, "Xxxii. on the influence of magnetism on the nature of the light emitted by a substance," *The London, Edinburgh, and Dublin Philosophical Magazine and Journal of Science*, vol. 43, no. 262, pp. 226–239, 1897.

[36] M. Dvornik, Y. Au, and V. Kruglyak, "Micromagnetic simulations in magnonics," in *Magnonics*, pp. 101–115, Springer, 2013.

[37] E. Schlömann, "Demagnetizing fields in thin magnetic films due to surface roughness," *Journal of Applied Physics*, vol. 41, no. 4, pp. 1617–1622, 1970.

[38] D. Dove, "Demagnetizing fields in thin magnetic films," *Bell System Technical Journal*, vol. 46, no. 7, pp. 1527–1559, 1967.

[39] M. Pajda, J. Kudrnovskỳ, I. Turek, V. Drchal, and P. Bruno, "Ab initio calculations of exchange interactions, spin-wave stiffness constants, and curie temperatures of Fe, Co, and Ni," *Physical Review B*, vol. 64, no. 17, p. 174402, 2001.

[40] P. W. Anderson, "Antiferromagnetism. theory of superexchange interaction," *Physical Review*, vol. 79, no. 2, p. 350, 1950.

[41] J. Kanamori, "Superexchange interaction and symmetry properties of electron orbitals," *Journal of Physics and Chemistry of Solids*, vol. 10, no. 2-3, pp. 87–98, 1959.

[42] T. Kasuya, "A theory of metallic ferro-and antiferromagnetism on zener's model," *Progress of theoretical physics*, vol. 16, no. 1, pp. 45–57, 1956.

[43] I. Dzyaloshinskii, "Theory of helicoidal structures in antiferromagnets. I. nonmetals," *Sov. Phys. JETP*, vol. 19, no. 4, pp. 960–971, 1964.

[44] E. Girt, W. Huttema, O. Mryasov, E. Montoya, B. Kardasz, C. Eyrich, B. Heinrich, A. Y. Dobin, and O. Karis, "A method for measuring exchange stiffness in ferromagnetic films," *Journal of Applied Physics*, vol. 109, no. 7, p. 07B765, 2011.

[45] M. Wu, "Nonlinear spin waves in magnetic film feedback rings," in *Solid State Physics*, vol. 62, pp. 163–224, Elsevier, 2010.

[46] V. Baryakhtar, "The phenomenological theory of relaxation processes in magnets," in *Frontiers in Magnetism of Reduced Dimension Systems*, pp. 63–94, Springer, 1998.

[47] J. C. Slonczewski, "Current-driven excitation of magnetic multilayers," *Journal of Magnetism and Magnetic Materials*, vol. 159, no. 1-2, pp. L1–L7, 1996.

[48] T. L. Gilbert, "A phenomenological theory of damping in ferromagnetic materials," *IEEE Transactions on Magnetics*, vol. 40, no. 6, pp. 3443–3449, 2004.

[49] J. Griffiths, "Anomalous high-frequency resistance of ferromagnetic metals," *Nature*, vol. 158, no. 4019, p. 670, 1946.

[50] C. Kittel, "On the theory of ferromagnetic resonance absorption," *Physical Review*, vol. 73, no. 2, p. 155, 1948.

[51] F. Bloch, "Zur theorie des ferromagnetismus," *Zeitschrift für Physik*, vol. 61, no. 3-4, pp. 206–219, 1930.

[52] S. O. Demokritov, *Spin Wave Confinement*. Singapore; Singapore; Hackensack, NJ: Pan Stanford Pub. ; Distributed by World Scientific, 2009.

[53] R. Damon and J. Eshbach, "Magnetostatic modes of a ferromagnet slab," *Journal of Physics and Chemistry of Solids*, vol. 19, no. 3-4, pp. 308–320, 1961.

[54] K. Y. Guslienko and A. Slavin, "Spin-waves in cylindrical magnetic dot arrays with in-plane magnetization," *Journal of Applied Physics*, vol. 87, no. 9, pp. 6337–6339, 2000.

[55] L. Walker, "Magnetostatic modes in ferromagnetic resonance," *Physical Review*, vol. 105, no. 2, p. 390, 1957.

[56] B. Kalinikos and A. Slavin, "Theory of dipole-exchange spin wave spectrum for ferromagnetic films with mixed exchange boundary conditions," *Journal of Physics C: Solid State Physics*, vol. 19, no. 35, p. 7013, 1986.

[57] R. Damon and H. Van de Vaart, "Dispersion of spin waves and magnetoelastic waves in YIG," *Proceedings of the IEEE*, vol. 53, no. 4, pp. 348–354, 1965.

[58] T. Holstein and H. Primakoff, "Field dependence of the intrinsic domain magnetization of a ferromagnet," *Phys. Rev.*, vol. 58, pp. 1098–1113, Dec 1940.

[59] F. J. Dyson, "General theory of spin-wave interactions," *Phys. Rev.*, vol. 102, pp. 1217–1230, Jun 1956.

[60] A. J. Princep, R. A. Ewings, S. Ward, S. Tóth, C. Dubs, D. Prabhakaran, and A. T. Boothroyd, "The full magnon spectrum of yttrium iron garnet," *npj Quantum Materials*, vol. 2, no. 1, p. 63, 2017.

[61] A. Chumak, A. Serga, and B. Hillebrands, "Magnonic crystals for data processing," *Journal of Physics D: Applied Physics*, vol. 50, no. 24, p. 244001, 2017.

[62] S. A. Nikitov, D. V. Kalyabin, I. V. Lisenkov, A. Slavin, Y. N. Barabanenkov, S. A. Osokin, A. V. Sadovnikov, E. N. Beginin, M. A. Morozova, Y. A. Filimonov, *et al.*, "Magnonics: a new research area in spintronics and spin wave electronics," *Physics-Uspekhi*, vol. 58, no. 10, p. 1002, 2015.

[63] V. Kruglyak, P. S. Keatley, A. Neudert, R. Hicken, J. Childress, and J. Katine, "Imaging collective magnonic modes in 2d arrays of magnetic nanoelements," *Physical Review Letters*, vol. 104, no. 2, p. 027201, 2010.

[64] A. V. Chumak, A. A. Serga, B. Hillebrands, and M. P. Kostylev, "Scattering of backward spin waves in a one-dimensional magnonic crystal," *Applied Physics Letters*, vol. 93, no. 2, 2008.

[65] H. Ulrichs, B. Lenk, and M. Münzenberg, "Magnonic spin-wave modes in CoFeB antidot lattices," *Applied Physics Letters*, vol. 97, no. 9, p. 092506, 2010.

[66] A. Chumak, P. Pirro, A. Serga, M. Kostylev, R. Stamps, H. Schultheiss, K. Vogt, S. Hermsdoerfer, B. Laegel, P. Beck, *et al.*, "Spin-wave propagation in a microstructured magnonic crystal," *Applied Physics Letters*, vol. 95, no. 26, p. 262508, 2009.

[67] M. Krawczyk, S. Mamica, M. Mruczkiewicz, J. Klos, S. Tacchi, M. Madami, G. Gubbiotti, G. Duerr, and D. Grundler, "Magnonic band structures in two-dimensional bi-component magnonic crystals with in-plane magnetization," *Journal of Physics D: Applied Physics*, vol. 46, no. 49, p. 495003, 2013.

[68] A. A. Nikitin, A. B. Ustinov, A. A. Semenov, A. V. Chumak, A. A. Serga, V. I. Vasyuchka, E. Lähderanta, B. A. Kalinikos, and B. Hillebrands, "A spin-wave logic gate based on a width-modulated dynamic magnonic crystal," *Applied Physics Letters*, vol. 106, no. 10, p. 102405, 2015.

[69] A. Chumak, T. Neumann, A. Serga, B. Hillebrands, and M. Kostylev, "A current-controlled, dynamic magnonic crystal," *Journal of Physics D: Applied Physics*, vol. 42, no. 20, p. 205005, 2009.

[70] D. Grundler, "Reconfigurable magnonics heats up," *Nature Physics*, vol. 11, no. 6, pp. 438–441, 2015.

[71] M. Vogel, A. V. Chumak, E. H. Waller, T. Langner, V. I. Vasyuchka, B. Hillebrands, and G. von Freymann, "Optically reconfigurable magnetic materials," *Nature Physics*, vol. 11, no. 6, pp. 487–491, 2015.

[72] J. Topp, D. Heitmann, M. P. Kostylev, and D. Grundler, "Making a reconfigurable artificial crystal by ordering bistable magnetic nanowires," *Physical Review Letters*, vol. 104, no. 20, p. 207205, 2010.

[73] A. Y. Galkin, B. Ivanov, and C. Zaspel, "Collective modes for an array of magnetic dots in the vortex state," *Physical Review B*, vol. 74, no. 14, p. 144419, 2006.

[74] F. Montoncello and L. Giovannini, "Vortex mode dynamics and bandwidth tunability in a two-dimensional array of interacting magnetic disks," *Applied Physics Letters*, vol. 100, no. 18, p. 182406, 2012.

[75] F. Ma, Y. Zhou, H. Braun, and W. Lew, "Skyrmion-based dynamic magnonic crystal," *Nano letters*, vol. 15, no. 6, pp. 4029–4036, 2015.

[76] A. H. Bobeck and H. Scovil, "Magnetic bubbles," *Scientific American*, vol. 224, no. 6, pp. 78–91, 1971.

[77] A. Thiele, "The theory of cylindrical magnetic domains," *The Bell System Technical Journal*, vol. 48, no. 10, pp. 3287–3335, 1969.

[78] F. De Leeuw, R. Van Den Doel, and U. Enz, "Dynamic properties of magnetic domain walls and magnetic bubbles," *Reports on Progress in Physics*, vol. 43, no. 6, p. 689, 1980.

[79] W. Doring, "About the inertia of the walls between white districts," *Journal of Science A*, vol. 3, no. 7, pp. 373–379, 1948.

[80] I. Makhfudz, B. Krüger, and O. Tchernyshyov, "Inertia and chiral edge modes of a skyrmion magnetic bubble," *Physical Review Letters*, vol. 109, no. 21, p. 217201, 2012.

[81] V. P. Kravchuk, D. D. Sheka, U. K. Rößler, J. van den Brink, and Y. Gaididei, "Spin eigenmodes of magnetic skyrmions and the problem of the effective skyrmion mass," *Physical Review B*, vol. 97, no. 6, p. 064403, 2018.

[82] S.-Z. Lin, C. D. Batista, and A. Saxena, "Internal modes of a skyrmion in the ferromagnetic state of chiral magnets," *Physical Review B*, vol. 89, no. 2, p. 024415, 2014.

[83] V. L. Zhang, C. G. Hou, K. Di, H. S. Lim, S. C. Ng, S. D. Pollard, H. Yang, and M. H. Kuok, "Eigenmodes of néel skyrmions in ultrathin magnetic films," *AIP Advances*, vol. 7, no. 5, p. 055212, 2017.

[84] T. Shiino, K.-J. Kim, K.-S. Lee, and B.-G. Park, "Inertia-driven resonant excitation of a magnetic skyrmion," *Scientific reports*, vol. 7, no. 1, pp. 1–7, 2017.

[85] C. Schütte and M. Garst, "Magnon-skyrmion scattering in chiral magnets," *Physical Review B*, vol. 90, no. 9, p. 094423, 2014.

[86] J.-V. Kim, F. Garcia-Sanchez, J. Sampaio, C. Moreau-Luchaire, V. Cros, and A. Fert, "Breathing modes of confined skyrmions in ultrathin magnetic dots," *Physical Review B*, vol. 90, no. 6, p. 064410, 2014.

[87] M. Garst, J. Waizner, and D. Grundler, "Collective spin excitations of helices and magnetic skyrmions: Review and perspectives of magnonics in non-centrosymmetric magnets," *Journal of Physics D: Applied Physics*, vol. 50, no. 29, p. 293002, 2017.

[88] J. C. Butcher, "A history of runge-kutta methods," *Applied numerical mathematics*, vol. 20, no. 3, pp. 247–260, 1996.

[89] A. Jameson, W. Schmidt, and E. Turkel, "Numerical solution of the euler equations by finite volume methods using runge kutta time stepping schemes," in *14th fluid and plasma dynamics conference*, p. 1259, 1981.

[90] F. Bloch, "About the quantum mechanics of electrons in crystal lattices," *Journal of Physics*, vol. 52, no. 7-8, pp. 555–600, 1929.

[91] C. Zener, "A theory of the electrical breakdown of solid dielectrics," *Proceedings of the Royal Society of London. Series A, Containing Papers of a Mathematical and Physical Character*, vol. 145, no. 855, pp. 523–529, 1934.

[92] K. Leo, P. H. Bolivar, F. Brüggemann, R. Schwedler, and K. Köhler, "Observation of Bloch oscillations in a semiconductor superlattice," *Solid State Communications*, vol. 84, no. 10, pp. 943–946, 1992.

[93] T. Dekorsy, R. Ott, H. Kurz, and K. Köhler, "Bloch oscillations at room temperature," *Physical Review B*, vol. 51, no. 23, p. 17275, 1995.

[94] H. Roskos, "Coherent emission of electromagnetic pulses from Bloch oscillations in semiconductor superlattices," in *Festkörperprobleme 34*, pp. 297–315, Springer, 1995.

[95] R. Sapienza, P. Costantino, D. Wiersma, M. Ghulinyan, C. J. Oton, and L. Pavesi, "Optical analogue of electronic Bloch oscillations," *Physical Review Letters*, vol. 91, no. 26, p. 263902, 2003.

[96] V. Agarwal, J. Del Río, G. Malpuech, M. Zamfirescu, A. Kavokin, D. Coquillat, D. Scalbert, M. Vladimirova, and B. Gil, "Photon Bloch oscillations in porous silicon optical superlattices," *Physical Review Letters*, vol. 92, no. 9, p. 097401, 2004.

[97] H. Trompeter, T. Pertsch, F. Lederer, D. Michaelis, U. Streppel, A. Bräuer, and U. Peschel, "Visual observation of Zener tunneling," *Physical Review Letters*, vol. 96, no. 2, p. 023901, 2006.

[98] N. L. Kimura, A. Fainstein, and B. Jusserand, "Phonon Bloch oscillations in acoustic-cavity structures," *Physical Review B*, vol. 71, no. 4, p. 041305, 2005.

[99] N. Lanzillotti-Kimura, A. Fainstein, B. Perrin, B. Jusserand, O. Mauguin, L. Largeau, and A. Lemaître, "Bloch oscillations of THz acoustic phonons in coupled nanocavity structures," *Physical Review Letters*, vol. 104, no. 19, p. 197402, 2010.

[100] M. de Lima Jr, Y. A. Kosevich, P. Santos, and A. Cantarero, "Surface acoustic Bloch oscillations, the Wannier-Stark ladder, and Landau-Zener tunneling in a solid," *Physical Review Letters*, vol. 104, no. 16, p. 165502, 2010.

[101] M. B. Dahan, E. Peik, J. Reichel, Y. Castin, and C. Salomon, "Bloch oscillations of atoms in an optical potential," *Physical Review Letters*, vol. 76, no. 24, p. 4508, 1996.

[102] S. Wilkinson, C. Bharucha, K. Madison, Q. Niu, and M. Raizen, "Observation of atomic Wannier-Stark ladders in an accelerating optical potential," *Physical Review Letters*, vol. 76, no. 24, p. 4512, 1996.

[103] Q. Niu, X.-G. Zhao, G. Georgakis, and M. Raizen, "Atomic Landau-Zener tunneling and Wannier-Stark ladders in optical potentials," *Physical Review Letters*, vol. 76, no. 24, p. 4504, 1996.

[104] D. Averin, A. Zorin, and K. Likharev, "Bloch oscillations in small Josephson junctions," *Sov. Phys. JETP*, vol. 61, no. 2, pp. 407–413, 1985.

[105] K. Likharev and A. Zorin, "Theory of the Bloch-wave oscillations in small Josephson junctions," *Journal of Low Temperature Physics*, vol. 59, no. 3-4, pp. 347–382, 1985.

[106] Y. A. Kosevich and V. V. Gann, "Magnon localization and Bloch oscillations in finite Heisenberg spin chains in an inhomogeneous magnetic field," *Journal of Physics: Condensed Matter*, vol. 25, no. 24, p. 246002, 2013.

[107] C. Wittig, "The landau- zener formula," *The Journal of Physical Chemistry B*, vol. 109, no. 17, pp. 8428–8430, 2005.

[108] H. Qin, G.-J. Both, S. J. Hämäläinen, L. Yao, and S. van Dijken, "Low-loss YIG-based magnonic crystals with large tunable bandgaps," *Nature Cfommunications*, vol. 9, no. 1, p. 5445, 2018.

[109] Q. Wang, B. Heinz, R. Verba, M. Kewenig, P. Pirro, M. Schneider, T. Meyer, B. Lägel, C. Dubs, T. Brächer, *et al.*, "Spin pinning and spin-wave dispersion in nanoscopic ferromagnetic waveguides," *Physical Review Letters*, vol. 122, no. 24, p. 247202, 2019.

[110] S. Demokritov, A. Serga, A. Andre, V. Demidov, M. Kostylev, B. Hillebrands, and A. Slavin, "Tunneling of dipolar spin waves through a region of inhomogeneous magnetic field," *Physical Review Letters*, vol. 93, no. 4, p. 047201, 2004.

[111] M. Dvornik, *Numerical Investigations of Spin Waves at the Nanoscale*. PhD thesis, University of Exeter, Sept. 2011.

[112] A. Chumak, V. Tiberkevich, A. Karenowska, A. Serga, J. Gregg, A. Slavin, and B. Hillebrands, "All-linear time reversal by a dynamic artificial crystal," vol. 1, no. 141, 2010.

[113] S. Choi, J. Choi, R. Landig, G. Kucsko, H. Zhou, J. Isoya, F. Jelezko, S. Onoda, H. Sumiya, V. Khemani, *et al.*, "Observation of discrete time-crystalline order in a disordered dipolar many-body system," *Nature*, vol. 543, no. 7644, p. 221, 2017.

[114] L. Peng, Y. Zhang, W. Wang, M. He, L. Li, B. Ding, J. Li, Y. Sun, X.-G. Zhang, J. Cai, *et al.*, "Real-space observation of nonvolatile zero-field biskyrmion lattice generation in mnniga magnet," *Nano Letters*, vol. 17, no. 11, pp. 7075–7079, 2017.

[115] L. Peng, Y. Zhang, M. He, B. Ding, W. Wang, J. Li, J. Cai, S. Wang, G. Wu, and B. Shen, "Multiple tuning of magnetic biskyrmions using in situ l-tem in centrosymmetric mnniga alloy," *Journal of Physics: Condensed Matter*, vol. 30, no. 6, p. 065803, 2018.

[116] W. Wang, Y. Zhang, G. Xu, L. Peng, B. Ding, Y. Wang, Z. Hou, X. Zhang, X. Li, E. Liu, *et al.*, "A centrosymmetric hexagonal magnet with superstable biskyrmion magnetic nanodomains in a wide temperature range of 100–340 K," *Advanced Materials*, vol. 28, no. 32, pp. 6887–6893, 2016.

[117] L. Peng, Y. Zhang, M. He, B. Ding, W. Wang, H. Tian, J. Li, S. Wang, J. Cai, G. Wu, *et al.*, "Generation of high-density biskyrmions by electric current," *npj Quantum Materials*, vol. 2, no. 1, p. 30, 2017.

[118] C. Phatak, A. Petford-Long, and M. De Graef, "Recent advances in lorentz microscopy," *Current Opinion in Solid State and Materials Science*, vol. 20, no. 2, pp. 107–114, 2016.

[119] T. E. Gureyev and K. A. Nugent, "Rapid quantitative phase imaging using the transport of intensity equation," *Optics Communications*, vol. 133, no. 1-6, pp. 339–346, 1997.

[120] D. Stickler, R. Frömter, H. Stillrich, C. Menk, C. Tieg, S. Streit-Nierobisch, M. Sprung, C. Gutt, L.-M. Stadler, O. Leupold, *et al.*, "Soft x-ray holographic microscopy," *Applied Physics Letters*, vol. 96, no. 4, p. 042501, 2010.

[121] N. Bukin, C. McKeever, E. Burgos-Parra, P. Keatley, R. Hicken, F. Ogrin, G. Beutier, M. Dupraz, H. Popescu, N. Jaouen, *et al.*, "Time-resolved imaging of magnetic vortex dynamics using holography with extended reference autocorrelation by linear differential operator," *Scientific reports*, vol. 6, p. 36307, 2016.

[122] H. Popescu, J. Perron, B. Pilette, R. Vacheresse, V. Pinty, R. Gaudemer, M. Sacchi, R. Delaunay, F. Fortuna, K. Medjoubi, *et al.*, "COMET: a new end-station at SOLEIL for coherent magnetic scattering in transmission," *Journal of Synchrotron Radiation*, vol. 26, no. 1, 2019.

[123] G. van der Laan and A. I. Figueroa, "X-ray magnetic circular dichroism—a versatile tool to study magnetism," *Coordination Chemistry Reviews*, vol. 277, pp. 95–129, 2014.

[124] J. C. Loudon, A. C. Twitchett-Harrison, D. Cortés-Ortuño, M. T. Birch, L. A. Turnbull, A. Štefančič, F. Y. Ogrin, E. O. Burgos-Parra, N. Bukin, A. Laurenson, *et al.*, "Do images of biskyrmions show type-ii bubbles?," *Advanced Materials*, vol. 31, no. 16, p. 1806598, 2019.

[125] K. Baker, "A review of magnetic bubble memories and their applications," *Radio and Electronic Engineer*, vol. 51, no. 3, pp. 105–115, 1981.

[126] T. Schneider, A. A. Serga, B. Leven, B. Hillebrands, R. L. Stamps, and M. P. Kostylev, "Realization of spin-wave logic gates," *Applied Physics Letters*, vol. 92, no. 2, p. 022505, 2008.

[127] T. H. R. Skyrme, "A unified field theory of mesons and baryons," *Nuclear Physics*, vol. 31, pp. 556–569, 1962.

[128] N. Nagaosa and Y. Tokura, "Topological properties and dynamics of magnetic skyrmions," *Nature Nanotechnology*, vol. 8, no. 12, p. 899, 2013.

[129] J. Sampaio, V. Cros, S. Rohart, A. Thiaville, and A. Fert, "Nucleation, stability and current-induced motion of isolated magnetic skyrmions in nanostructures," *Nature Nanotechnology*, vol. 8, no. 11, p. 839, 2013.

[130] V. Krivoruchko and A. Marchenko, "Apparent sixfold configurational anisotropy and spatial confinement of ferromagnetic resonances in hexagonal magnetic antidot lattices," *Journal of Applied Physics*, vol. 109, no. 8, p. 083912, 2011.

[131] A. Marchenko and V. Krivoruchko, "Skyrmion-like bubbles and stripes in a thin ferromagnetic film with lattice of antidots," *Journal of Magnetism and Magnetic Materials*, vol. 377, pp. 153–158, 2015.

[132] C.-R. Mann, T. J. Sturges, G. Weick, W. L. Barnes, and E. Mariani, "Manipulating type-i and type-ii dirac polaritons in cavity-embedded honeycomb metasurfaces," *Nature communications*, vol. 9, no. 1, p. 2194, 2018.

[133] J. Wen, A. Rüegg, C.-C. J. Wang, and G. A. Fiete, "Interaction-driven topological insulators on the kagome and the decorated honeycomb lattices," *Physical Review B*, vol. 82, no. 7, p. 075125, 2010.

Appendix A

Data analysis codes

A.1 Holographic reconstruction: *hero.py*

The following code is used to reconstruct real space magnetic contrast using off axis Fourier transform holography with a slit reference, as described in section 4.2. This code is available for download on github: https://github.com/AngusLaurenson/HERALDO

```
1  import h5py as hd
2  import scipy as sp
3  import fabio
4  from skimage import feature, transform, color, exposure
5  from scipy import ndimage, fftpack, optimize
6  import matplotlib.pyplot as plt
7  from matplotlib.colors import LogNorm
8  from matplotlib import colors
9  import colorcet
10
11 class reconstructor():
12     """Reconstructor object takes left and right polarised
```

```
13      X-ray diffraction patterns as input and contains all the
14      methods required to automatically reconstruct the real
15      space magnetic contrast.
16
17      a = reconstructor(file_1, file_2)
18      a.reconstruct()
19
20      Complex, real space magnetic data is then stored as an
21      array attribute,
22
23      a.magnetic()
24
25      which can be further processed and plotted. If automatic
26      methods fail then manual inputs can be used to align the
27      inverse transform and differential filter.
28
29      This module lacks any functions for detecting or removing
30      hot pixels and stray light. This can be done by directly
31      editing the a.raw_1 and a.raw_2 arrays that hold the
32      raw data from each file.
33
34      """
35      def __init__(self, fname1, fname2):
36          super(reconstructor, self).__init__()
37          self.raw_1 = self.load_data(fname1)
38          self.raw_2 = self.load_data(fname2)
39
40
```

```
41      def load_data(self, fname):
42          # logic to open any data File
43          try:
44              return fabio.open(fname).data
45          except:
46              pass
47          try:
48              return self.load_nxs_data(fname)
49          except:
50              print('failure to read data')
51              pass
52
53      def load_nxs_data(self,fname):
54          ''' Accepts either file number or full name:
55          if input is number, make file fname '''
56          if fname.isdigit() == True:
57              fnum = fname
58              fname = 'scanx_' + str(fname) + '.nxs'
59          # else assume the input is file name and make number
60          else:
61              fnum = ''.join([a for a in fname.split('/')[-1] if a
    .isdigit()])
62          # open the nxs file and roots around for the data array
63          with hd.File(fname,'r') as f:
64              # explore the contents and scan group
65              group = [a for a in list(f.keys()) if a.find(str(
    fnum))][0]
```

```
66            # explore the contents of the scan data and find
    nonzero array
67            dset = [a for a in list(f[group]['scan_data'].keys()
    ) if sp.squeeze(f[group]['scan_data'][a].size >= 200)][0]
68            # make name for variable
69            return sp.squeeze(f[group]['scan_data'][dset])
70
71     def sum_dif(self, equalisation=True):
72         '''
73         optimising equalisation of input images to maximise
    signal to noise ratio, remove non magnetic signals
74         this section does not cancel out the aperture in the
    magnetic images
75         it is likely that normalising over a subset of the image
     would be better
76         '''
77         if equalisation is True and hasattr(self, 'ratio') is
    False:
78             def sum_abs_dif_data(ratio):
79                 return sp.sum(sp.absolute(self.raw_1[:500,1500:]
     - ratio * self.raw_2[:500,1500:]),axis=(0,1))
80
81             ratio = optimize.minimize(sum_abs_dif_data, 1).x[0]
82             self.ratio = ratio
83
84         elif equalisation is False:
85             self.ratio = 1
86
```

```
87          self.dif_data = self.raw_1 - self.ratio * self.raw_2
88          self.sum_data = self.raw_1 + self.ratio * self.raw_2
89          self.div_data = self.raw_1/self.raw_2
90
91      def auto_centre(self, data, sigma=0, count=10):
92          # hough transform to fit circles and vote
93          # Load picture and detect edges
94          image = data / sp.amax(data)
95          edges = feature.canny(image, sigma)
96
97          # Detect two radii
98          hough_radii = sp.arange(20, 35, 2)
99          hough_res = transform.hough_circle(edges, hough_radii)
100
101         accums, cx, cy, radii = transform.hough_circle_peaks(
    hough_res, hough_radii,total_num_peaks=count)
102
103         self.centre = [sp.mean(cx),sp.mean(cy)]
104         self.centre_radius = sp.mean(radii)
105
106     def auto_angle(self, data, sigma=5):
107         slope, intercept, r_value, p_value, std_err = sp.stats.
    linregress(
108         sp.arange(data.shape[0]), sp.argmax(ndimage.
    gaussian_filter(data,sigma), axis=1))
109         self.angle = sp.arctan(slope)
110
111     def display_callibration(self):
```

```
112         # calculate the fit line from callibration parameters
113         x = sp.linspace(-self.sum_data.shape[0]/2,self.sum_data.
    shape[0]/2,self.sum_data.shape[0])
114 #           c = self.centre[0] - self.angle*self.centre[1]
115         y = sp.sin(self.angle)*x + self.centre[0]
116         z = sp.cos(self.angle)*x + self.centre[1]
117 
118         plt.figure();
119         plt.imshow(self.sum_data, cmap = 'plasma',
120                    norm=LogNorm())
121         plt.scatter(*self.centre,marker='x',color='orange')
122         plt.scatter(y,z,marker='.',color='green')
123         plt.show()
124 
125     def beam_stop_blur(self, data, sigma=3, edge = 60):
126         index = sp.indices(self.sum_data.shape)
127         index[0,:,:] = index[0,:,:] - self.centre[1]
128         index[1,:,:] = index[1,:,:] - self.centre[0]
129 
130         mask = 1-ndimage.gaussian_filter(sp.where(sp.sum(index
    **2, axis=0)>(2*self.centre_radius+edge)**2+40, 0.0, 1.0),
    sigma)
131         return data*mask
132 
133     def beam_stop_stopper(self, data, sigma=5, edge=10):
134         '''Uses circular smoothed mask to cutout beamstop at
    centre'''
135         radius = self.centre_radius + edge
```

```
136         # setup the metric space and empty mask
137         position = sp.array(self.centre)
138         indices = sp.indices(data.shape)
139         mask = sp.zeros(data.shape)
140         # filled circle of ones at the centre
141         mask[sp.where(sp.sum((indices-position[:,None,None])**2,
    axis=0) < radius**2)] = 1
142         # smooth the circle of ones out
143         mask = sp.ndimage.gaussian_filter(mask,sigma)
144         # apply inverse mask to the data and return
145         return data * (1 - mask/sp.amax(mask))
146
147     # perform filtering, inverse fourier transform and phase
    phase_correction
148     # requires prior callibration
149     def differential_filtering(self, data):
150         # differential_filter
151         x,y = sp.meshgrid(sp.arange(data.shape[1]),
152                           sp.arange(data.shape[0]))
153         self.diff_filter = sp.pi * 2 * (+sp.cos(self.angle)*(x-
    self.centre[0]) \
154         -sp.sin(self.angle)*(y-self.centre[1]))
155
156         # apply differential_filter
157         filtered_data = data * self.diff_filter
158         return  filtered_data
159
160     def fourier_2D(self, data):
```

```
161         # fourier transform
162         return fftpack.fftshift(fftpack.fft2(data),axes=(0,1))
163
164     def offset_correction(self, data):
165         # phase correct for offset fourier transform
166         x,y = sp.meshgrid(sp.arange(data.shape[1]),
167                           sp.arange(data.shape[0]))
168
169         data = data * sp.exp(1j*2*sp.pi*(self.centre[0] * x /
    self.sum_data.shape[0] + self.centre[1] * y / self.sum_data.
    shape[1]))
170         return data
171
172     def display(self, data, cmap='coolwarm', linthresh=10):
173         plt.figure()
174         plt.imshow(data,
175             norm=colors.SymLogNorm(linthresh=linthresh),
176             origin='lower',
177             cmap = cmap,
178             interpolation='none'
179         )
180         plt.show()
181
182     def phase_amp_data(self, data):
183         # generate phase color array
184         norm = plt.Normalize()
185         phase_colors = colorcet.cm['cyclic_mygbm_30_95_c78_s25'
    ](norm(sp.angle(data)))
```

```
186         # generate amplitude greyscale array
187         norm = plt.Normalize()
188         amplitude_colors = colorcet.cm['linear_grey_10_95_c0'](
    norm(sp.absolute(data)**(0.2)))
189         # combine amplitude and phase
190         phase_amplitude = phase_colors*amplitude_colors
191         # return
192         return phase_amplitude
193
194     def max_real(self, data):
195         angles = sp.ravel(sp.angle(data))
196         amplitudes = sp.ravel(sp.absolute(data))
197         zipped = list(zip(angles,amplitudes))
198         res = sorted(zipped, key = lambda x : x[0])
199         angles, amplitudes = list(zip(*res))
200         filtered = sp.ndimage.gaussian_filter1d(amplitudes, 100,
     mode='wrap')
201     #     print(angles[sp.where(filtered == sp.amax(filtered))
    [0][0]])
202         return angles[sp.where(filtered == sp.amax(filtered))
    [0][0]], angles, amplitudes
203
204
205         return angle, angle2
206
207     def reconstruct(self, blur = True, equalisation=True):
208         # check for subtracted 'dif_data', else generate
209         # self.sum_dif() and check if callibration exists,
```

```
210         # if non try to auto detection
211         if hasattr(self, 'sum_data'):
212             pass
213         else:
214             # create sum and difference images with automatic
    equalisation
215             self.sum_dif(equalisation=equalisation)
216         if hasattr(self, 'angle'):
217             pass
218         else:
219             # calcualte automatically the angle of diffraction
    line
220             self.auto_angle(self.sum_data)
221         if hasattr(self, 'centre'):
222             pass
223         else:
224             try:
225                 # find centre of diffraction rings
226                 self.auto_centre(self.sum_data);
227             except:
228                 print('failed to fit centre automatically\n set
    manually\n')
229
230         # define intermediate data arrays
231         dif = self.dif_data.copy()
232         sum = self.sum_data.copy()
233         div = self.div_data.copy()
234
```

```
235         # beam stop blurr application to the images
236         dif = self.beam_stop_blur(dif, 10, 50)
237         sum = self.beam_stop_blur(sum, 10, 50)
238         div = self.beam_stop_blur(div, 10, 50)
239 
240         dif = self.differential_filtering(dif)
241         sum = self.differential_filtering(sum)
242         div = self.differential_filtering(div)
243 
244         dif = self.fourier_2D(dif)
245         sum = self.fourier_2D(sum)
246         div = self.fourier_2D(div)
247 
248         dif = self.offset_correction(dif)
249         sum = self.offset_correction(sum)
250         div = self.offset_correction(div)
251 
252 
253         # assign attributes
254         self.magnetic = dif
255         self.charge = sum
256         self.magnetic_div = div
257 
258     def save_image(self, name, data):
259         plt.ioff
260         plt.figure()
261         plt.imshow(data,
```

```
262             norm=colors.SymLogNorm(linthresh=0.03, linscale
    =0.03),
263             origin='lower',
264             cmap = 'plasma',
265             interpolation='none'
266             )
267         plt.savefig(name+'.png')
268
269     def quick_reconstruction(self, data):
270         F = data/self.sum_data
271         self.auto_centre(self.sum_data)
272         return(self.offset_correction(self.fourier_2D(F)))
```

Appendix B

Mode profiles of bubble domains in an antidot lattice

The band structure and correpsonding mode profiles of collective breathing, gyrating and ellipitcal modes of the bubble domain array are shown in this appendix.

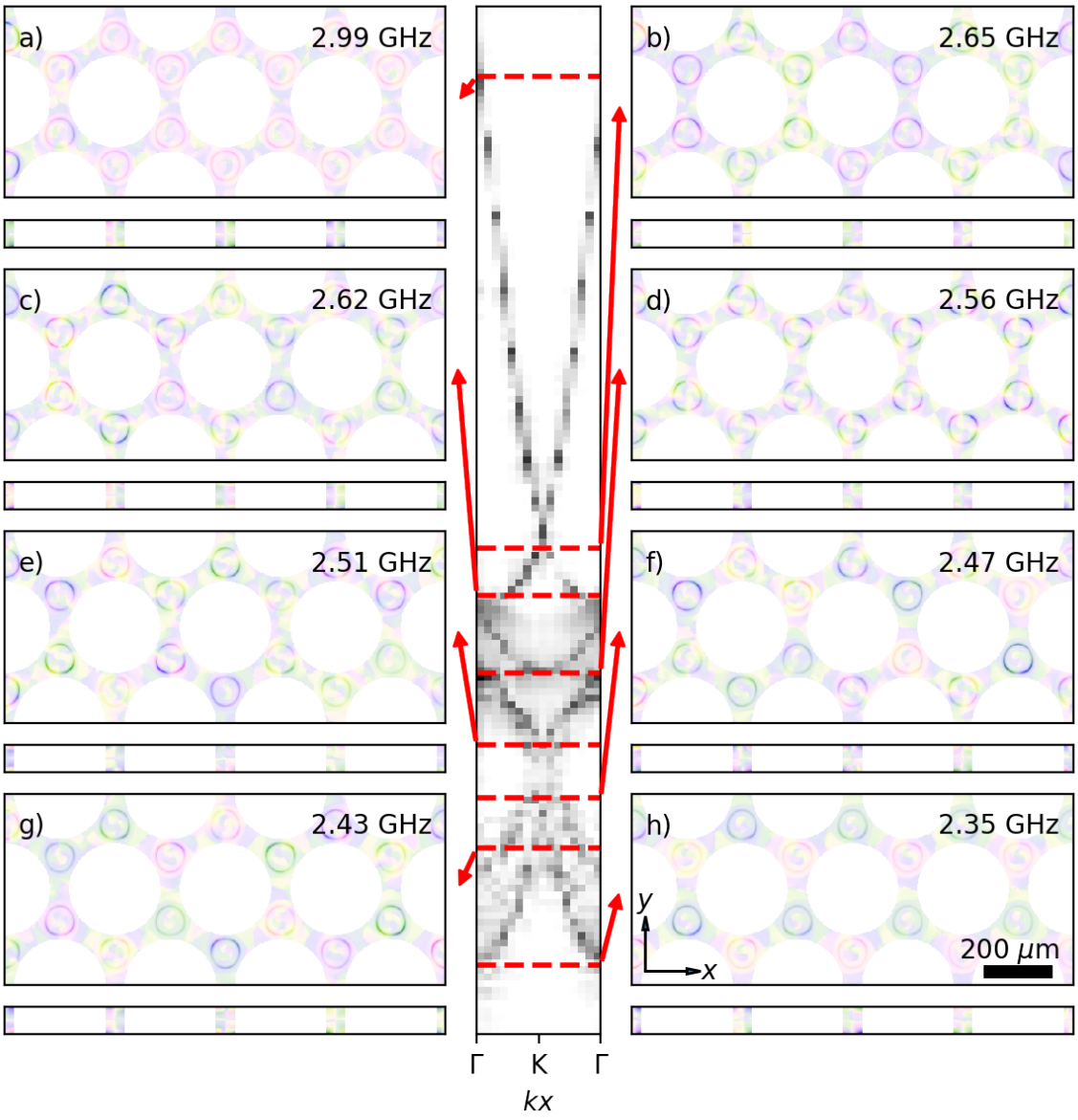

Fig. B.1 The band structure of the collective breathing modes propagating along the x axis is shown in the centre, with the corresponding mode profiles on either side. colour shows relative phase of precession and intensity the amplitude as shown in the inset colour wheel. A uniform phase around the domain wall of each individual bubble domains shows they are in the breathing mode. The difference in phase between neighbours shows the wavelength of the collective breathing modes.

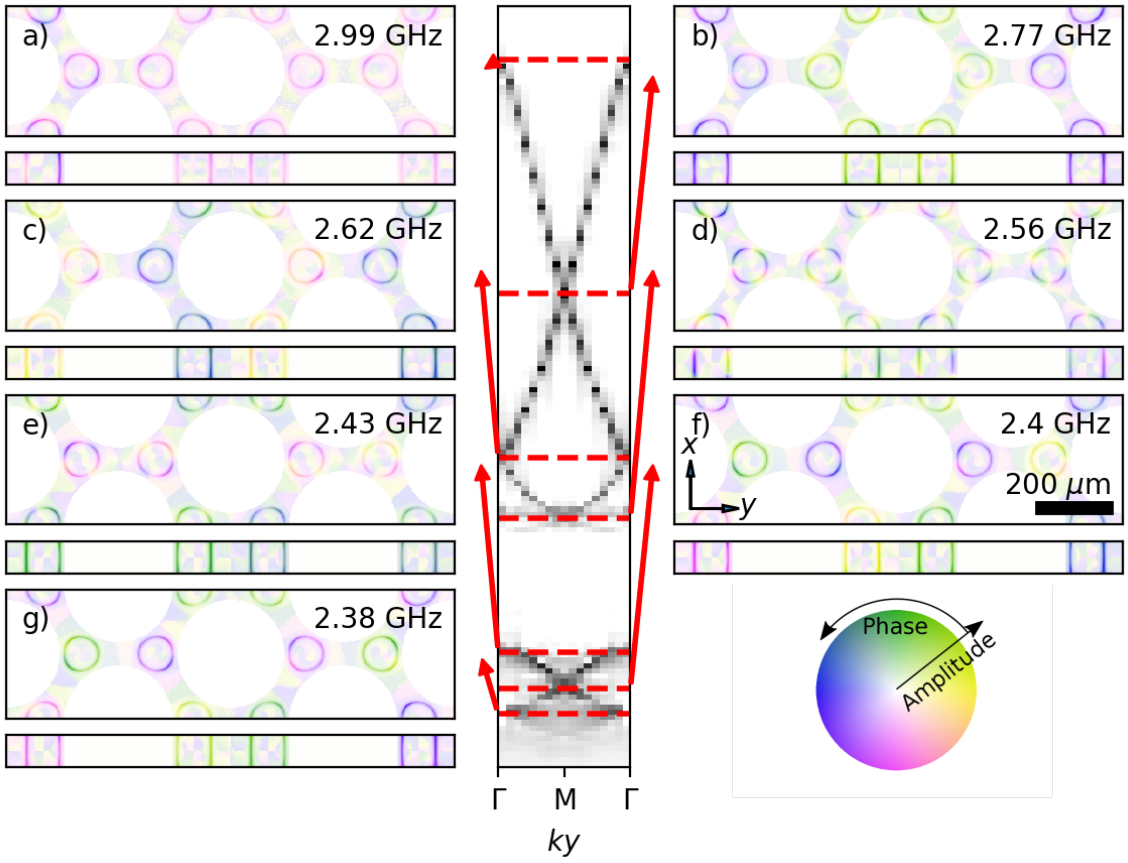

Fig. B.2 The band structure of the collective breathing modes propagating along the y axis is shown in the centre, with the corresponding mode profiles on either side. colour shows relative phase of precession and intensity the amplitude as shown in the inset colour wheel. A uniform phase around the domain wall of each individual bubble domains shows they are in the breathing mode. The difference in phase between neighbours shows the wavelength of the collective breathing modes.

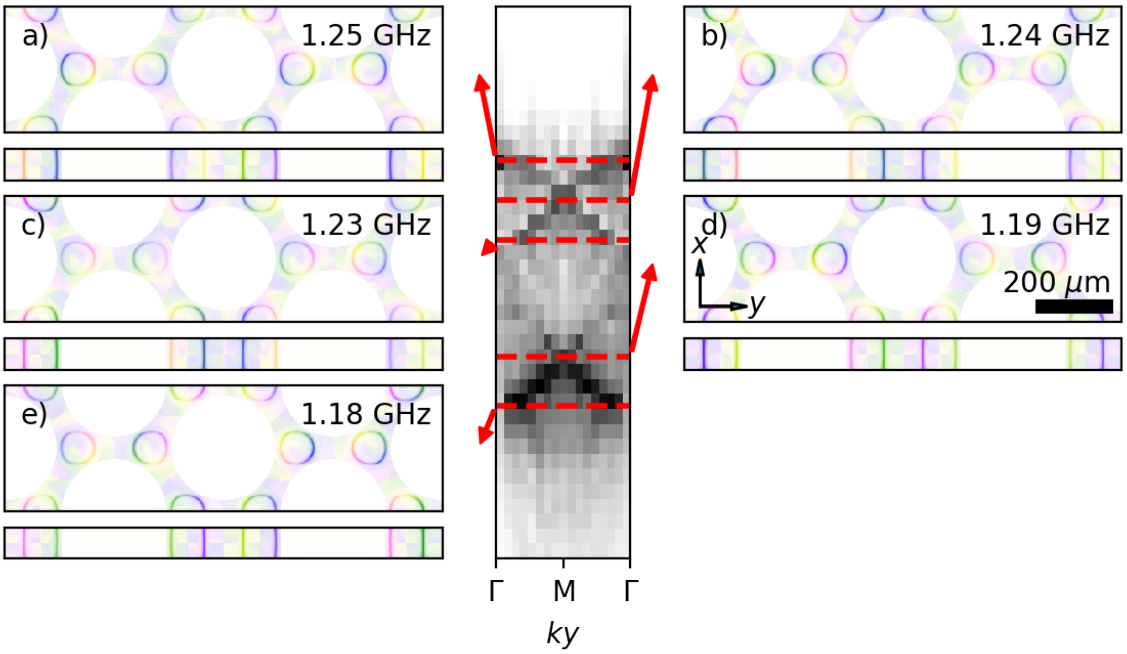

Fig. B.3 The band structure of the collective gyration modes propagating along the y axis is shown in the centre, with the corresponding mode profiles on either side. colour shows relative phase of precession and intensity the amplitude as shown in the inset colour wheel. A uniform phase around the domain wall of each individual bubble domains shows they are in the gyration mode. The difference in phase between neighbours shows the wavelength of the collective gyration modes.

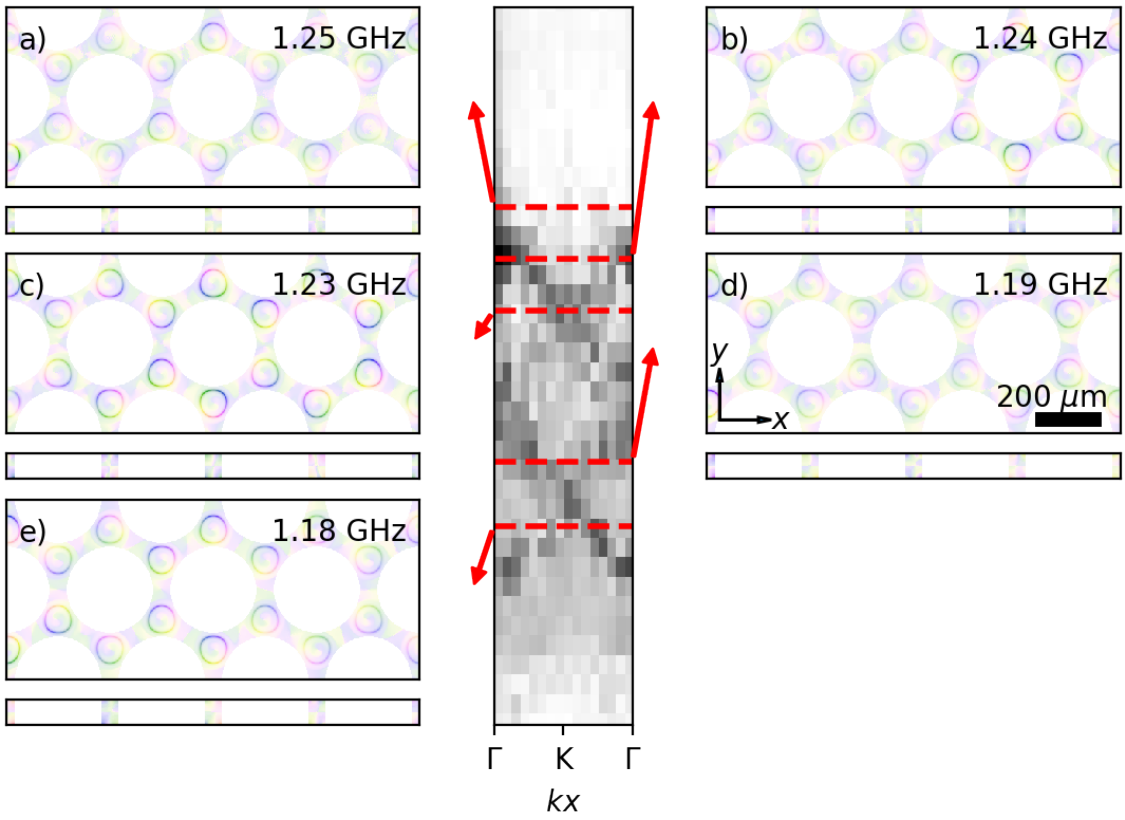

Fig. B.4 The band structure of the collective gyration modes propagating along the x axis is shown in the centre, with the corresponding mode profiles on either side. colour shows relative phase of precession and intensity the amplitude as shown in the inset colour wheel. A uniform phase around the domain wall of each individual bubble domains shows they are in the gyration mode. The difference in phase between neighbours shows the wavelength of the collective gyration modes.

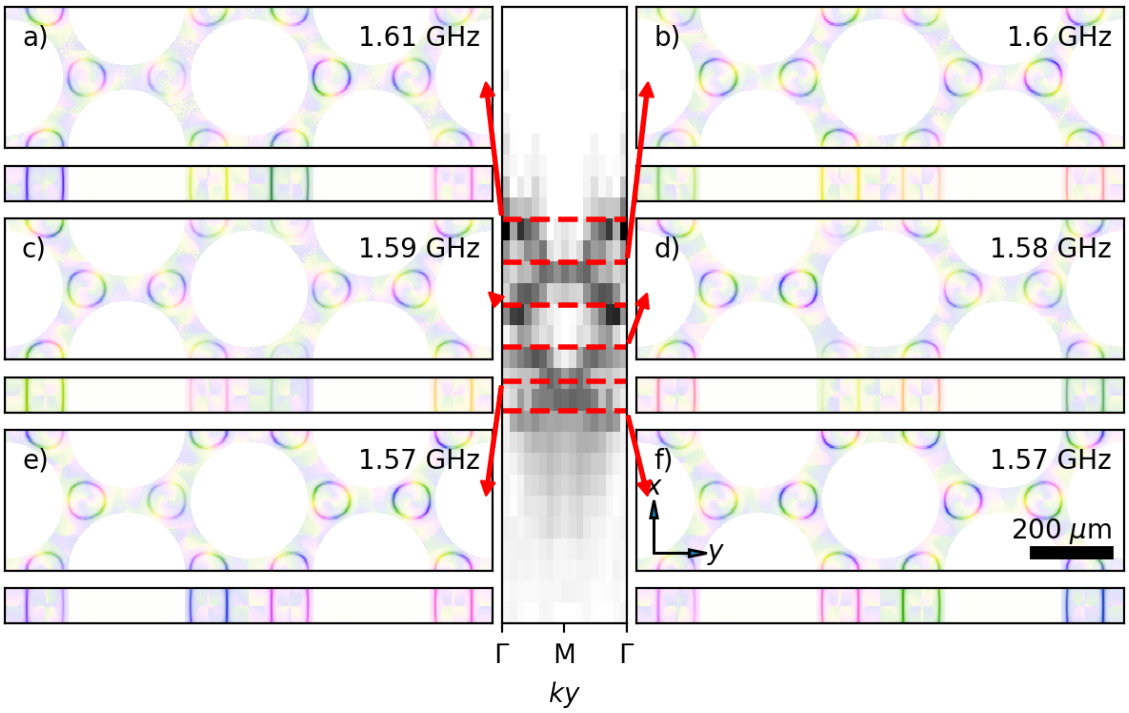

Fig. B.5 The band structure of the collective elliptical modes propagating along the *y* axis is shown in the centre, with the corresponding mode profiles on either side. colour shows relative phase of precession and intensity the amplitude as shown in the inset colour wheel. A uniform phase around the domain wall of each individual bubble domains shows they are in the elliptical mode. The difference in phase between neighbours shows the wavelength of the collective elliptical modes.

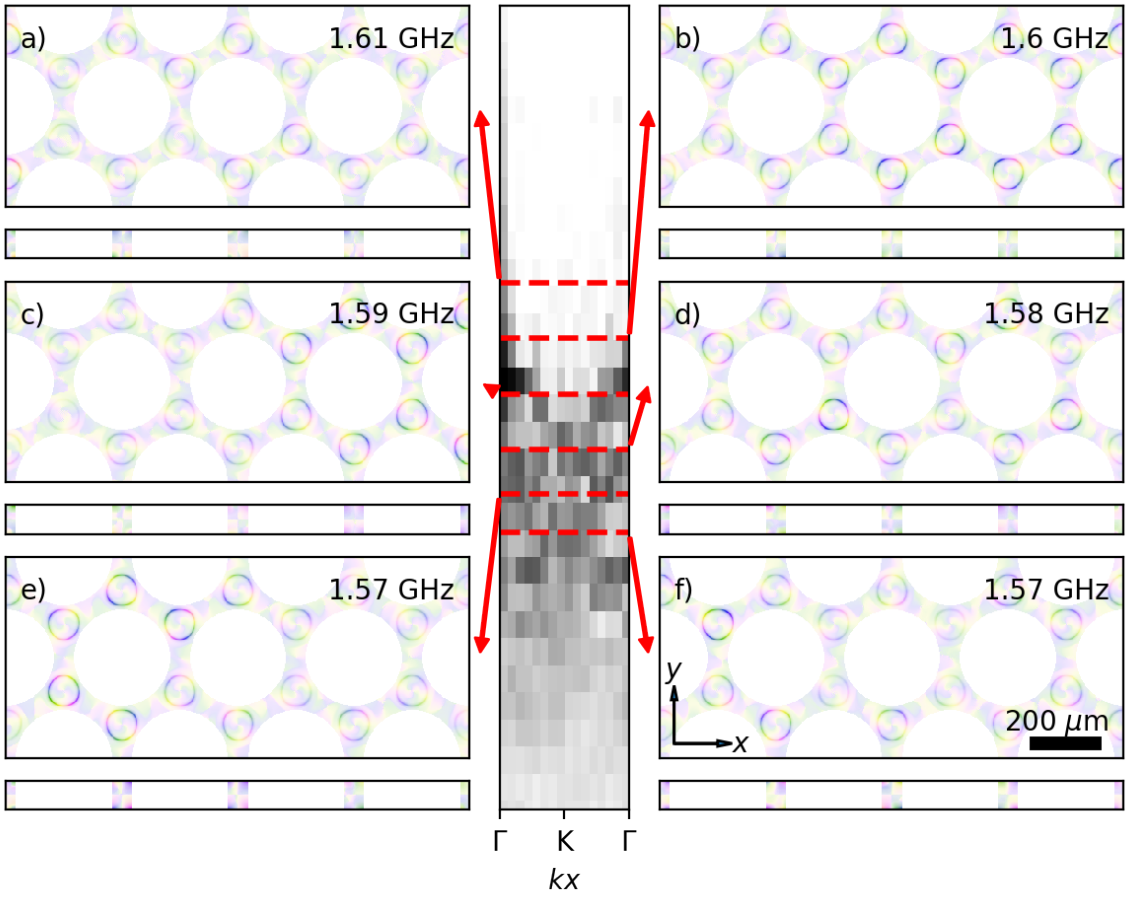

Fig. B.6 The band structure of the collective elliptical modes propagating along the x axis is shown in the centre, with the corresponding mode profiles on either side. colour shows relative phase of precession and intensity the amplitude as shown in the inset colour wheel. A uniform phase around the domain wall of each individual bubble domains shows they are in the elliptical mode. The difference in phase between neighbours shows the wavelength of the collective elliptical modes.